

AD \_\_\_\_\_

Award Number: DAMD17-03-1-0353

TITLE: Monitoring of Breast Tumor Response to Local  
Chemotherapeutic Agent Delivered by Biodegradable Fibers

PRINCIPAL INVESTIGATOR: Jae G. Kim

CONTRACTING ORGANIZATION: University of Texas at Arlington  
Arlington, TX 76019-0498

REPORT DATE: May 2005

TYPE OF REPORT: Annual

PREPARED FOR: U.S. Army Medical Research and Materiel Command  
Fort Detrick, Maryland 21702-5012

DISTRIBUTION STATEMENT: Approved for Public Release;  
Distribution Unlimited

The views, opinions and/or findings contained in this report are those of the author(s) and should not be construed as an official Department of the Army position, policy or decision unless so designated by other documentation.

20051107 295

# REPORT DOCUMENTATION PAGE

*Form Approved*  
**OMB No. 0704-0188**

Public reporting burden for this collection of information is estimated to average 1 hour per response, including the time for reviewing instructions, searching existing data sources, gathering and maintaining the data needed, and completing and reviewing this collection of information. Send comments regarding this burden estimate or any other aspect of this collection of information, including suggestions for reducing this burden to Department of Defense, Washington Headquarters Services, Directorate for Information Operations and Reports (0704-0188), 1215 Jefferson Davis Highway, Suite 1204, Arlington, VA 22202-4302. Respondents should be aware that notwithstanding any other provision of law, no person shall be subject to any penalty for failing to comply with a collection of information if it does not display a currently valid OMB control number. **PLEASE DO NOT RETURN YOUR FORM TO THE ABOVE ADDRESS.**

<b>1. REPORT DATE (DD-MM-YYYY)</b> 01-06-2005		<b>2. REPORT TYPE</b> Annual		<b>3. DATES COVERED (From - To)</b> 1 May 2004 - 30 Apr 2005	
<b>4. TITLE AND SUBTITLE</b> Monitoring of Breast Tumor Response to Local Chemotherapeutic Agent Delivered by Biodegradable Fibers				<b>5a. CONTRACT NUMBER</b>	
				<b>5b. GRANT NUMBER</b> DAMD17-03-1-0353	
				<b>5c. PROGRAM ELEMENT NUMBER</b>	
<b>6. AUTHOR(S)</b> Jae G. Kim  E-Mail: jae@uta.edu				<b>5d. PROJECT NUMBER</b>	
				<b>5e. TASK NUMBER</b>	
				<b>5f. WORK UNIT NUMBER</b>	
<b>7. PERFORMING ORGANIZATION NAME(S) AND ADDRESS(ES)</b> University of Texas at Arlington Arlington, TX 76019-0498				<b>8. PERFORMING ORGANIZATION REPORT NUMBER</b>	
<b>9. SPONSORING / MONITORING AGENCY NAME(S) AND ADDRESS(ES)</b> U.S. Army Medical Research and Materiel Command Fort Detrick, Maryland 21702-5012				<b>10. SPONSOR/MONITOR'S ACRONYM(S)</b>	
				<b>11. SPONSOR/MONITOR'S REPORT NUMBER(S)</b>	
<b>12. DISTRIBUTION / AVAILABILITY STATEMENT</b> Approved for Public Release; Distribution Unlimited					
<b>13. SUPPLEMENTARY NOTES</b>					
<b>14. ABSTRACT</b> Abstract follows.					
<b>15. SUBJECT TERMS</b> Near-infrared spectroscopy, <sup>19</sup> F MR PO <sub>2</sub> mapping, biodegradable fiber					
<b>16. SECURITY CLASSIFICATION OF:</b>			<b>17. LIMITATION OF ABSTRACT</b>  UU	<b>18. NUMBER OF PAGES</b>  123	<b>19a. NAME OF RESPONSIBLE PERSON</b>
<b>a. REPORT</b> U	<b>b. ABSTRACT</b> U	<b>c. THIS PAGE</b> U			<b>19b. TELEPHONE NUMBER (include area code)</b>

## ABSTRACT

For the second year of the project, we have investigated the cyclophosphamide dose effects on rat breast tumor hemodynamics and also monitored how tumor hemodynamics is affected by a vascular disrupting agent by a near-infrared spectroscopy. For experiments, we have applied systemic chemotherapy of cyclophosphamide (CTX) to two groups of rats bearing syngeneic 13762NF mammary adenocarcinomas: one group received a single high dose i. p. (200 mg/kg CTX) and the other group metronomic low doses (20 mg/kg CTX i. p. for 10 days). Combretastatin (CA4P) which is one of vascular disrupting agents was also administered to the rats (30 mg/kg, i. p.) to see its effects in tumor hemodynamics. After CTX treatments, significant changes in vascular hemodynamic response to oxygen inhalation were observed from both groups. The preliminary results suggest that cyclophosphamide has greatest effect on the well perfused tumor vasculature. CA4P administration caused significant decreases in tumor blood volume and oxygenation, and tumor vasculature recovered its function slowly at day 1 after CA4P administration. Overall, our study supports our earlier hypothesis, proving that the effects of chemotherapy in tumor may be monitored non-invasively by using NIRS by detecting the changes of hemodynamics induced with respiratory challenges.

---

## Table of Contents

Cover.....	
SF 298.....	
Table of Contents.....	3
Introduction.....	4
Body.....	5
Key Research Accomplishments.....	18
Reportable Outcomes.....	18
Conclusions.....	19
References.....	20
Appendices.....	20

This report presents the specific aims and accomplishments of our breast cancer research project during the second of funding sponsored by the U.S. Army Department of the Defense. It covers our activities from May 1, 2004 to April 30, 2005.

## Introduction

The overall goals of this research are to evaluate NIRS technique as a non-invasive tool for monitoring the drug effects in breast tumors and to compare the effects of systemically delivered drug and locally delivered drug with embedded biodegradable fibers. In the first year of the project, systemic chemotherapy has been applied to rat breast tumors with a single high dose (200mg/kg) of cyclophosphamide (CTX). The results have shown that the hemodynamics of blood oxygenation ( $\Delta[\text{HbO}_2]$ ) increase during oxygen intervention has become significantly changed before and after CTX administration which proved NIRS could be used as a monitoring tool for cancer therapy. In the second year of this project, we have expanded systemic CTX treatment on tumors by applying metronomic low dose treatment (20mg/kg for 10 days) to see the differences in treatment efficacy comparing to a single high dose CTX treatment. We have also applied combretastatin (CA4D), one of vascular disrupting agents, to see its acute effects in tumor hemodynamics by monitoring the change of tumor blood oxygenation and also blood volume. Throughout this study, it will allow us to validate a non-invasive tool that can monitor the effects of chemotherapy on breast tumors and to demonstrate advantages of local drug delivery using biodegradable fibers for breast tumor treatment. Our study may help breast cancer patients under chemotherapy have a higher survival rate and better quality of life with reduced side effects and proper tumor treatment selection.

## Objectives:

The overall project has five specific aims:

**Aim 1:** to monitor tumor vascular oxygenation during oxygen/carbogen interventions using both NIRS and  $^{19}\text{F}$  MR pO<sub>2</sub> mapping after a systemic drug delivery.

**Aim 2:** to compare the effects of the systemically delivered drugs on the vascular and tissue oxygenation of the breast tumors in order to validate the monitoring capability of the two techniques for breast cancer treatment.

**Aim 3:** to develop/implement biodegradable fibers loaded with a chemotherapeutic agent for local drug delivery at the specific breast cancer site.

**Aim 4:** to monitor tumor vascular oxygenation during oxygen/carbogen interventions using both NIRS and  $^{19}\text{F}$  MR pO<sub>2</sub> mapping after a local drug delivery through a biodegradable fiber.

**Aim 5:** to compare the chemotherapy effects between local drug delivery and systemic drug delivery.

Specifically, Task 2 was planned for months 8-16 to accomplish Aims 1 and 2, and Task 3 was planned for months 17-21 to accomplish Aim 3. Task 4 was planned for months 22-30 to achieve Aims 4 and 5:

**Task 2:** To monitor tumor vascular oxygenation during oxygen/carbogen interventions using both NIRS and  $^{19}\text{F}$  MR pO<sub>2</sub> mapping after a systemic drug delivery. **(months 8-16):**

**Task 3:** To develop/implement biodegradable fibers loaded with a chemotherapeutic agent for local drug delivery at the specific breast cancer site. **(months 17-21):**

**Task 4:** To monitor tumor vascular oxygenation during oxygen/carbogen interventions using both NIRS and  $^{19}\text{F}$  MR pO<sub>2</sub> mapping after a local drug delivery through a biodegradable fiber. **(months 22-30):**

## Body of the Report

The PI has made significant efforts to accomplish the tasks. The overall purpose of this project is to evaluate NIRS technique as a non-invasive tool for monitoring the drug effects in breast tumors and to compare the effects of systemically delivered drug and locally delivered drug with embedded biodegradable fibers. In the first year, I have obtained the specific skills for handling laboratory animals and appropriate knowledge of tumor physiology and NIR spectroscopy. Meanwhile, I have conducted primary experiments on breast tumors with a single dose of systemic CTX treatment for evaluating NIRS system and assessing the changes in dynamic response of breast tumor oxygenation with respect to respiratory challenges before and after CTX treatment (See the annual report in year 1). During the second year (May 1, 2004~April 30,2005), I have expanded the previous systemic CTX treatment on tumors by applying metronomic low dose treatment (20mg/kg for 10 days) to see the differences in treatment efficacy comparing to a single high dose CTX treatment. In addition to that, we have also applied a combretastatin (CA4D), one of vascular disrupting agents, on tumors to see its acute effects in tumor hemodynamics by monitoring the change of tumor blood oxygenation and also blood volume. As a part of developing a drug loaded biodegradable fiber, I have conducted the spectrophotometric experiments to obtain a calibration curve of CTX concentration which will be used later for drug release kinetics measurement. I have mainly accomplished the task proposed in this period, as reported below:

### 1. Metronomic low dose CTX treatment.

We have monitored the hemodynamics changes after a single high dose of CTX treatment in the first year period and proved that multi-channel NIRS could be used as a monitoring tool to detect the therapeutic effects from chemotherapy. In the second year of the project, CTX treatment study has been further expanded to see the effect from a low dose of CTX and also from the size of tumor before treatment.

#### 1.1 Experimental setup and procedures

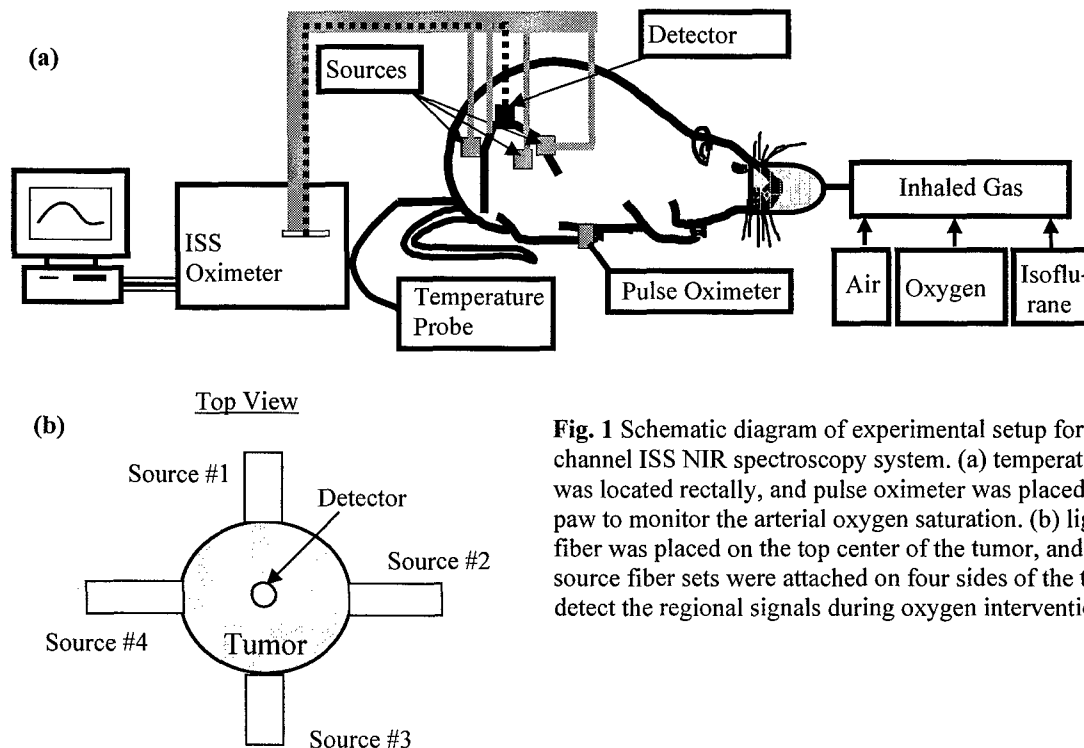
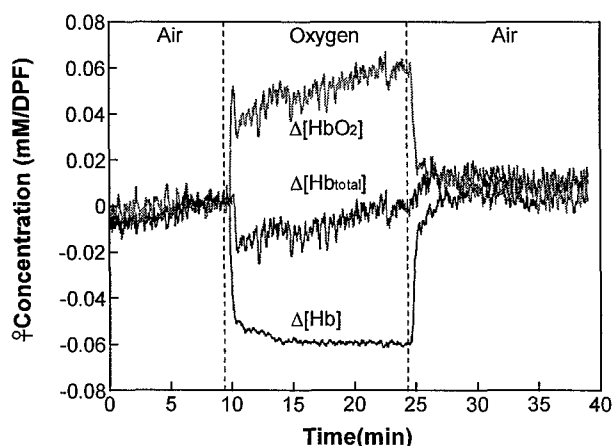


Fig. 1 Schematic diagram of experimental setup for the 4-channel ISS NIR spectroscopy system. (a) temperature probe was located rectally, and pulse oximeter was placed on the hind paw to monitor the arterial oxygen saturation. (b) light detector fiber was placed on the top center of the tumor, and four light source fiber sets were attached on four sides of the tumor to detect the regional signals during oxygen intervention.

The tumor line was rat mammary adenocarcinomas 13762NF (cells originally provided by the Division of Cancer Therapeutics, NCI), and the tumors were implanted in the hind limb of adult female Fisher 344 rats (~200 g). A four-channel, frequency domain, NIRS (ISS, Champaign, IL) has been utilized during the second year of project to obtain the dynamic response of tumor oxygenation during oxygen gas intervention. We have divided rats into two groups which are control group (n=3) and CTX treated group (n=3). During the measurements, four light source fiber sets (750 and 830 nm) were placed on the side of tumor and a light detector fiber was located centrally on the top of tumor, providing us with four different regional signals of tumor vascular oxygenation during oxygen inhalation (Figure 1). Changes of  $[\text{HbO}_2]$ ,  $[\text{Hb}]$ , and  $[\text{Hb}_{\text{total}}]$  were simultaneously measured during a sequence of air to oxygen and then to air for studying the dynamic response of tumor oxygenation to oxygen intervention. A low dose of CTX (20mg/kg) was administered into the rats via i.p. injection daily for 10 days which results in total amount of CTX (200mg) same as the dose (200mg/kg) used during the first year.

## 1.2 Results

A representative tumor hemodynamic change during experimental procedure is shown in Fig. 2. After around 10 minutes of air breathing measurement as the baseline, the inhaled gas was switched from air to oxygen, causing a sharp increase in  $\Delta[\text{HbO}_2]$  ( $p < 0.0001$  1 min. after gas switch) followed by a further gradual, but significant increase over the next 15 min ( $P < 0.0001$ ). However,  $\Delta[\text{Hb}_{\text{total}}]$  first dropped rapidly after switching gas from air to oxygen and then showed a gradual increase followed by 5 minutes of stabilization. This behavior could be explained by vasoconstriction of artery due to oxygen intervention which results in blood flow decreases and thus reduces blood volume. After returning to air inhalation,  $\Delta[\text{HbO}_2]$  decreased and  $\Delta[\text{Hb}_{\text{total}}]$  showed overshooting then slowly decreased, both reaching slightly higher than their respective baseline level. This result clearly shows that an NIRS can monitor the changes of blood oxygenation or blood volume in tumor dynamically and in real-time.



**Fig. 2** Time course of tumor vascular  $\Delta[\text{HbO}_2]$ ,  $\Delta[\text{Hb}]$ , and  $\Delta[\text{Hb}_{\text{total}}]$  for a representative 13762NF breast tumor with the inhaled gas under the sequence of air-oxygen-air.

### 1.2.1 Rat body weight and tumor volume changes after CTX treatments

Rat body weight and tumor volume were monitored before and after the CTX treatments to see the tumor responses and side effects from chemotherapy. Changes in rat body weight and tumor volume were normalized to day 0 (before CTX or saline administration). (Fig. 3) Solid circles represent the data from a control group, and open squares and open diamonds represent the continuous low dose group and single high dose group from the previous year, respectively. In the single high dose treatment group, body weight decreased until 6 days after the treatment, but later increased for the rest of days of observation.

Two rats among five in this group failed to survive at day 3 and 6 due to the toxicity from the high dose CTX treatment. Therefore, the data shown at day 8 and 10 represent the smaller group of rats which survived during the high dose treatment. Tumor volume did not further decreased after day 4. (Fig. 3(b)) In comparison, rats in the metronomic low dose group initially lost weight after a low dose of CTX administration, but gradually gained the weight during the treatment, presenting low toxicity from the treatment. This group also showed a significant reduction in tumor volume during the treatment. For the control group, the average rat body weight gradually decreased during the entire course of treatment, which implies the sickness of rats possibly due to the tumor growth (cachexia). (At Day 10, the tumor volume was ~5 times larger than that at Day 0.)

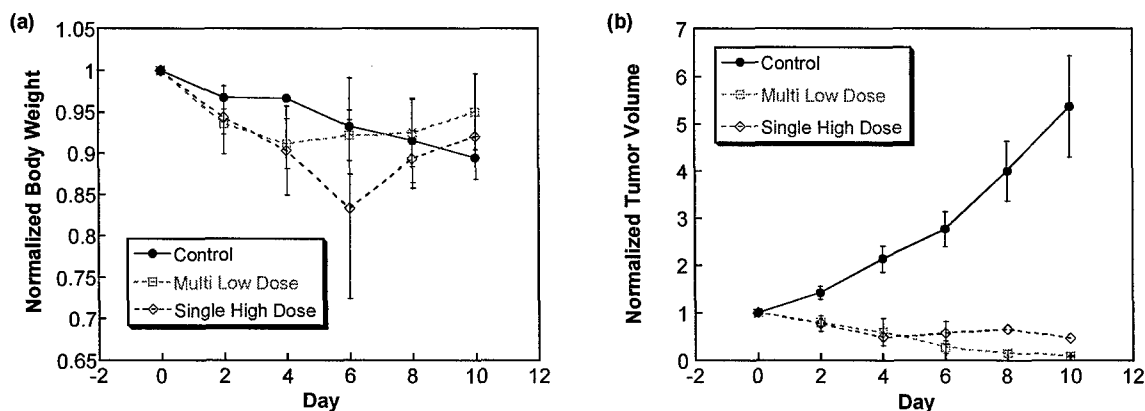


Fig. 3 Normalized changes in rat body weight (a) and tumor volume (b) during the saline and CTX treatments.

## 1.2.2 Tumor vascular hemodynamics changes before and after CTX treatments

### 1.2.2.1 A high single dose CTX treatment

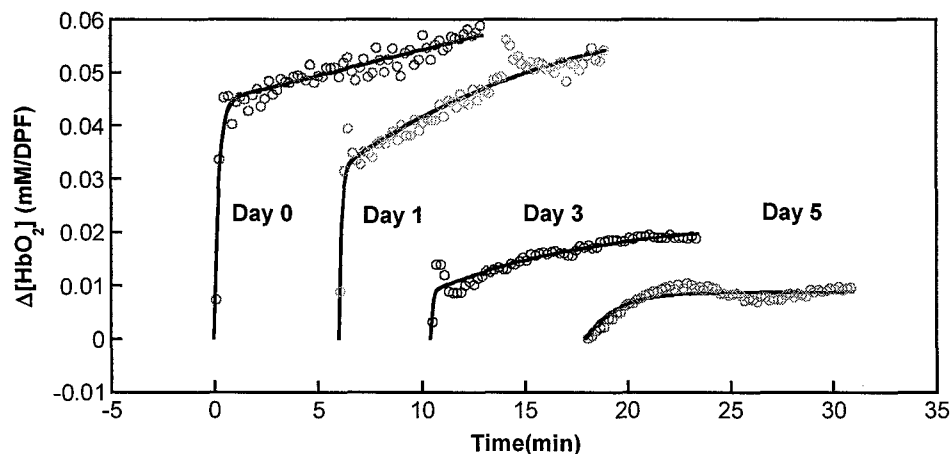


Fig. 4 Dynamic changes of  $[\text{HbO}_2]$  taken at location #1 from a rat breast tumor before and after a single high dose of CTX treatments (200mg/kg). The rising part of  $\Delta[\text{HbO}_2]$  from location #1 was fitted using either a single- or double-exponential expression.

The tumor hemodynamics during oxygen intervention was measured before and after administration of CTX and saline. Figure 4 shown here was presented in the first year report and represents the changes of

tumor hemodynamics during oxygen intervention during a single high dose of CTX treatment. This figure clearly demonstrated that we could observe significant changes in tumor hemodynamics after chemotherapy by using respiratory challenge as a mediator.

The amplitude and time constants obtained from  $\Delta[\text{HbO}_2]$  increase (Fig. 4) were summarized in Table 1. At day 0, we can see that  $\gamma_1/\gamma_2$  is higher than 1, indicating that the measured signal results more from the well perfused region than poorly perfused region. However, this ratio becomes less than 1 after injection of cyclophosphamide (Day 1 and 3). This may be explained by destruction of vascular structure in tumor after chemotherapy. We expect that after a single high dose administration of CTX, the drug circulates in the blood vessels and is delivered to the tumor cells more in the well perfused region than in the poorly perfused region. This will lead to death of tumor cells in the well perfused region more effectively than that in the poorly perfused region, eventually resulting in decreases in tumor volume in the well perfused region more than in the poorly perfused region. Then, the tumor volume containing the well perfused regions will consequently decrease, so will the contribution of detected NIR signals from the well perfused region. In other words, a decrease in  $\gamma_1/\gamma_2$  may indicate decreases in well perfused regions in tumor volume, after the administration of CTX.

**Table 1.** Summary of vascular oxygen dynamics determined at location #1 from the tumor shown in Fig. 4 before and after a single high dose of CTX treatment.

Day	$A_1$	$A_2$	$\tau_1$	$\tau_2$	$A_1/A_2 (= \gamma_1/\gamma_2)$	$\tau_1/\tau_2$	$f_1/f_2$
0	0.044	0.031	0.23	25.21	1.42	0.0091	156
1	0.032	0.033	0.13	11.36	0.97	0.0114	85
3	0.0087	0.014	0.089	8.36	0.62	0.0106	58
5	0.0087		1.27				

#### 1.2.2.2 A metronomic low dose CTX treatment

The representative data from the control group and continuous low dose group are shown in Figs. 5(a) and 5(b), respectively. Open symbols are the raw data from measurements, and solid lines are the fitted curves using our double exponential model. As mentioned before, there were 4 light sources placed on the surface of tumor. Figure 5 shows the acute and then gradual changes of  $[\text{HbO}_2]$  after switching the breathing gas from air to oxygen, and the data were observed at the same (or nearly the same) location of tumor from day 0 to day 6. From Figure 5(a), we can see different tumor hemodynamics at different days, but having similar trends and maximum  $\Delta[\text{HbO}_2]$  for the control group. However, the data taken from the continuous low dose group show quite different hemodynamics throughout the treatment days (Fig. 5(b)). Especially, we notice that the fast increase part became much smaller at Days 2 and 6 compared to Day 0, implying a significant decrease in signal from the well perfused region.

The amplitudes and time constants obtained from  $\Delta[\text{HbO}_2]$  increase (Fig. 5(a) and 5(b)) were summarized in Table 2 and 3, respectively. The data at day 0 and 2 in Fig. 5(a) were fitted well with a mono exponential model rather than bi-exponential model which implies that tumor vasculature is roughly homogeneous. However, the  $\Delta[\text{HbO}_2]$  increase at day 6 in Fig. 5(a) was better fitted with bi-exponential model which tells us that tumor vasculature became heterogeneous and possibly hypoxic region was developed in the central region of tumor. The tumor sizes at day 0 and 2 were 0.55 and 0.74  $\text{cm}^3$  which can be considered as small tumors whereas the tumor size at day 6 was 1.67  $\text{cm}^3$  which was a large tumor that can possibly have necrotic regions in tumor. Since time constant values are related to the blood flow velocity in tumor [1,2], the increase of time constant represents the decrease of blood flow velocity. The time constant value at day 2 from table 2 was increased compared to the value from day 0, and we can understand this as a decrease of average blood flow velocity in tumor.

Table 3 summarized the fitted parameters from Fig. 5(b) which the tumor was treated under the metronomic low dose CTX plan. It shows a few similar features as observed from table 1 which the data are from one of the high dose CTX treated group. Firstly, time constant values ( $\tau_1$ ) were decreased as CTX treatments were undergoing. Secondly, the major decrease in maximum  $\Delta[\text{HbO}_2]$  during oxygen intervention came from the well perfused region rather than poorly perfused region which is shown by the decrease in  $A_1$  values. Therefore, thirdly, the ratio of well-perfused region and poorly perfused region became small at day 6 compared to day 0 shown by  $A_1/A_2$  decrease. While these two different CTX treatment plans showed a few similar effects on tumor hemodynamics, it is noteworthy that the tumor hemodynamics at day 6 from the metronomic low dose CTX treatment still showed a bi-exponential feature and also a relatively high maximum  $\Delta[\text{HbO}_2]$  compared to that observed from a tumor at day 5 after a single high dose CTX treatment. This may imply that the metronomic low dose CTX treatment caused less disruption in tumor vasculature while it still gave great therapeutic effects on rat breast tumors.

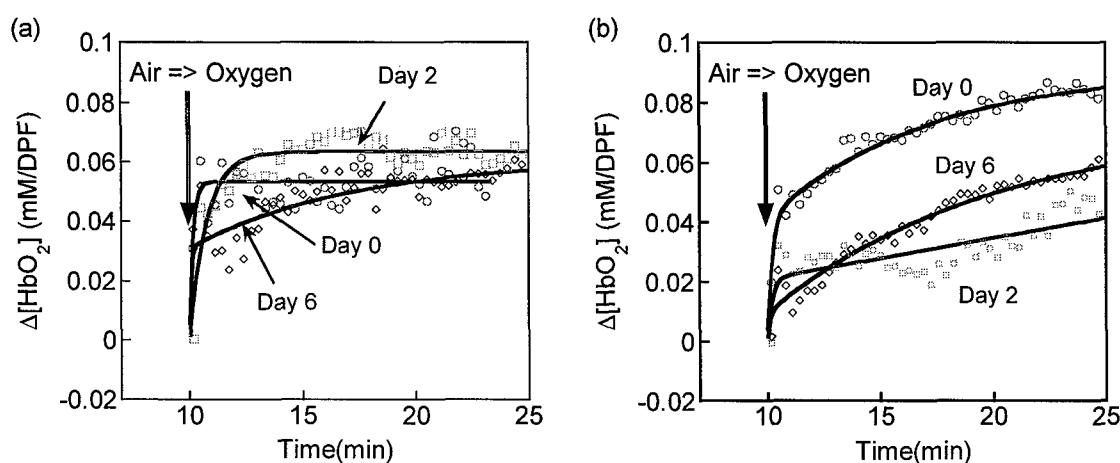


**Fig. 5** Dynamic changes of  $\Delta[\text{HbO}_2]$  taken at location #1 from a rat breast tumor before and after administration of (a) saline and (b) metronomic low dose of CTX (20 mg/kg for 10 days). The rising part of  $\Delta[\text{HbO}_2]$  from location #1 was fitted using either the single or double-exponential expression.

**Table 2.** Summary of vascular oxygen dynamics determined at location #1 from the tumor shown in Fig. 5 (a) as a control.

Day	$A_1$	$A_2$	$\tau_1$	$\tau_2$	$f_1 = A_1/\tau_1$	$A_1/A_2$	$\tau_1/\tau_2$	$f_1/f_2$
0	0.053		0.16		3.3			
2	0.063		0.77		0.08			
6	0.031	0.030	0.07	7.21		0.44	0.004	110

**Table 3.** Summary of vascular oxygen dynamics determined at location #1 from the tumor shown in Fig. 5 (b) before and after a metronomic low dose of CTX treatment.

Day	$A_1$	$A_2$	$\tau_1$	$\tau_2$	$A_1/A_2 (= \gamma_1/\gamma_2)$	$\tau_1/\tau_2$	$f_1/f_2$
0	0.041	0.05	0.20	7.19	0.82	0.028	29.3
2	0.021	0.02	0.21	12.7	1.05	0.017	61.8
6	0.009	0.06	0.12	9.96	0.15	0.006	25

## 2. The effect of tumor size on chemotherapeutic efficacy

As it was already described earlier, we have studied the therapeutic effects of metronomic low dose and compared to those observed from a single high dose CTX treated group. However, the rats studied for the single high dose CTX treatment had quite large tumor volumes ranged from 2.6 to 11.4 cm<sup>3</sup> while the tumor sizes used for the metronomic low dose CTX study were in the range of 0.57 to 1.02 cm<sup>3</sup>. Since the therapeutic effects from chemotherapy could be affected by tumor size, we performed the same CTX treatment as studied in the first year but with much smaller sizes of tumors (0.97 - 1.77 cm<sup>3</sup>). Figure 6 shows the distribution of rat body weight and tumor volume among three groups. The box includes 50% of the data with the median value of the variable displayed as a line. The lines extending from the top and bottom of each box mark the minimum and maximum values within the data set. It clearly shows that the tumor volumes of a high single dose CTX treated group in the first year are much greater than those from the CTX treated groups during the second year of project.

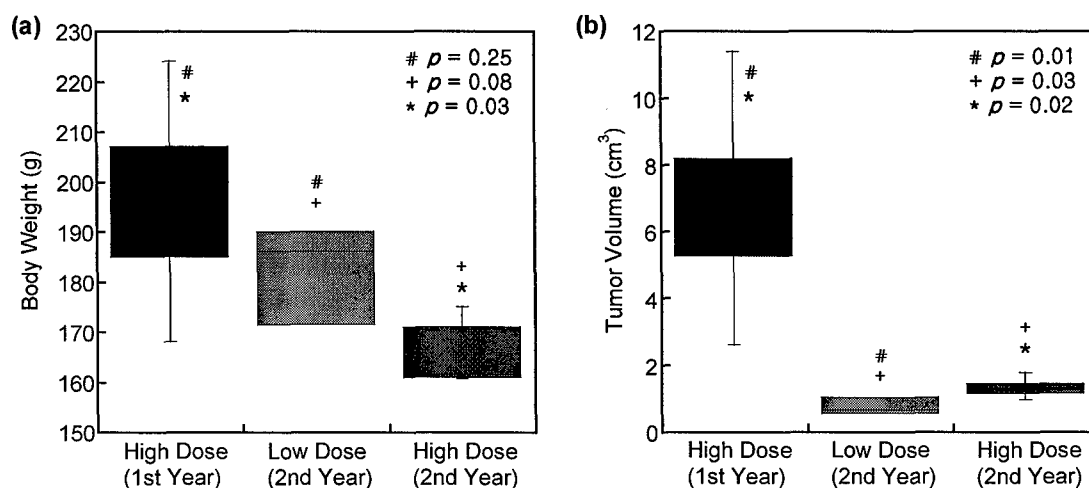


**Fig. 6** The distribution of rat body weight (a) and tumor volume (b) from three groups studied in the first and second year. The statistical analysis was performed to find the differences among groups and it has been shown that both the body weight and tumor volumes between the high dose CTX treated group during the first year and second year are significantly different ( $p < 0.05$ ).

### 2.1 Experimental setup

The same tumor line (rat mammary adenocarcinomas 13762NF) used in the first year study was implanted subcutaneously on the hind limb of fisher rats ( $n=5$ ). A broadband tungsten halogen light source (HL-2000HP, Ocean Optics Inc., Florida) and four channels spectrometer (Ocean Optics Inc., Florida) were utilized as a light source and detectors, respectively. The white light from the light source was delivered to the top of tumors through a light guide and transmitted light was detected by 4 channels spectrometer via four optical fibers on the side of tumors (Fig. 7). The intensities at 750 and 830 nm were traced during the experiments by using OoiBase32 software (Ocean Optics Inc., Florida) and changes of [Hb], [HbO<sub>2</sub>], and [Hb<sub>total</sub>] were obtained by using the modified Beer-Lambert's law. The experimental protocol was kept same as the one used during the first year's experiments. Rats were given air breathing for 10 minutes and then gas was switched from air to oxygen to give an increase in tumor blood oxygenation.

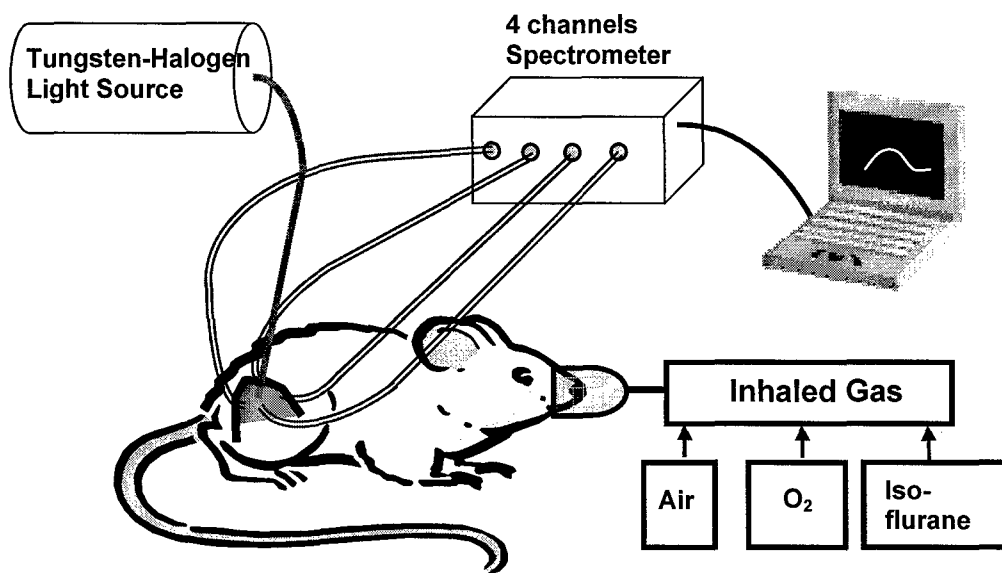


Fig. 7 Schematic diagram of experimental setup for the 4-channels NIR spectroscopy system. The changes of [Hb], [HbO<sub>2</sub>], and [Hb<sub>total</sub>] were monitored during the respiratory challenges and compared before and after a single high dose of CTX treatment.

## 2.2 Results

### 2.2.1 Comparison of rat body weight and tumor volume changes

The changes of rat body weight and tumor volume during a single high dose of CTX treatment were recorded and compared with the data from the first year. (Fig. 8) One rat among five in this group failed to survive at day 4, and all the other rats also could not survive at day 6 due to the toxicity from the high dose CTX treatment. The small tumor group showed a little more decrease in body weight after CTX treatment compared to the large tumor group studied in the first year. However, it was not significantly different between two groups throughout day 1 to 5 ( $p > 0.1$ ).

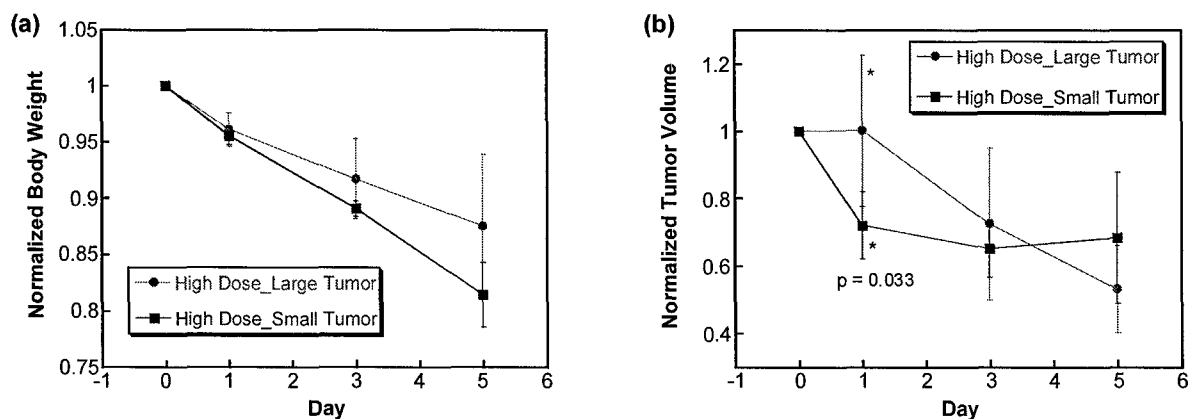
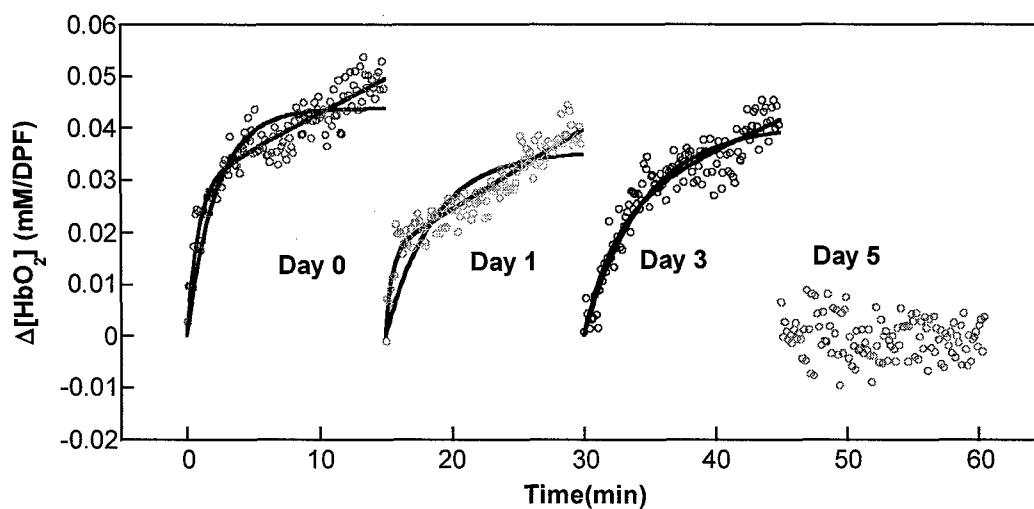


Fig. 8 Normalized changes in rat body weight (a) and tumor volume (b) during a single high dose of CTX treatments from the first year and the second year experiments.

In terms of tumor volume, the small tumor group initially showed more decrease in tumor volume than the large tumor group after CTX treatment, but did maintained their tumor volumes. However, the large tumor group did not greatly respond to CTX treatment at Day 1, but showed continuing decrease in tumor volume at day 3 and 5. Statistical analysis shows that there are no significant differences in tumor volume reduction after CTX treatment between the large and the small tumor group ( $p > 0.2$ ). However, the decrease in tumor volume at day 1 after CTX treatment showed a significant difference between a large and a small tumor group ( $p = 0.033$ ).

### **2.2.2 Tumor vascular hemodynamics changes during a single high dose CTX treatment**

The tumor hemodynamics during oxygen intervention was measured before and after administration of CTX as same as experiments during the first year. A representative data showing the changes of  $\Delta[\text{HbO}_2]$  from the small tumor group before and after a single high dose CTX treatment is shown in Fig. 9. The fitted parameters from our mathematical model are summarized in Table 2 to compare the changes in hemodynamic parameters before and after administration of CTX. The rising part of  $\Delta[\text{HbO}_2]$  from location #1 was fitted using either a single- or double- exponential expression. Unlike the data from the large tumor used in the first year, all rats with small tumor volumes were failed to survive more than 5 days after CTX treatment. Table 2 clearly shows the changes of hemodynamic parameters during oxygen intervention before and after a CTX treatment.



**Fig. 9** Dynamic changes of  $[\text{HbO}_2]$  taken at location #1 from a rat breast tumor before and after a single high dose of CTX treatments (200mg/kg). The rising part of  $\Delta[\text{HbO}_2]$  from location #1 was fitted using either a single- or double-exponential expression.

The  $\Delta[\text{HbO}_2]$  during the oxygen intervention observed at day 0 could be fit well with a bi-exponential model but not with a mono-exponential model. This bi-phasic feature of  $\Delta[\text{HbO}_2]$  during the oxygen intervention was again observed from the data at day 1, but not from the data at day 3. The  $\Delta[\text{HbO}_2]$  increase during the oxygen intervention at day 3 could be fit well by both mono- and also bi-exponential model. The maximum  $\Delta[\text{HbO}_2]$  during the oxygen intervention was decreased after a CTX treatment and actually showed slight negative values at day 5. This might implies that tumor vasculature lost its vascular function at day 5 after a CTX administration. The trend of changes in time constant values from the rapid increase part of  $\Delta[\text{HbO}_2]$  during the oxygen intervention ( $\tau_1$ ) shows the consistency with the trend observed from the large tumor data during the first year (see table 1). The  $\tau_1$  values were

decreased after a CTX treatment until the  $\Delta[\text{HbO}_2]$  could be fit well with a mono exponential model (day 3 in the table 4 and day 5 in the table 1). Since time constant values are related to tumor perfusion rate or more precisely blood flow velocity, the decrease of  $\tau_1$  values implies the increase of blood flow velocities in the well perfused region.

**Table 4.** Summary of vascular oxygen dynamics determined at location #1 from the tumor shown in Fig. 9 before and after CTX treatment.

Day	$A_1$	$A_2$	$\tau_1$	$\tau_2$	$A_1/A_2 (= \gamma_1/\gamma_2)$	$\tau_1/\tau_2$	$f_1/f_2$	R
0	0.024	0.037	0.83	14.5	0.65	0.057	11.4	0.95
1	0.017	0.045	0.51	23.6	0.38	0.022	17.3	0.96
3	0.024	0.019	2.44	9.53	1.26	0.26	4.8	0.95

Day	$A_1$	$\tau_1$	$f_1$	R
0	0.044	2.23	0.0197	0.89
1	0.035	3.67	0.0095	0.86
3	0.041	4.54	0.0090	0.95

The ratio of  $A_1/A_2 (= \gamma_1/\gamma_2)$  has been decreased nearly 40% from day 0 to day 1, indicating that less signals came from the well perfused region at day 1 compared to the data at day 0. This was also observed from the large tumor shown in the Fig. 4, and it was explained as follows. After administration of cyclophosphamide, it will be circulated in blood vessels and will be more delivered to the tumor cells in the well perfused region than those in the poorly perfused region. This will cause more apoptosis of tumor cells in the well perfused region than that in the poorly perfused region, eventually causing decreases in tumor volume in the well perfused region more than that in the poorly perfused region. Then, the tumor volume optically interrogated by detector #1 will have less contribution from the well perfused region than the poorly perfused region, leading to a decrease of  $\gamma_1/\gamma_2$ , after administration of cyclophosphamide.

### 3. Monitoring the effects of vascular disrupting agent on tumor vascular hemodynamics

Recently, many vascular disrupting agents (VDAs) including combretastatin (CA4P) have been intensively studied either by VDA itself or combination with other cancer therapies.[3] Since these VDAs will disrupt the blood vessels results in changes in vascular function in tumors, NIRS can be a possible tool to monitor the tumor hemodynamic responses to VDA administration. Kragh et al. have reported the effects of 5 vascular modifying agents (VMAs) including CA4P on tumor perfusion and tumor blood volume changes by utilizing the laser Doppler flowmetry and a single wavelength NIRS.[4] However, they did not show the dynamic changes in  $\Delta[\text{HbO}_2]$ ,  $\Delta[\text{Hb}]$ , and  $\Delta[\text{Hb}_{\text{total}}]$  modulated by VMA throughout the whole experimental time. Therefore, it will be valuable to monitor the tumor blood oxygenation and blood volume changes before and after CA4P administration and show the dynamic changes in tumor  $\Delta[\text{HbO}_2]$ ,  $\Delta[\text{Hb}]$ , and  $\Delta[\text{Hb}_{\text{total}}]$  for the entire measurement time.

#### 3.1 Experimental setup and procedures

The dynamic response of tumor oxygenation and blood volume to CA4P has been continuously monitored by a single channel NIRS. Since we can not detect absolute values of oxy- and deoxyhemoglobin in tumor, we have given oxygen intervention to give a tumor hemodynamic changes which can tell us the effects of CA4P in tumor vasculatures. For the experiments, rats were divided into

two groups. One group (n = 6) were received a saline administration as a control group and another group (n=8) had a CA4P injection with the dose of 30 mg/kg via i.p. as a treatment group. During the NIRS measurements, the following respiratory challenge paradigm was employed.

Air (15 min) → O<sub>2</sub> (20 min) → Air (15 min) → Saline/CA4P administration → Air (2 hours) → O<sub>2</sub> (20 min) → Air (5 min)

## 3.2 Results

### 3.2.1 Control group

A representative result from control group is shown in Fig. 10. After 15 minutes of air breathing measurement as the baseline, the inhaled gas was switched from air to oxygen, causing a sharp increase in oxyhemoglobin concentration ( $\Delta[\text{HbO}_2]$ ) ( $p < 0.0001$ , 1~2 min. after gas switch) followed by a further gradual, but significant increase over the next 18 min ( $P < 0.0001$ ). However, total hemoglobin concentration ( $\Delta[\text{Hb}_{\text{total}}]$ ) first dropped rapidly after switching gas from air to oxygen and then slowly recovered during the next 15 minutes of oxygen inhalation. After returning to air inhalation,  $\Delta[\text{HbO}_2]$  decreased and deoxyhemoglobin concentration ( $\Delta[\text{Hb}]$ ) increased, both reaching approximately their respective baseline level. 15 min after second air intervention, either saline for a control group or CA4P for a test group has been given by i.p. injection, and tumor hemodynamics was continuously monitored for 2 hours. The second oxygen intervention was given to be compared with the tumor response during the first oxygen intervention with the following 5 min of Air inhalation. As we can see in Fig. 10, the tumor response during the second oxygen intervention was very similar to the response observed during the first oxygen intervention for a control group.

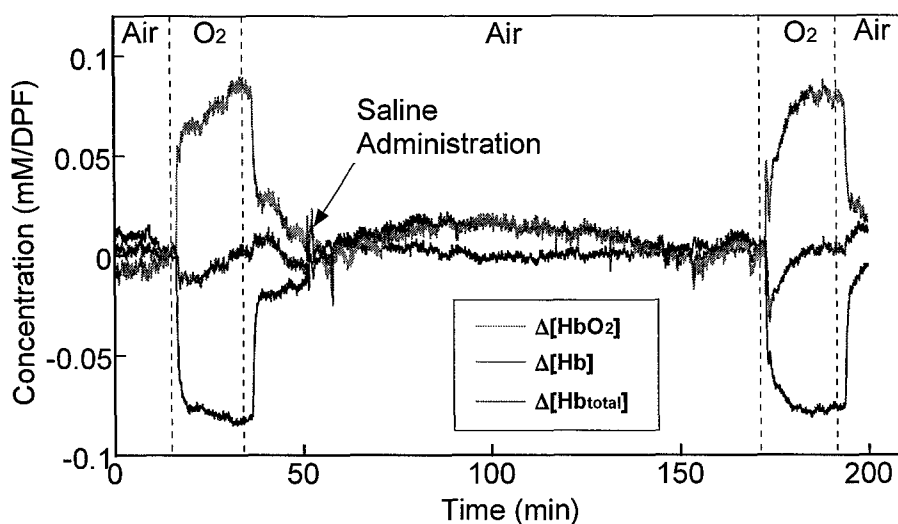


Figure 10. Time course of tumor vascular  $\Delta[\text{HbO}_2]$ ,  $\Delta[\text{Hb}]$ , and  $\Delta[\text{Hb}_{\text{total}}]$  for a 13762NF breast tumor with the inhaled gas under the sequence of air-oxygen-air-oxygen-air with the administration of saline.

### 3.2.2 CA4P treated group

The same experimental procedure was applied to the test group except that CA4P was administered instead of saline. Figure 11 shows the representative results from CA4P treatment group. Unlike the data from control group (Fig. 10),  $\Delta[\text{HbO}_2]$  and  $\Delta[\text{Hb}_{\text{total}}]$  have been significantly dropped about 40 seconds after CA4P administration while  $\Delta[\text{Hb}]$  concentration showed slight decrease. Both  $\Delta[\text{HbO}_2]$  and  $\Delta[\text{Hb}_{\text{total}}]$  have become stabilized 20 minutes after CA4P injection and maintained until the second oxygen intervention was given. The second oxygen intervention was applied 2 hours after CA4P administration, but both  $\Delta[\text{HbO}_2]$  and  $\Delta[\text{Hb}_{\text{total}}]$  showed little changes compared to the first oxygen intervention. These results clearly prove that CA4P is very effective in terms of blocking the blood flow in tumor vasculature so that it can be applied to the cancer treatments.

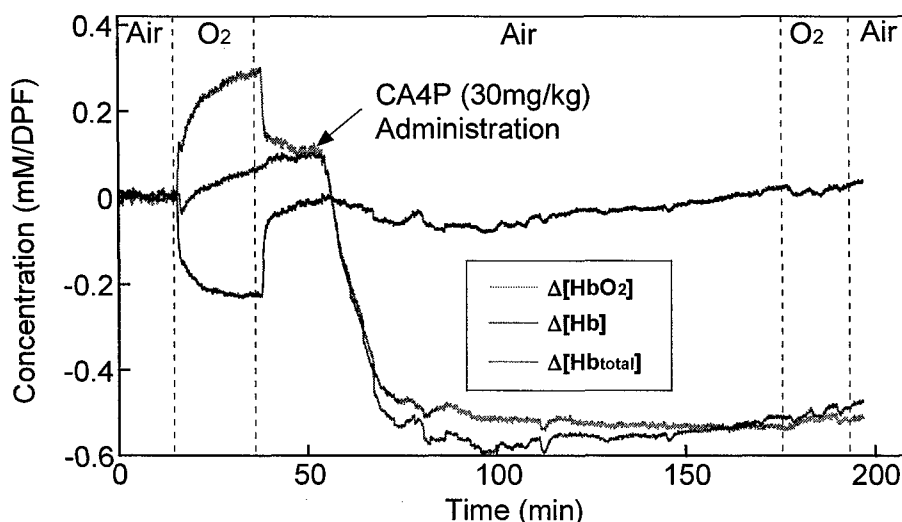


Figure 11. Time course of tumor vascular  $\Delta[\text{HbO}_2]$ ,  $\Delta[\text{Hb}]$ , and  $\Delta[\text{Hb}_{\text{total}}]$  for another 13762NF breast tumor with the inhaled gas under the sequence of air-oxygen-air-oxygen-air with the administration of CA4P.

### 3.2.3 Comparison of tumor response between a control and a CA4P treated group

Oxygen intervention was given again 1 day after either saline or CA4P administration to compare the tumor response with the responses observed at day 0 and 2 hours after agent administration. Figure 12 shows the results from the same tumors shown in Figs 10 and 11. Figure 12(a) shows the tumor response to the oxygen from 1 day after saline injection and the tumor response to the oxygen is very similar to the tumor response during oxygen inhalation in the Fig. 10. They both have similar level of  $\Delta[\text{HbO}_2]$  increase during oxygen intervention. However, the  $\Delta[\text{HbO}_2]$  increase observed in Fig. 12(b) is nearly ten times smaller than the amount of  $\Delta[\text{HbO}_2]$  increased shown in Fig. 11. This tells us that the effect of CA4P in tumor vasculature is not vanished and it's still affecting the tumor blood vessels. To see the changes of CA4P effects on tumor vasculature with the time, we have collected the tumor responses to the oxygen intervention at day 0, 2hours, day 1 and day 2 after CA4P administration and plotted them as a one figure (Fig. 13).

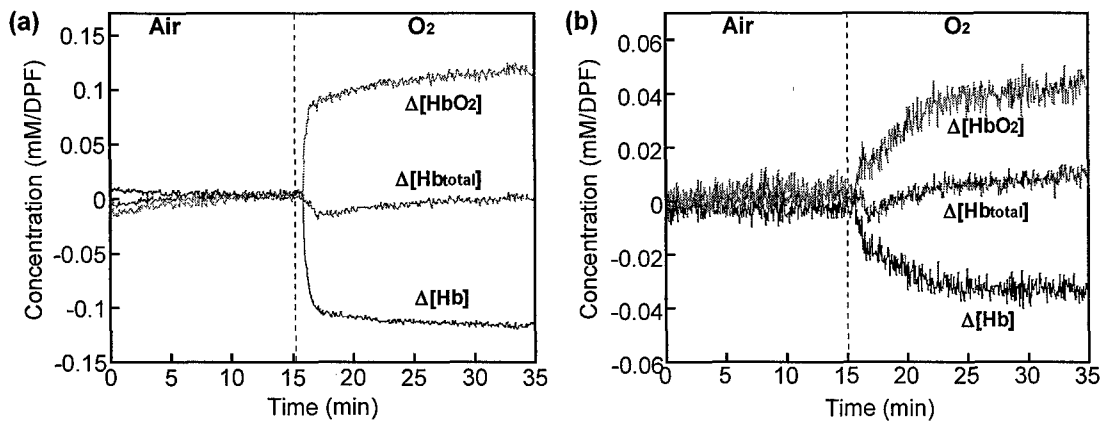


Figure 12. Changes in  $\Delta[\text{HbO}_2]$ ,  $\Delta[\text{Hb}]$ , and  $\Delta[\text{Hb}_{\text{total}}]$  from breast tumors shown in Fig. 1 and 2 during respiratory challenges from air to oxygen at 1 day after saline (a) and CA4P (b) administration.

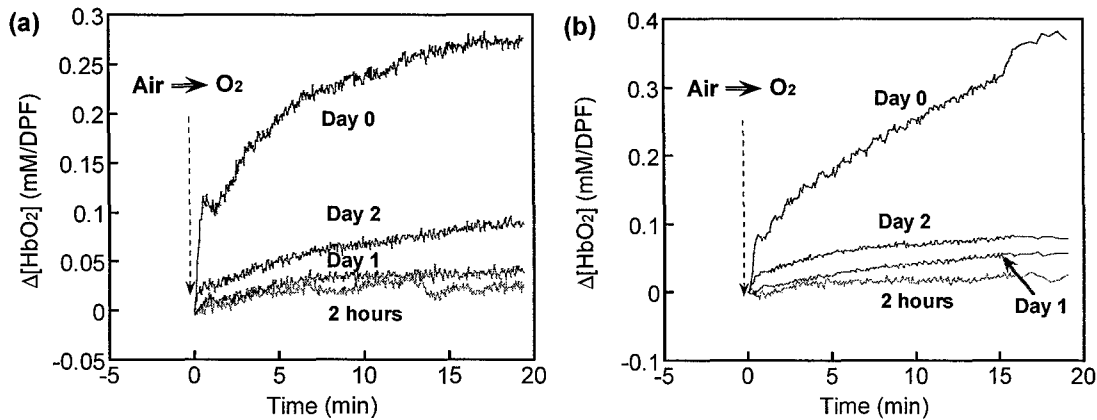


Figure 13. Dynamic changes of  $\Delta[\text{HbO}_2]$  from rat breast tumors during oxygen intervention before and after administration of CA4P.

Figure 13(a) is from the same tumor that was shown in Fig. 11 and 12(b) and the result from another tumor is shown in Fig. 13(b). These Figures clearly show the changes of tumor vascular responses to changes of tumor responses to oxygen intervention before and after CA4P administration. It's hard to find the fast component of  $\Delta[\text{HbO}_2]$  increase from the tumor response during oxygen inhalation 2 hours after CA4P administration. However, the initial fast increase of  $\Delta[\text{HbO}_2]$  is gradually showing up through Day 1 and 2 after CA4P administration.

To statistically compare the tumor response to oxygen intervention after saline and CA4P administration, we normalized the changes of  $\Delta[\text{HbO}_2]$  increase during the oxygen intervention and the mean and standard deviation were plotted in Fig. 14(a). It is very clear that there are no significant changes observed from the control group ( $p < 0.5$ ) while the CA4P group showed significant changes from day 0 to day 1 ( $p < 0.05$ ). We also plotted the mean and standard deviation of  $\Delta[\text{HbO}_2]$  and  $\Delta[\text{Hb}_{\text{total}}]$  during 2 hours right after saline and CA4P injection (Fig. 14(b)). Figure 14(b) shows that saline administration did not cause significant changes in  $\Delta[\text{HbO}_2]$  and  $\Delta[\text{Hb}_{\text{total}}]$  during 2 hours while  $\Delta[\text{HbO}_2]$  and  $\Delta[\text{Hb}_{\text{total}}]$  from CA4P group showed significant decrease during 2 hours after CA4P administration.

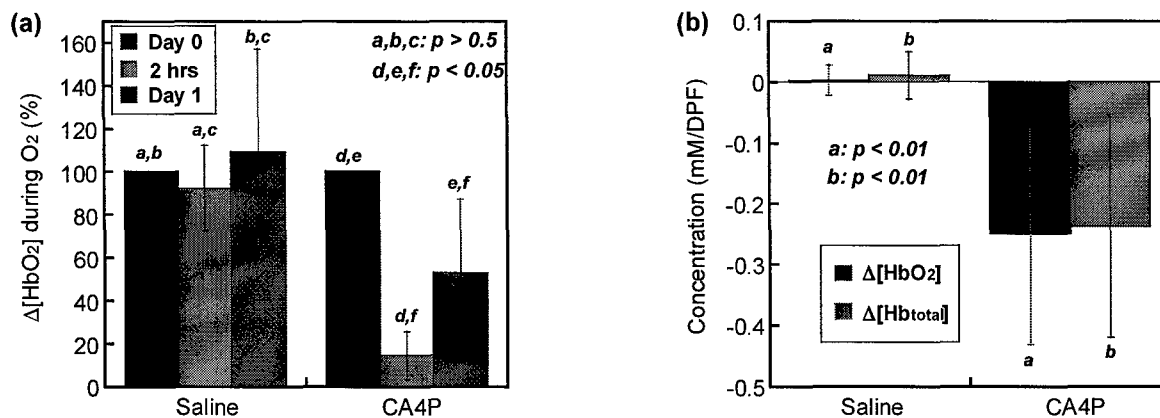


Figure 14. (a) Percentage of changes in  $\Delta[\text{HbO}_2]$  from rat breast tumors during oxygen intervention before and after administration of saline and CA4P. (b) Changes in  $\Delta[\text{HbO}_2]$  and  $\Delta[\text{Hb}_{\text{total}}]$  from rat breast tumors during 2 hours after administration of saline and CA4P.

All the results shown in here prove that CA4P has a significant effects in tumor vasculature by showing the decrease of  $\Delta[\text{HbO}_2]$  and  $\Delta[\text{Hb}_{\text{total}}]$  after CA4P administration. It was also observed that tumor vasculature was recovering its function 1 day after CA4P administration by showing the response to oxygen intervention. This indeed proves that NIRS can be used as a tool to monitor the tumor hemodynamic response to vascular disrupting agents including CA4P.

#### 4. Calibration curve of CTX

Obtaining the calibration curve for calculating CTX concentration is essential since we do need to measure the CTX release kinetics from the biodegradable fiber. CTX was dissolved in phosphate buffered saline (PBS) and the optical density was measured with the different CTX concentration by diluting the original CTX solution. We found the major absorption peak of CTX solution at 212 nm and plotted the change of optical density values with the change in CTX solution as shown in Fig. 15. The fabrication of drug embedded biodegradable fiber will be fabricated at TissueGen Inc. (Dallas, TX) which established by Dr. Kevin Nelson (one of the collaborators in this project).

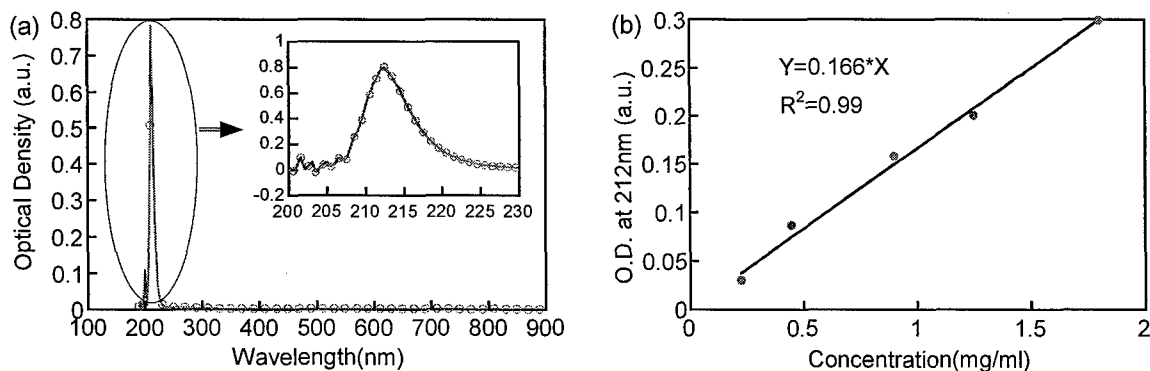


Figure 15. (a) Absorption spectra of CTX solution with the concentration of CTX at 7.5 mg/ml. (b) a calibration curve obtained for a low concentration of CTX.

### Key Research Accomplishments:

- a. Observed the changes of tumor volume and body weight of rats during the expanded cyclophosphamide chemotherapy from the first year. This clearly showed the response of tumor to the chemotherapy.
- b. Investigated the dynamic response of tumor vascular  $\Delta[\text{HbO}_2]$  to oxygen intervention before and after cyclophosphamide administration. The ratios of  $\gamma_1/\gamma_2$  and  $f_1/f_2$  have been changed during therapy, indicating that changes in hemodynamics of  $\Delta[\text{HbO}_2]$  during oxygen intervention before and after cyclophosphamide can be applied to find the efficacy of chemotherapeutic agent.
- c. Investigated the effects of dose in tumor response during CTX treatments. The Metronomic low dose CTX treatment showed less toxicity from the chemotherapy and better treatment efficacy compared to a single high dose CTX treatment.
- d. The dependency of chemotherapy on tumor volume was studied by applying a single high dose of CTX administration. There were similar features observed from both small and large tumor volume groups under CTX treatment. However, further studies are needed to conclude at this point.
- e. Monitored the effect of vascular disrupting agent on tumor hemodynamics by observing the changes of  $\Delta[\text{HbO}_2]$ ,  $\Delta[\text{Hb}]$  and  $\Delta[\text{Hb}_{\text{total}}]$  after CA4P administration. CA4P could significantly reduced blood flow and thus blood volume and oxygenation in tumors, and the tumor vascular function recovered slowly at day 1 and 2 after CA4P injection.
- f. Obtained the calibration curve of CTX concentration by measuring the optical density value at 212 nm which will be used to measure drug release kinetics of biodegradable fiber.

### Reportable Outcomes

#### Manuscripts for Peer-reviewed Journals:

- 1) **Jae G. Kim**, Mengna Xia, Hanli Liu, "Extinction coefficients of hemoglobin for near-infrared spectroscopy of tissue", *IEEE Eng. in Med. & Biol. Magazine*, 24(2), 118-121 (2005).
- 2) **Jae G. Kim**, Hanli Liu, "Investigation of bi-phasic tumor oxygen dynamics induced by hyperoxic gas intervention: A numerical study", *Optics Express*, 13, 4465-4475 (2005).  
<http://www.opticsexpress.org/abstract.cfm?URI=OPEX-13-12-4465>
- 3) Yulin Song, **Jae G. Kim**, Ralph P. Mason, Hanli Liu, "Investigation of rat breast tumor oxygen consumption by near infrared spectroscopy," *J. of Physics D: Applied Physics*, in press, (2005).
- 4) **Jae G. Kim**, Hanli Liu, "Investigation of bi-phasic tumor oxygen dynamics induced by hyperoxic gas intervention: The dynamic phantom approach", *Applied Optics*, ready to submit, (2005)

#### Presentations and Proceeding papers:

- 1) **Jae G. Kim**, Dawen Zhao, Ralph P. Mason, and Hanli Liu, "Chemotherapeutic (Cyclophosphamide) Effects on Rat Breast Tumor Hemodynamics Monitored by Multi-Channel NIRS.", *Proc. SPIE-Int. Soc. Opt. Eng.*, 5693, to be published (2005)

## Conclusions

From the work that I have conducted up-to-date, the following conclusions can be drawn.

- a. The effects of chemotherapy dose have been investigated by monitoring the changes in hemodynamic parameters before and after chemotherapy. The results showed that the Metronomic low dose CTX treatment caused less toxicity in tumors and better treatment efficacy compared to a single high dose CTX treatment. Both a single high dose treatment and a metronomic low dose treatment caused a large decrease in  $\Delta[\text{HbO}_2]_{\text{max}}$  during oxygen inhalation, which is consistent with the reduction of tumor size. However, low toxicity was observed in a group with a metronomic low dose CTX treatment compared to the rats under a single high dose treatment. While these two different CTX treatment plans showed a few similar effects on tumor hemodynamics, the tumor hemodynamics at day 6 from the metronomic low dose CTX treatment still showed a bi-exponential feature and also a relatively high maximum  $\Delta[\text{HbO}_2]$  compared to that observed from a tumor at day 5 after a single high dose CTX treatment. This may imply that the metronomic low dose CTX treatment caused less disruption in tumor vasculature while it still gave great therapeutic effects on rat breast tumors.
- b. We also have investigated the effects of tumor size on tumor hemodynamics changes during a single high dose CTX treatment. Both a small and a large tumor groups showed a similar trend of changes in time constant values from the rapid increase part of  $\Delta[\text{HbO}_2]$  during the oxygen intervention ( $\tau_1$ ). The  $\tau_1$  values were decreased after a CTX treatment until the  $\Delta[\text{HbO}_2]$  could be fit well with a mono exponential model. Since time constant values are related to tumor perfusion rate or more precisely blood flow velocity, the decrease of  $\tau_1$  values implies the increase of blood flow velocities in the well-perfused region. All the rats in a small tumor group failed to survive 6 days after a single high dose CTX treatment while a few rats in a large tumor group did survive even 8 days after the CTX treatment. This could be possibly caused by a difference in rat body weight, but needs to be studied further. All of our data obtained in Year 2 support that measuring hemodynamics of breast tumor during gas intervention can be used for monitoring the efficacy of cancer therapy, such as radiation therapy, photodynamic therapy, and chemotherapy.
- c. The effects of combretastatin on tumor hemodynamics have been studied. It was observed that tumor blood oxygenation and blood volume were significantly decreased right after CA4P administration. We have given another oxygen intervention 2 hours after CA4P injection, but little responses of tumor  $\Delta[\text{HbO}_2]$  were observed which represent tumor vasculature lost its function. The respiratory challenge was applied again at day 1 after CA4P administration and the results showed that tumor vasculature was slowly recovering its function which became clearer at day 2 after CA4P administration. This study also proves that NIRS can be a great tool to monitor the effects of vascular disrupting/modifying agents on tumors.
- d. The calibration curve for a CTX concentration has been obtained by correlating the optical density values with the concentrations of CTX. This curve will be used for measuring the CTX release rate from the biodegradable fiber.

## Reference

---

1. Jae G. Kim, Hanli Liu, "Investigation of bi-phasic tumor oxygen dynamics induced by hyperoxic gas intervention: A numerical study", *Optics Express*, **13**, 4465-4475 (2005).  
<http://www.opticsexpress.org/abstract.cfm?URI=OPEX-13-12-4465>
2. Jae G. Kim and Hanli Liu, "Investigation of bi-phasic tumor oxygen dynamics induced by hyperoxic gas intervention: The dynamic phantom approach", *Applied Optics*, ready to submit, (2005)
3. D. W. Siemann, D. J. Chaplin, and M. R. Horsman, "Vascular-targeting therapies for treatment of malignant disease," *Cancer*, **100**(12), 2491-2499 (2004)
4. M. Kragh, B. Quistorff, M.R. Horsman, P.E. Kristjansen, "Acute effects of vascular modifying agents in solid tumors assessed by noninvasive laser Doppler flowmetry and near infrared spectroscopy," *Neoplasia*, **4**(3), 263-267 (2002)

## List of Appendices

- 1) **Jae G. Kim**, Mengna Xia, Hanli Liu, "Extinction coefficients of hemoglobin for near-infrared spectroscopy of tissue", *IEEE Eng. in Med. & Biol. Magazine*, **24**(2), 118-121 (2005).
- 2) Yulin Song, **Jae G. Kim**, Ralph P. Mason, Hanli Liu, "Investigation of rat breast tumor oxygen consumption by near infrared spectroscopy," *J. of Physics D: Applied Physics*, in press, (2005).
- 3) **Jae G. Kim**, Hanli Liu, "Investigation of bi-phasic tumor oxygen dynamics induced by hyperoxic gas intervention: A numerical study", *Optics Express*, **13**, 4465-4475 (2005).  
<http://www.opticsexpress.org/abstract.cfm?URI=OPEX-13-12-4465>
- 4) **Jae G. Kim**, Hanli Liu, "Investigation of bi-phasic tumor oxygen dynamics induced by hyperoxic gas intervention: The dynamic phantom approach", *Applied Optics*, ready to submit, (2005)
- 5) **Jae G. Kim**, Dawen Zhao, Ralph P. Mason, and Hanli Liu, "Chemotherapeutic (Cyclophosphamide) Effects on Rat Breast Tumor Hemodynamics Monitored by Multi-Channel NIRS.", *Proc. SPIE-Int. Soc. Opt. Eng.*, **5693**, in press, (2005)

## extinction coefficients of hemoglobin for near-infrared spectroscopy of tissue

Jae G. Kim, Mengna Xia,  
and Hanli Liu

**E**xtinction coefficients of hemoglobin have been studied for five decades by clinical chemists and biochemists, particularly for laboratory spectrophotometric measurements. A representative list of literature can be found in [1]–[12], and the studies on the temperature dependence of extinction coefficients of hemoglobin can be found in [13] and [14].

However, during the last ten to 15 years, near infrared spectroscopy (NIRS) and imaging for tissue vascular oxygenation, breast tumor detection, and functional brain imaging have been intensively developed for in vivo measurements by groups of physicists, biomedical engineers, and mathematicians. In the approach of NIRS, NIR light in the wavelength range of 650–900 nm is utilized to illuminate tissue in vivo, and the transmitted or reflected light through tissue is recorded for the quantification of hemoglobin concentrations of the measured tissue vasculature. In order to achieve mathematical conversion from the detected light intensity at different wavelengths to hemoglobin concentration, extinction coefficients of hemoglobin,  $\epsilon$ , must be used.

While the engineers and physicists working in the NIR field have found the correct  $\epsilon$  values to use, there has been controversy on what  $\epsilon$  values should be used for in vivo NIRS in comparison with the conventional  $\epsilon$  that most biochemists have used in the laboratories for in vitro measurements. The purpose of this article is to address this issue and help biomedical engineers and physicists gain a better understanding of  $\epsilon$  to be used for NIRS and NIR imaging.

### Spectrophotometric Measurements to Determine Hemoglobin Concentration

Hemoglobin is a molecule in the red blood cells that has a role of deliver-

ing oxygen to tissue cells. Hemoglobin is composed of four heme groups and a protein group, known as a globin. Historically, for spectrophotometric experiments, biological chemists and biochemists utilized Beer-Lambert's law and developed the notation of absorbance to express light absorption as a function of hemoglobin concentration as given in [1]–[5]:

$$OD = \text{Log}(I_0/I) = \epsilon c L \quad (1)$$

where OD is the optical density,  $I_0$  is the light intensity of incident light,  $I$  is the light intensity of transmitted light,  $\epsilon$  is the extinction coefficient of hemoglobin,  $c$  is the concentration of hemoglobin, and  $L$  is the length of light path through solution.

When the measured sample has a mixture of oxygenated and deoxygenated hemoglobin, (1) can be further expanded as [3]–[5],

$$OD^\lambda = \{\epsilon_{\text{Hb}}^\lambda [\text{Hb}] + \epsilon_{\text{HbO}_2}^\lambda [\text{HbO}_2]\} L \quad (2)$$

where  $OD^\lambda$  is the optical density or absorbance at wavelength  $\lambda$  and  $\epsilon_{\text{Hb}}(\lambda)$  and  $\epsilon_{\text{HbO}_2}(\lambda)$  are the extinction coefficients at wavelength  $\lambda$  for molar concentrations of deoxygenated hemoglobin, [Hb], and oxygenated hemoglobin, [HbO<sub>2</sub>], respectively, assuming ferrihemoglobin is minimal. In some references, the light path,  $L$ , was taken as 1 cm without mentioning the definition of  $L$  each time [3]–[5]. Both [HbO<sub>2</sub>] and [Hb] can be determined by measuring the light absorbance at the two specific wavelengths, provided that the values for  $\epsilon_{\text{Hb}}(\lambda)$  and  $\epsilon_{\text{HbO}_2}(\lambda)$  are known, as expressed below.

$$\begin{aligned} [\text{HbO}_2] &= \frac{\epsilon_{\text{Hb}}^{\lambda_2} OD^{\lambda_1} - \epsilon_{\text{Hb}}^{\lambda_1} OD^{\lambda_2}}{L(\epsilon_{\text{Hb}}^{\lambda_2} \epsilon_{\text{HbO}_2}^{\lambda_1} - \epsilon_{\text{Hb}}^{\lambda_1} \epsilon_{\text{HbO}_2}^{\lambda_2})} \end{aligned} \quad (3)$$

$$\begin{aligned} [\text{Hb}] &= \frac{\epsilon_{\text{HbO}_2}^{\lambda_2} OD^{\lambda_1} - \epsilon_{\text{HbO}_2}^{\lambda_1} OD^{\lambda_2}}{L(\epsilon_{\text{Hb}}^{\lambda_1} \epsilon_{\text{HbO}_2}^{\lambda_2} - \epsilon_{\text{Hb}}^{\lambda_2} \epsilon_{\text{HbO}_2}^{\lambda_1})} \end{aligned} \quad (4)$$

It follows that changes in [Hb] and [HbO<sub>2</sub>] can be consequently given as

$$\begin{aligned} \Delta[\text{HbO}_2] &= \frac{\epsilon_{\text{Hb}}^{\lambda_2} \Delta OD^{\lambda_1} - \epsilon_{\text{Hb}}^{\lambda_1} \Delta OD^{\lambda_2}}{L(\epsilon_{\text{Hb}}^{\lambda_2} \epsilon_{\text{HbO}_2}^{\lambda_1} - \epsilon_{\text{Hb}}^{\lambda_2} \epsilon_{\text{HbO}_2}^{\lambda_2})} \end{aligned} \quad (5)$$

$$\begin{aligned} \Delta[\text{Hb}] &= \frac{\epsilon_{\text{HbO}_2}^{\lambda_2} \Delta OD^{\lambda_1} - \epsilon_{\text{HbO}_2}^{\lambda_1} \Delta OD^{\lambda_2}}{L(\epsilon_{\text{Hb}}^{\lambda_1} \epsilon_{\text{HbO}_2}^{\lambda_2} - \epsilon_{\text{Hb}}^{\lambda_2} \epsilon_{\text{HbO}_2}^{\lambda_1})} \end{aligned} \quad (6)$$

$$\Delta[\text{Hb}]_{\text{total}} = \Delta[\text{Hb}] + \Delta[\text{HbO}_2], \quad (7)$$

where  $\Delta OD^\lambda$  represents a change in optical density at the specific wavelength,  $\lambda$ , and equals  $\log(I_B/I_T)$ .  $I_B$  and  $I_T$  correspond to light intensities measured under the baseline and transient conditions.

These spectrophotometric calculations seem straightforward mathematically and have been used for several decades by biochemists to quantify [Hb] and [HbO<sub>2</sub>] in the laboratory measurements. However, close attention must be paid to the definition and accuracy of  $\epsilon$  since biochemical details in obtaining  $\epsilon$

values give rise to the different quantification of hemoglobin concentration. In early publications on spectrophotometry of hemoglobin [3], it was clearly stated that all extinction coefficients were expressed on a heme basis, using a term of equivalent, where per equivalent of hemoglobin was assumed to be 66,800/4 or 16,700 gm, i.e., one-quarter of the molecular weight of the hemoglobin molecule [12]. While spectroscopic absorption measurements became a popular methodology for biochemists to quantify [Hb] and [HbO<sub>2</sub>] in laboratories [5], [6], [12] the notation of extinction coefficients being based on one heme group (or per equivalent) gradually has not been mentioned and has become conventionally understood by biological chemists for the last two to three decades.

#### Near-Infrared Spectroscopy Used to Determine Hemoglobin Concentration

For the last 15 or more years, significant research efforts have been conducted using NIRS for *in vivo* quantification of hemoglobin concentrations from intact living tissues. At the early stage of development, direct utilization of (3) and (4) was performed to obtain values or changes of oxygenated and deoxygenated hemoglobin concentration from living tissues *in vivo* [15]–[18], without particularly noticing that most of the  $\epsilon$  values published in biological literature were extinction coefficients for hemoglobin per equivalent (or per one heme of hemoglobin). Such confusion was propagated in some recent publications [19], including our own studies [20]–[22], where the  $\epsilon$  values given by Zijlstra et al. have been applied [7].

It gradually becomes clear to the authors that for NIRS of hemoglobin quantification, a factor of four needs to be multiplied by the  $\epsilon$  values published by the conventional biochemistry methods. This is a conversion factor to account for four hemes per hemoglobin molecule, which has been

During the last ten to 15 years, near infrared spectroscopy (NIRS) and imaging for tissue vascular oxygenation, breast tumor detection, and functional brain imaging have been intensively developed for *in vivo* measurements.

demonstrated by Mark Cope [10]. In this way, more meaningful results for concentrations of [Hb] and [HbO<sub>2</sub>] can be arrived from the NIR absorption measurements.

Furthermore, accurate determination of [Hb] and [HbO<sub>2</sub>], or  $\Delta$ [Hb] and  $\Delta$ [HbO<sub>2</sub>], is highly sensitive to the accuracy of  $\epsilon$  values, and intensive studies have been conducted over decades on how to determine accurate  $\epsilon$  values [6]–[8], [13]–[14]. The  $\epsilon$  values used in our earlier publications were obtained using data interpolation from Zijlstra's  $\epsilon$  table [7]. However, such data interpolation for  $\epsilon$  at different wavelengths contained potential errors because of the nonlinearity of  $\epsilon$ . Therefore, a calibration procedure was necessary and correction factors had to be applied in our earlier algorithm development [21]. On the other hand, Mark Cope has generated a complete  $\epsilon$  table at each wavelength between 650 and 999 nm, while taking four hemes into consideration. Such an  $\epsilon$  table has been recently well accepted and used [23]–[25].

#### Comparison of Published Extinction Coefficients for NIRS Given by Two Groups

Since Hoppe-Seyley first described the visible bands of oxyhemoglobin in 1862 [26], numerous reports on hemo-

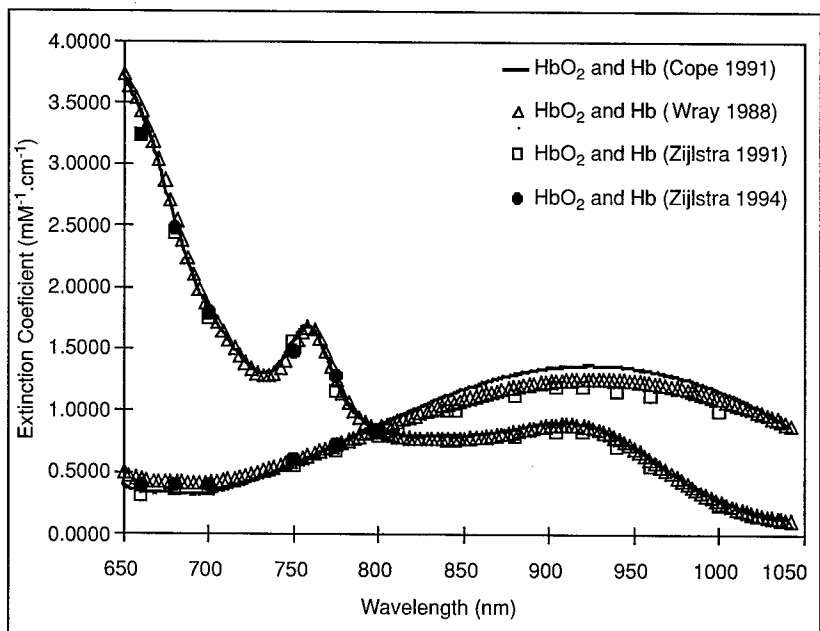


Fig. 1. Absorption spectra of oxy- and deoxyhemoglobin from Wray (9), Cope (10), and Zijlstra (7), (8).

**Table 1: Hemoglobin extinction coefficients from two different sources.**

Wave-length (nm)	$\epsilon_{\text{Hb}}$ (mM <sup>-1</sup> ·cm <sup>-1</sup> )				$\epsilon_{\text{HbO}_2}$ (mM <sup>-1</sup> ·cm <sup>-1</sup> )			
	Human (7)	Human (8)	Human (10)	Difference (Absolute)	Human (7)	Human (8)	Human (10)	Difference (Absolute)
750	0.39	0.37	0.3865	0.0165	0.14	0.15	0.1374	0.0126
758		0.354	0.4205	0.0665		0.1596	0.1494	0.0102
775	0.29	0.32	0.3120	0.008	0.17	0.18	0.1759	0.0041
785		0.276	0.2494	0.0266		0.192	0.192	0
800	0.20	0.21	0.2099	0.0001	0.20	0.21	0.2163	0.0063
805	0.20		0.2037		0.21		0.2243	
840	0.19		0.1954		0.25		0.2768	

globin absorption spectra have appeared in the literature. However, only a few have tabular forms of hemoglobin extinction coefficients. In particular, two groups have reported tabular forms of hemoglobin extinction coefficients in a broad range of the NIR spectrum. Zijlstra et al. reported  $\epsilon$  values for human blood [7], followed by another publication for updated human  $\epsilon$  values with a comparison to those of rat blood [8]. Moreover, Cope has generated a complete  $\epsilon$  table at each wavelength between 650 and 999 nm, while taking four hemes into account for in vivo NIRS measurements. Cope also compared his own experiments with other previous reports, finding that the isobestic point of hemoglobin is shifted to  $798 \pm 1.5$  nm from 800 nm reported by Horecker [1], 805 nm by Barlow [27] and 815 nm by van Assendelft [28].

It is worthwhile to note that the determination of  $\epsilon$  values has resulted in a range of accuracy claims, even for values reported from the same group. For example, according to Zijlstra et al., a value of  $\epsilon_{\text{Hb}}$  at 560 nm in [29] was  $12.72$  (mM<sup>-1</sup>·cm<sup>-1</sup>), while it was later changed to  $13.09$  (mM<sup>-1</sup>·cm<sup>-1</sup>) in [7]; a value of  $\epsilon_{\text{HbO}_2}$  at 630 nm was  $0.11$  (mM<sup>-1</sup>·cm<sup>-1</sup>) as given in [7], while it was also reported as  $0.14$  (mM<sup>-1</sup>·cm<sup>-1</sup>) in [8]. From Cope's group, their published reports show that

$\epsilon_{\text{Hb}}$  and  $\epsilon_{\text{HbO}_2}$  at 752 nm are  $1.574$  (mM<sup>-1</sup>·cm<sup>-1</sup>) and  $0.608$  (mM<sup>-1</sup>·cm<sup>-1</sup>), respectively, as given in [9], while the corresponding  $\epsilon$  values are  $1.5938$  (mM<sup>-1</sup>·cm<sup>-1</sup>) and  $0.5613$  (mM<sup>-1</sup>·cm<sup>-1</sup>) in [10]. A complete comparison of  $\epsilon$  values based on [7]–[10] by Zijlstra et al., Wray et al., and Cope is plotted in Figure 1, showing the similarities and differences among the reported extinction coefficients of oxy- and deoxyhemoglobin. Notice that the values plotted from Zijlstra's group have been multiplied by a factor of four to account for four hemes per hemoglobin molecule for in vivo measurements. It is obvious that certain variations among different sets of  $\epsilon$  values exist, while the basic trends are the same.

Table 1, on the other hand, shows the tabular form of hemoglobin extinction coefficients from these two groups. Extinction coefficients in the left two columns of  $\epsilon_{\text{Hb}}$  and  $\epsilon_{\text{HbO}_2}$  are from Zijlstra's two reports [7], [8] and those in the third column of  $\epsilon_{\text{Hb}}$  and  $\epsilon_{\text{HbO}_2}$  are from Cope's report [10]. Since the tabular form of extinction coefficients from Zijlstra does not have values of 758 and 785 nm, the extinction coefficients of 758 and 785 nm were obtained by linear interpolation between 750 and 775 nm and between 775 and 800 nm, respectively. The hemoglobin extinction coefficients from Cope were divided by four to be

“per equivalent” so that they could be compared to those from Zijlstra et al. The differences listed in the last column are the differences between Cope's  $\epsilon$  values and the values from Zijlstra et al [8].

While the differences in  $\epsilon$  values seem small among the published data, they can result in  $\sim 20\%$  variation in quantification of hemoglobin concentration, i.e., [Hb], [HbO<sub>2</sub>], and [Hb]<sub>total</sub> for the NIRS determined values. The error range varies, depending on the actual wavelengths used. We are currently conducting more quantitative error analysis to demonstrate the importance of accurate  $\epsilon$  for NIRS. Meanwhile, we wish in this report to help biomedical engineers better understand the extinction coefficients of hemoglobin and to further draw attention to the dependence of NIRS accuracy on the extinction coefficients of hemoglobin.

#### Acknowledgments

This work was supported in part by the U.S. Department of Defense Breast Cancer Research grants of DAMD17-03-1-0353 (JGK), W81XWH-04-1-0411 (MX), and DAMD17-00-1-0459 (HL).

#### References

[1] B.L. Horecker, “The absorption spectra of hemoglobin and its derivatives in the visible and near

infrared regions," *J. Biol. Chem.*, vol. 148, no. 1, pp. 173-183, 1943.

[2] E.J. van Kampen and W.G. Zijlstra, "Determination of hemoglobin and its derivatives," *Adv. Clin. Chem.*, vol. 8, pp. 141-187, 1965.

[3] R. Benesch, G. Macduff, and R.E. Benesch, "Determination of oxygen equilibria with a versatile new tonometer," *Anal. Biochem.*, vol. 11, no. 1, pp. 81-87, 1965.

[4] R.E. Benesch, R. Benesch, and S. Yung, "Equations for the spectrophotometric analysis of hemoglobin mixtures," *Anal. Biochem.*, vol. 55, no. 1, pp. 245-248, 1973.

[5] O.W. van Assendelft and W.G. Zijlstra, "Extinction coefficients for use in equations for the spectrophotometric analysis of haemoglobin mixtures," *Anal. Biochem.*, vol. 69, pp. 43-48, 1975.

[6] W.G. Zijlstra, A. Buursma, and A. Zwart, "Molar absorptivities of human hemoglobin in the visible spectral range," *J. Appl. Physiol.: Respirat. Environ. Exercise Physiol.*, vol. 54, no. 5, pp. 1287-1291, 1983.

[7] W.G. Zijlstra, A. Buursma, and W.P. Meeuwsc-van der Roest, "Absorption spectra of human fetal and adult oxyhemoglobin, deoxyhemoglobin, carboxyhemoglobin, and methemoglobin," *Clin. Chem.*, vol. 37, no. 9, pp. 1633-1638, 1991.

[8] W.G. Zijlstra, A. Buursma, H.E. Falke, and J.F. Catsburg, "Spectrophotometry of hemoglobin: Absorption spectra of rat oxyhemoglobin, deoxyhemoglobin, carboxyhemoglobin, and methemoglobin," *Comp. Biochem. Physiol.*, vol. 107B, no. 1, pp. 161-166, 1994.

[9] S. Wray, M. Cope, D.T. Delpy, J.S. Wyatt, and E. Osmund R. Reynolds, "Characterization of the near infrared absorption spectra of cytochrome a3 and haemoglobin for the non-invasive monitoring of cerebral oxygenation," *Biochimica et Biophysica Acta*, vol. 933, no. 1, pp. 184-192, 1988.

[10] M. Cope, "The application of near infrared spectroscopy to non invasive monitoring of cerebral oxygenation in the newborn infant," Ph.D. thesis, Appendix B, pp. 316-323, University College London, 1991.

[11] S.J. Matcher, C.E. Elwell, C.E. Cooper, M. Cope, and D.T. Delpy, "Performance comparison of several published tissue near-infrared spectroscopy algorithms," *Anal. Biochem.*, vol. 227, no. 1, pp. 54-68, 1995.

[12] Y. Mendelson and J.C. Kent, "Variations in optical absorption spectra of adult and fetal hemoglobins and its effect on pulse oximetry," *IEEE Trans. Biomed. Eng.*, vol. 36, no. 8, pp. 844-848, 1989.

[13] L. Cordone, A. Cupane, M. Leone and E. Vitrano, "Optical absorption spectra of deoxy- and oxyhemoglobin in the temperature range 300-20 K," *Biophys. Chem.*, vol. 24, no. 3, pp. 259-275, 1986.

[14] J.M. Steinke and A.P. Shepherd, "Effects of temperature on optical absorbance spectra of oxy-, carboxy-, and deoxyhemoglobin," *Clin. Chem.*, vol. 38, no. 7, pp. 1360-1364, 1992.

[15] E.M. Sevcik, B. Chance, J. Leigh, S. Nioka, and M. Maris, "Quantitation of time- and frequency-resolved optical spectra for the determination of tissue oxygenation," *Anal. Biochem.*, vol. 195, no. 2, pp. 330-351, 1991.

[16] M. Miwa, Y. Ueda, and B. Chance, "Development of time resolved spectroscopy system for quantitative non-invasive tissue measurement," *Proc. SPIE-Int. Soc. Opt. Eng.*, vol. 2389, p. 142, 1995.

[17] H. Liu, A.H. Hielscher, F.K. Tittel, S.L. Jacques, and B. Chance, "Influence of blood vessels on the measurement of hemoglobin oxygenation as determined by time-resolved reflectance spectroscopy," *Med. Phys.*, vol. 22, no. 8, pp. 1209-1217, 1995.

[18] S. Fantini, M.A. Franceschini-Fantini, J.S. Maier, S.A. Walker, B. Barbieri, and E. Gratton, "Frequency-domain multichannel optical detector for noninvasive tissue spectroscopy and oximetry," *Opt. Eng.*, vol. 34, no. 1, pp. 32-42, 1995.

[19] C.D. Kurth and W.S. Thayer, "A multiwavelength frequency-domain near-infrared cerebral oximeter," *Phys. Med. Biol.*, vol. 44, no. 3, pp. 727-740, 1999.

[20] H. Liu, Y. Song, K.L. Worden, X. Jiang, A. Constantinescu, and R.P. Mason, "Noninvasive investigation of blood oxygenation dynamics of tumors by near infrared spectroscopy," *Appl. Opt.*, vol. 39, no. 28, pp. 5231-5243, 2000.

[21] J.G. Kim, Y. Song, D. Zhao, A. Constantinescu, R.P. Mason, and H. Liu, "Interplay of tumor vascular oxygenation and tumor pO<sub>2</sub> observed using near infrared spectroscopy, an oxygen needle electrode, and <sup>19</sup>F MR pO<sub>2</sub> mapping," *J. Biomed. Opt.*, vol. 8, no. 1, pp. 53-62, 2003.

[22] Y. Gu, V. Bourke, J.G. Kim, A. Constantinescu,

R.P. Mason, and H. Liu, "Dynamic response of breast tumor oxygenation to hyperoxic respiratory challenge monitored with three oxygen-sensitive parameters," *Appl. Opt.*, vol. 42, no. 16, pp. 2960-2967, 2003.

[23] J.B. Fishkin, O. Coquoz, E.R. Anderson, M. Brenner, and B.J. Tromberg, "Frequency-domain photon migration measurements of normal and malignant tissue optical properties in a human subject," *Appl. Opt.*, vol. 36, no. 1, pp. 10-20, 1997.

[24] E.L. Hull, D.L. Conover, and T. Foster, "Carbogen-induced changes in rat mammary tumour oxygenation reported by near infrared spectroscopy," *British J. of Cancer*, vol. 79, no. 11/12, pp. 1709-1716, 1999.

[25] D.A. Boas, M.A. Franceschini, A.K. Dunn, and G. Strangman, "Noninvasive imaging of cerebral activation with diffuse optical tomography," in *In-vivo Optical Imaging of Brain Function*, R.D. Frostig, Ed. New York: CRC Press, 2000.

[26] H.S. Newcomer, "Absorption spectra of acid hematin, oxyhemoglobin, and carbon monoxide hemoglobin," *J. Biol. Chem.*, vol. 37, no. 3, pp. 465-496, 1919.

[27] R.B. Barlow and M.L. Polanyi, "Absorption measurements for oxygenated and reduced hemoglobin in the range 0.6-1.88 microns," *Clin. Chem.*, vol. 8, no. 1, pp. 67-71, 1962.

[28] O.W. van Assendelft, "Spectrophotometry of haemoglobin derivatives," Ph.D. thesis, Univ. of Groningen, The Netherlands, 1970.

[29] W.G. Zijlstra and A. Buursma, "Spectrophotometry of hemoglobin: A comparison of dog and man," *Comp. Biochem. Physiol.*, vol. 88B, no. 1, pp. 251-255, 1987.

**Address for Correspondence:** Hanli Liu, Joint Graduate Program in Biomedical Engineering, The University of Texas at Arlington and The University of Texas Southwestern Medical Center at Dallas Arlington, TX 76019 USA. Phone: +1 817 272 2054. Fax: +1 817 272 2251. E-mail: hanli@uta.edu.

## COMAR Reports *(continued from page 117)*

membership and by the IEEE EMBS Executive Committee.

### Sources and Further Reading

[1] IEEE C95.1-1991, Standard for Safety Levels with Respect to Human Exposure to Radio Frequency Electromagnetic Fields, 3 kHz to 300 GHz, (1999 edition).

[2] International Commission on Non-Ionizing Radiation Protection, "Guidelines for limiting exposure to time-varying electric, magnetic and electro-

magnetic fields (up to 300 GHz)," *Health Physics*, vol. 74, no. 4, pp. 494-522, 1998.

[3] J. M. Osepchuk and R. C. Petersen, "Safety standards for exposure to electromagnetic fields," *IEEE Microwave Magazine*, vol. 2, no. 2, pp. 57-69, June 2001.

[4] "Reviews of the Effects of RF Fields on Various Aspects of Human Health," *Bioelectromagnetics*, vol. 24, no. S6, 2003.

[5] *Welcome to IEEE standards development online* [Online]. Available: <http://standards.ieee.org/resources/development/index.html>

[6] *IEEE international committee on electromagnetic safety* [Online]. Available: <http://grouper.ieee.org/groups/sec28/>

[7] K. R. Foster, "Limiting Technology: Issues in Setting Exposure Guidelines for Radiofrequency Energy," in Ma Jian-Guo, Ed. 3rd Generation Mobile Communication Systems: Future Developments and Advanced Topics, Springer, Sept. 2003.

[8] *Framework for harmonization of standards* [Online]. Available: <http://www.who.int/peh-emf/standards/framework/cn/>

# Investigation of Rat Breast Tumor Oxygen Consumption by Near Infrared Spectroscopy

Yulin Song<sup>+ $\phi$</sup> , Jae G. Kim<sup>+</sup>, Ralph P. Mason <sup>$\phi$</sup> , and Hanli Liu<sup>+ $\#$</sup>

<sup>+</sup>Joint Graduate Program in Biomedical Engineering  
University of Texas at Arlington/University of Texas Southwestern Medical Center at Dallas  
Arlington, TX 76019

<sup>$\phi$</sup> Advanced Radiological Sciences, Department of Radiology  
University of Texas Southwestern Medical Center at Dallas  
Dallas, TX 75390

# The corresponding author's information:

Hanli Liu  
Joint Program of Biomedical Engineering  
P.O. Box 19138  
University of Texas at Arlington  
Arlington, TX, USA 76019  
Phone: (817) 272-2054  
Fax: (817) 272-2251  
e-mail: [hanli@uta.edu](mailto:hanli@uta.edu)

**Short title:** Rat Tumor Oxygen Consumption by Near Infrared Spectroscopy

## ABSTRACT

This study develops a mathematical model for calculating tumor oxygen consumption rate and investigates the correlation with tumor volume. Near-infrared spectroscopy (NIRS) was used to measure changes of oxygenated hemoglobin concentration ( $\Delta[\text{HbO}_2]$ ) before and after potassium chloride (KCl) induced cardiac arrest. Measurements were made in five 13762NF mammary adenocarcinomas implanted in female adult Fisher 344 rats, while the anesthetized rats breathed air. After 5-10 minutes of baseline NIRS measurement, KCl overdose was administered i.v. in the tail. NIRS showed a significant drop in tumor vascular oxygenation immediately following KCl induced cardiac arrest. The tumor oxygen consumption rate was calculated by fitting the model to the measured  $\Delta[\text{HbO}_2]$  data, and a relationship between tumor oxygen consumption rate and tumor volume was analyzed using linear regression. A strong negative linear relationship was found between the mean tumor oxygen consumption rate and tumor volume. This study demonstrates that the NIRS can provide an efficient and real-time approach to quantify tumor oxygen consumption rate, while further development is required to make it non-invasive.

**Key Words:** rat breast tumor, tumor oxygen consumption, near infrared spectroscopy, tumor vascular oxygenation.

## 1. Introduction

The physiology of solid tumors is highly complex and largely associated with multiple physiological parameters, such as tumor blood flow, blood volume, blood oxygen saturation, tissue oxygen tension ( $pO_2$ ), and oxygen consumption. It is known that tumor microvasculature is often abnormal, leaky, having distended capillaries and sluggish flow [1,2,3]. Hypoxic regions exist in almost all solid tumors, and tumor oxygenation affects greatly tumor growth, malignant progressions, tumor prognosis, and therapy efficacy. Therefore, understanding the various physiological parameters of solid tumors is significant for better strategies and efficacy of treating solid tumors in the near future.

Over the past decade, substantial studies have been conducted in both laboratory and clinical settings to non-invasively investigate tissue/tumor vascular oxygenation [4,5,6,7,8] and blood flow [9,10] using near infrared (NIR) spectroscopy (NIRS) and imaging. Several studies were also reported on tumor  $pO_2$  heterogeneity [11] and on comparisons between tumor vascular oxygenation and tumor  $pO_2$  using animal tumor models during hyperoxic gas interventions [12,13]. Regarding tissue oxygen consumption, considerable efforts have been made in developing techniques for measuring skeletal muscle oxygen consumption ( $\dot{V}O_2$ ) during rest and exercise with and without vascular occlusion [14,15,16,17,18]. More recently, extensive attention has been paid to quantitative relationships among neuronal activity, oxygen metabolism, and hemodynamic responses [19,20,21,22]. While various mathematical models for computing or interpreting hemoglobin concentrations have been proposed [23,24,25], the approaches for calculations of oxygen consumptions in human muscles versus in the brain during cortical activation are quite diversified.

In principle, tumor oxygen consumption is quite different from regular muscle or brain oxygen consumptions, which warrants separate studies targeting on tumor oxygen consumption. In this regard, little is known about tumor oxygen consumption even in animal models or its relationship to tumor kinetic parameters and tumor volume. Some earlier studies indicated that oxygen consumption rates of breast tumors *in vivo* were intermediate between normal tissues with low metabolic rates and normal tissues with quite high activities [26]. Steen *et al.* [27] found out that the oxygen consumption rate of rat brain was higher than that of 9L gliosarcoma by comparing pre-sacrifice and post-sacrifice  $sO_2$  (hemoglobin oxygen saturation) values. While a few reports recently appeared in literature on determination of tumor oxygen consumption rate through *in vitro* measurements using a standard Clark-type oxygen electrode [10,28], overall knowledge and investigation on tumor oxygen consumption is still limited and much needed.

It would be desirable to develop a non-invasive technique or methodology to quantify tumor oxygen consumption rate; however, it would be still acceptable to conduct invasive studies if significant knowledge on tumor oxygen consumption can be explored. In this paper, we report a novel methodology to quantify tumor oxygen consumption rate using an invasive approach, to be done by the end of regular tumor experiments when the animals had to be sacrificed. In experiment, we took the NIR readings from the animal tumors during potassium chloride (KCl) induced cardiac arrest (total global ischemia), as a procedure for animal euthanasia. In theory, we have developed a simple mathematical model based on Fick's Law of diffusion to describe hemokinetics of tumor vascular oxygenated hemoglobin concentration,  $[HbO_2]$ . The model describes changes in tumor oxyhemoglobin concentration,  $\Delta[HbO_2]$ , as a function of time. Specifically, the mathematical model is developed in such a way that the measured  $\Delta[HbO_2]$  is directly associated with the tumor oxygen consumption rate, which can be further correlated with

the tumor volume. In this paper, we will report 1)  $\Delta[\text{HbO}_2]$  measurement using NIRS from the animal tumor models, in common with our previous work [12,29], 2) the development of the mathematical model for computing tumor oxygen consumption rate, and 3) the investigation of relationship between tumor oxygen consumption rate and tumor volume.

## 2. Materials and Methods

### 2.1 Calculations of Tumor $[\text{HbO}_2]$ and $[\text{Hb}]_{\text{total}}$

The principle of tissue NIRS is that concentrations of oxygenated hemoglobin,  $[\text{HbO}_2]$  and deoxygenated hemoglobin,  $[\text{Hb}]$ , respectively, are the only significant absorbing materials in tissue within the NIR range (700-900 nm). When the measured sample, such as tumor, has a mixture of oxygenated and deoxygenated hemoglobin, the modified Beer-Lambert law can be written as [30,31,32]

$$\text{OD}^\lambda = \{\varepsilon_{\text{Hb}}^\lambda [\text{Hb}] + \varepsilon_{\text{HbO}_2}^\lambda [\text{HbO}_2]\} l, \quad (1)$$

where  $\text{OD}^\lambda$  is the optical density or absorbance at wavelength  $\lambda$ ,  $\varepsilon_{\text{Hb}}^\lambda$  and  $\varepsilon_{\text{HbO}_2}^\lambda$  are the extinction coefficients at  $\lambda$  for molar concentrations of  $[\text{Hb}]$  and  $[\text{HbO}_2]$ , respectively, and  $l$  is the optical path length. By employing two wavelengths at  $\lambda_1$  and  $\lambda_2$ , both  $[\text{HbO}_2]$  and  $[\text{Hb}]$  can be determined by measuring the light absorbance at the two specific wavelengths, provided that the values for  $\varepsilon_{\text{Hb}}^\lambda$  and  $\varepsilon_{\text{HbO}_2}^\lambda$  are known:

$$[\text{HbO}_2] = \frac{\varepsilon_{\text{Hb}}^{\lambda_2} \text{OD}^{\lambda_1} - \varepsilon_{\text{Hb}}^{\lambda_1} \text{OD}^{\lambda_2}}{l(\varepsilon_{\text{Hb}}^{\lambda_2} \varepsilon_{\text{HbO}_2}^{\lambda_1} - \varepsilon_{\text{Hb}}^{\lambda_1} \varepsilon_{\text{HbO}_2}^{\lambda_2})}, \quad (2)$$

$$[\text{Hb}] = \frac{\varepsilon_{\text{HbO}_2}^{\lambda_2} \text{OD}^{\lambda_1} - \varepsilon_{\text{HbO}_2}^{\lambda_1} \text{OD}^{\lambda_2}}{l(\varepsilon_{\text{Hb}}^{\lambda_1} \varepsilon_{\text{HbO}_2}^{\lambda_2} - \varepsilon_{\text{Hb}}^{\lambda_2} \varepsilon_{\text{HbO}_2}^{\lambda_1})}. \quad (3)$$

It follows that changes in  $[\text{Hb}]$  and  $[\text{HbO}_2]$  are given by:

$$\Delta[\text{HbO}_2] = \frac{\varepsilon_{\text{Hb}}^{\lambda_2} \Delta\text{OD}^{\lambda_1} - \varepsilon_{\text{Hb}}^{\lambda_1} \Delta\text{OD}^{\lambda_2}}{l(\varepsilon_{\text{Hb}}^{\lambda_2} \varepsilon_{\text{HbO}_2}^{\lambda_1} - \varepsilon_{\text{Hb}}^{\lambda_1} \varepsilon_{\text{HbO}_2}^{\lambda_2})}, \quad (4)$$

$$\Delta[\text{Hb}] = \frac{\varepsilon_{\text{HbO}_2}^{\lambda_2} \Delta\text{OD}^{\lambda_1} - \varepsilon_{\text{HbO}_2}^{\lambda_1} \Delta\text{OD}^{\lambda_2}}{l(\varepsilon_{\text{Hb}}^{\lambda_1} \varepsilon_{\text{HbO}_2}^{\lambda_2} - \varepsilon_{\text{Hb}}^{\lambda_2} \varepsilon_{\text{HbO}_2}^{\lambda_1})}, \quad (5)$$

where  $\Delta\text{OD}^\lambda$  represents a change in optical density at the specific wavelength,  $\lambda$ , and equals to  $\log(A_B/A_T)$ .  $A_B$  and  $A_T$  correspond to light intensities measured under the baseline and transient conditions.

Equations (4) and (5) seem straightforward mathematically and have been used for several decades by biochemists to quantify  $\Delta[\text{Hb}]$  and  $\Delta[\text{HbO}_2]$  in laboratory spectrophotometric measurements. However, close attention needs to be paid to the values of  $\varepsilon$  for *in vivo* hemoglobin determination, since  $\varepsilon$  values were often expressed on a basis of per heme, whereas the hemoglobin molecule has four hemes. Therefore, there exists a factor of 4 between the commonly published  $\varepsilon$  values and the  $\varepsilon$  values to be used in equations (4) and (5) for *in vivo* measurements [33,34]. Furthermore, the optical pathlength,  $l$ , should be proportional to the source and detector separation,  $d$ , with a differential pathlength factor (DPF) [35,36], i.e.,  $l=d*DPF$ . We previously utilized the  $\varepsilon$  values given by W. G. Zijlstra [37], which were expressed on a heme basis, and assumed that the DPF values were constant at the two wavelengths. For  $\lambda_1=758$  nm and  $\lambda_2=785$  nm, eqs. (4) and (5) gave the following empirical relationships based on system calibration using liquid phantoms [12]:

$$\Delta[\text{HbO}_2] = \frac{-10.63 \cdot \log\left(\frac{A_B}{A_T}\right)^{758} + 14.97 \cdot \log\left(\frac{A_B}{A_T}\right)^{785}}{d}, \quad (6)$$

$$\Delta[\text{Hb}] = \frac{8.95 \cdot \log\left(\frac{A_B}{A_T}\right)^{758} - 6.73 \cdot \log\left(\frac{A_B}{A_T}\right)^{785}}{d}, \quad (7)$$

$$\begin{aligned} \Delta[\text{Hb}]_{\text{total}} &= \Delta[\text{Hb}] + \Delta[\text{HbO}_2] \\ &= \frac{-1.68 \cdot \log\left(\frac{A_B}{A_T}\right)^{758} + 8.24 \cdot \log\left(\frac{A_B}{A_T}\right)^{785}}{d}, \quad (8) \end{aligned}$$

The factor 4 in  $\epsilon$  relating to 4 hemes and the DPF values are essentially constants and do not affect dynamic features of tumor  $\Delta[\text{HbO}_2]$ . For simplicity, thus, we did not include them in these equations and used arbitrary units for  $\Delta[\text{Hb}]$  and  $\Delta[\text{HbO}_2]$  since the focus of this study is on relative changes of  $\Delta[\text{HbO}_2]$  between the baseline conditions and response to KCl injection. The error estimation due to the assumption of constant DPF has been given in Ref. 29.

## 2.2 One-Channel NIRS System

A dual-wavelength (at 758 nm and 785 nm), one-channel NIR system (NIM, Inc., Philadelphia, PA) was used (Figure 1). A radio-frequency (rf) source was used to modulate the light intensities of two laser diodes at 140 MHz through a time-sharing system. After the light passed through a bifurcated fiber optic probe, it was transmitted through the tumor tissue and then collected by a second fiber bundle. The light was demodulated by an In-phase and Quadrature-phase chip (I&Q chip), amplified by a photo multiplier tube (PMT), and filtered by a low pass (LP) filter to pass only the DC electronic components. The signals were digitized by an analog-to-digital converter (ADC) and stored in a laptop computer. The I&Q chip served as a frequency mixer, giving high and low (near DC) components. The measured DC electrical signals at the I and Q branches,  $I_{DC}(\lambda)$  and  $Q_{DC}(\lambda)$ , contained the quantities of optical amplitudes,

$A(\lambda)$ , and phase,  $\theta(\lambda)$ , that passed through the tumor tissues [38]. Both  $A(\lambda)$  and  $\theta(\lambda)$  can be recovered through the DC output readings at the I and Q branches, as

$$A(\lambda) = \sqrt{I(\lambda)_{DC}^2 + Q(\lambda)_{DC}^2}, \quad (9a)$$

$$\theta(\lambda) = \tan^{-1}\left(\frac{Q(\lambda)_{DC}}{I(\lambda)_{DC}}\right). \quad (9b)$$

where  $\lambda$  represents the respective wavelengths utilized in the NIR system. Although our NIR system allowed us to quantify both the amplitudes and phase, the phase information was not utilized in the study. The reasons for abandoning  $\theta(\lambda)$  include that 1) the diffusion theory was not valid to use in this case due to the finite size and heterogeneity of solid tumors, and 2) only the modified Beer-Lambert's was applied for the calculation. In the calculation, we employed only the measured values of  $A(\lambda)$  at the two selected wavelengths and substituted them in eqs. (6) to (8) to compute changes in tumor vascular  $[HbO_2]$  and  $[Hb]_{total}$ .

### 2.3 Animal Tumor Model and its Response to KCl Injection

Rat mammary adenocarcinomas 13762NF were implanted in skin pedicles on the forebacks of adult female Fischer 344 rats ( $\sim 250$  g,  $n=5$ ), as described in detail previously [39]. Relatively large tumors ( $\sim 1.2$ - $1.5$  cm in radius or  $\sim 7$ - $14$  cm<sup>3</sup> in tumor volume) were used to ensure that the NIRS interrogated only the tumor tissue rather than the surrounding normal skin tissue, but this corresponds to a typical lower limit of tumor detected in patients. The rats were anesthetized with 200  $\mu$ l ketamine hydrochloride i.p. (100 mg/ml; Aveco, Fort Dodge, IA) and were maintained under general gaseous anesthesia with air (1.0 l/min) and 1.0% isoflurane. Hair around the tumors was cut with scissors to improve the NIR light transmission, and the three orthogonal diameters were measured by caliper to estimate tumor volume. The rats were placed on their sides in an animal bed and stabilized using tape to reduce potential motion artifacts

caused by breathing movements. The body temperature was maintained at about 37 °C by a warm water blanket connected a water pump (K-MOD 100, Baxter Healthcare Co., Deerfield, IL). A fiber optic pulse oximeter (Nonin Medical, Inc., Plymouth, MN) was placed on the hind foot to monitor arterial hemoglobin saturation ( $s_aO_2$ ) and heart rate (HR), and a thermocouple (Cole-Parmer Instrument Co., Vernon Hills, IL) was inserted rectally to monitor core temperature (Figure 1).

Following baseline  $\Delta[HbO_2]$  measurement (5 ~ 10 min), while the rats were breathing air, the rats were given an overdose of KCl (1 g/kg in saline) i.v. in the tail. Without disturbing the position of the light source, detector or tumor, changes in tumor vascular  $[HbO_2]$  and total hemoglobin concentration ( $[Hb]_{total}$ ) were continuously monitored during and after cardiac arrest for about 40 minutes by NIRS.

## 2.4 Data Analysis

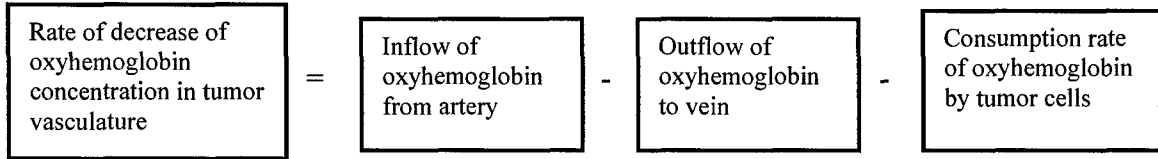
Raw data were filtered, baseline corrected and fitted to the mathematical model (described below) to determine the kinetic parameters of the dynamic response. Tumor oxygen consumption rate  $\dot{V}O_2$  and mean tumor oxygen consumption rate  $\bar{V}O_2$  were computed for 5 rat tumors, respectively, by fitting the mathematical model with the measured  $\Delta[HbO_2]$ . Relationships between those parameters and tumor volume were analyzed using linear regression.

## 3. Development of a Mathematical Model for Tumor Oxygen Consumption Rate

### 3.1 Dynamic Changes of Tumor $[HbO_2]$ caused by KCl Injection

We previously [29] applied Kety's approach [40] to evaluate tumor hemodynamics by using  $HbO_2$  intervention as a tracer, but we did not consider the effect of tumor oxygen consumption. In this study, we included tumor oxygen consumption rate in our hemodynamic

model. In principle, the rate of change of  $\text{HbO}_2$  in tumor vasculature should be equal to the rate at which the  $\text{HbO}_2$  is transported in by arterial circulation minus the rate at which it is carried away into the venous drainage and minus the rate at which tumor cells consume oxygen. In common with our previous approach [29], we assumed a one-compartment model: tumor vasculature is well mixed with respect to oxygen so that a mass balance equation for  $\text{HbO}_2$  can be written by the following chart. Specifically, if  $[\text{HbO}_2]$  is the oxyhemoglobin concentration in the tumor at a given time  $t$ , the general conservation of mass equation for  $[\text{HbO}_2]$  can be schematically depicted as:



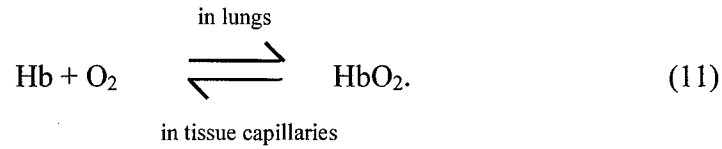
By using Fick's Law of diffusion, the above schematic diagram can be written mathematically as

$$\frac{d[\text{HbO}_2]}{dt} = f \cdot [\text{HbO}_2]_A - f \cdot [\text{HbO}_2]_V - \kappa \cdot [\text{HbO}_2], \quad (10)$$

where  $[\text{HbO}_2] = [\text{HbO}_2](t)$  (arbitrary unit) is a solution to this differential equation and is a function only of time. Because of the one-compartment model,  $f$  is the blood perfusion rate ( $\text{ml}/\text{min}/\text{cm}^3_{\text{tissue}}$ ), and  $[\text{HbO}_2]_A$  and  $[\text{HbO}_2]_V$  are oxyhemoglobin concentrations in the arterial and venous blood in the tumor, respectively, and  $\kappa$  is defined as the oxyhemoglobin dissociation constant ( $\text{min}^{-1}$ ).

In Equation (10), we assumed that the oxyhemoglobin dissociation rate is equal to the tumor oxygen consumption rate at the steady state. This assumption is based on the following: deoxyhemoglobin and oxygen molecules normally combine to form oxyhemoglobin through a loading reaction that occurs in the lungs. Oxyhemoglobin, in turn, can be dissociated to

deoxyhemoglobin and free oxygen molecules through an unloading process that occurs in the tissue capillaries. These two processes can be expressed as the reversible reaction:



The direction of the reaction depends largely on two factors: 1) the  $p\text{O}_2$  of the environment and 2) the affinity of hemoglobin for oxygen. A high  $p\text{O}_2$  drives the equation to the right promoting oxygen loading, whereas low  $p\text{O}_2$  in the tissue capillaries drives the reaction to the left to promote oxygen unloading. The affinity of hemoglobin for oxygen does not change appreciably over a short period of time (minutes). Since the rat died rapidly by KCl induced cardiac arrest, the reaction went to the left to unload oxygen to the plasma because of lack of oxygen supply from incoming blood. The oxygen dissolved in the plasma and diffused to the surrounding tumor tissues, where it was consumed by aerobic cellular respiration.

Assuming that the rat died instantaneously by KCl induced cardiac arrest, then the blood flow stopped, the lungs no longer functioned, and the gas exchange between the alveolar air and the blood in pulmonary capillaries ceased. As a result, no further oxyhemoglobin molecules were transported either to or from the tumor vasculature. Mathematically, this means that the tumor blood perfusion rate  $f$  is 0 after KCl administration. Equation (10), therefore, simplifies to

$$\frac{d[\text{HbO}_2]}{dt} = -\kappa \cdot [\text{HbO}_2], \quad (12)$$

To solve Equation (12), we need to know its initial condition, which is given by

$$[\text{HbO}_2]_{t=0} = [\text{HbO}_2]_0, \quad (13)$$

where  $[\text{HbO}_2]_0$  is the initial baseline value (pre-KCl administration) of oxyhemoglobin concentration. Rearranging and integrating Equation (12) gives rise to an exponential solution

$$\int \frac{d[\text{HbO}_2]}{[\text{HbO}_2]} = -\int \kappa dt \quad \Rightarrow \quad [\text{HbO}_2](t) = C \cdot e^{-\kappa t}, \quad (14)$$

where  $C$  is the constant of integration. By applying the initial condition, equation (13), to equation (14), we obtain the solution as follows:

$$[\text{HbO}_2](t) = [\text{HbO}_2]_0 \cdot e^{-\kappa t}. \quad (15)$$

Equation (15) indicates that following KCl induced cardiac arrest, tumor vascular  $[\text{HbO}_2]$  decreases exponentially with time, and this process is characterized by the dissociation constant  $\kappa$  and the initial oxyhemoglobin concentration  $[\text{HbO}_2]_0$ , both of which can be determined by fitting equation (15) to the experimental data.

Furthermore, it is useful to introduce the mean lifetime  $\tau$ , defined as the average time that an oxyhemoglobin molecule is likely to survive before it is dissociated from oxygen. The number of oxyhemoglobin molecules that survive to time  $t$  is  $[\text{HbO}_2](t)$ , and the number of oxyhemoglobin molecules that dissociate between  $t$  and  $t + dt$  is  $|d[\text{HbO}_2]/dt| \cdot dt$ . Thus, the theoretical mean lifetime  $\tau$  is

$$\tau = \frac{\int_0^{\infty} t \cdot |d[\text{HbO}_2]/dt| \cdot dt}{\int_0^{\infty} |d[\text{HbO}_2]/dt| \cdot dt}, \quad (16)$$

where  $\int_0^{\infty} |d[\text{HbO}_2]/dt| \cdot dt$  gives the total number of oxyhemoglobin molecules that are dissociated after KCl administration, and  $\int_0^{\infty} d[\text{HbO}_2]/dt \cdot dt$  is equal to  $[\text{HbO}_2]_0$ . Evaluating

Equation (16) gives

$$\tau = \frac{\int_0^{\infty} t \cdot [\text{HbO}_2]_0 \cdot (-\kappa) \cdot e^{-\kappa t} \cdot dt}{\int_0^{\infty} [\text{HbO}_2]_0 \cdot (-\kappa) \cdot e^{-\kappa t} \cdot dt} = \frac{\frac{1}{\kappa} \int_0^{\infty} (\kappa t) \cdot e^{-\kappa t} \cdot d(\kappa t)}{\int_0^{\infty} e^{-\kappa t} \cdot d(\kappa t)} = \frac{1}{\kappa}. \quad (17)$$

Equation (17) indicates that the mean lifetime  $\tau$  is simply the inverse of the dissociation constant  $\kappa$  and is just the time constant of Equation (15), which, therefore, can be rewritten as

$$[\text{HbO}_2](t) = [\text{HbO}_2]_0 \cdot e^{-t/\tau}. \quad (18)$$

Since we only measure relative changes of  $[\text{HbO}_2]$ , we can express  $\Delta[\text{HbO}_2]$  as:

$$\Delta[\text{HbO}_2] = [\text{HbO}_2] - [\text{HbO}_2]_0 = -[\text{HbO}_2]_0 (1 - e^{-t/\tau}). \quad (19)$$

In this way, both quantities of  $[\text{HbO}_2]_0$  and  $\tau$  can be obtained by fitting equation (19) with the experimental data taken from the changes in  $[\text{HbO}_2]$  caused by KCl-induced cardiac arrest. As seen from this equation, when the measuring time is long, i.e.,  $t \rightarrow \infty$ , the stabilized  $\Delta[\text{HbO}_2]$  reaches the value of  $\Delta[\text{HbO}_2]_0$ .

### 3.2 Tumor Oxygen Consumption Rate $\dot{V}\text{O}_2$

It is perhaps more important and significant to compute tumor oxygen consumption rate  $\dot{V}\text{O}_2$  from  $\Delta[\text{HbO}_2]$ , because it reflects tumor oxygen consumption and metabolic activities.

Tumor oxygen consumption rate  $\dot{V}O_2$  is determined by taking the first order derivative of equation (15) with respect to time  $t$ ,

$$|\dot{V}O_2(t)| = \left| \frac{d}{dt} [HbO_2]_0 \cdot e^{-t/\tau} \right| = \left| -\frac{[HbO_2]_0}{\tau} \cdot e^{-t/\tau} \right| = \left| -\frac{[HbO_2](t)}{\tau} \right|, \quad (20)$$

which reflects the number of oxyhemoglobin molecules that are dissociated per unit time at a particular time  $t$ . The “minus” sign reflects the opposite direction between a decrease in  $[HbO_2](t)$  and an increase in  $\dot{V}O_2(t)$ . This equation shows that the tumor oxygen consumption is proportional to the concentration of  $[HbO_2]$  in our experimental case with an opposite direction. In particular, equation (20) permits direct quantification of the regular tumor oxygen consumption rate,  $\dot{V}O_2(t=0)$ , as being  $[HbO_2]_0/\tau$ , which can be obtained by fitting equation (19) to our experimental data. Furthermore, taking logarithm of equation (20) leads to

$$\ln |\dot{V}O_2| = -t/\tau + \ln |\dot{V}O_2(t=0)|, \quad (21)$$

where  $\dot{V}O_2$  has been taken as an absolute value to obtain logarithmic expressions. This equation demonstrates a linear relationship between the logarithm of magnitude of tumor oxygen consumption rate and time after KCl injection with a slope being the inverse of the time constant of  $\Delta[HbO_2]$  decay following cardiac arrest.

To facilitate the comparison of the tumor oxygen consumption rates as a function of tumor volume, we also computed an absolute value of mean tumor oxygen consumption rate as follows:

$$|\bar{V}O_2| = \frac{1}{T} \int_0^T \frac{[HbO_2]_0}{\tau} \cdot e^{-t/\tau} dt \quad (22)$$

where  $T$  is the time that it takes for oxyhemoglobin concentration to drop to a steady or asymptotic minimum value. In order to evaluate the integral, we made an approximation:  $T = 3\tau$

because tumor oxyhemoglobin concentration dropped to 5% of its initial value within  $3\tau$ , and the error introduced by this approximation was minimal. Evaluating equation (22) with  $T = 3\tau$  gives

$$\left| \bar{v}O_2 \right| = \frac{1}{3\tau} \int_0^{3\tau} \frac{[HbO_2]_0}{\tau} \cdot e^{-t/\tau} dt \approx \frac{1}{3} \left( \frac{[HbO_2]_0}{\tau} \right). \quad (23)$$

Both eqs. (20) and (23) indicate that the quantity  $([HbO_2]_0/\tau)$  has an important physiological significance, representing the transient and mean tumor oxygen consumption rate and reflecting the metabolic activity of the tumor.

#### 4. Experimental Results

Figure 2(a) shows the KCl effects on tumor vascular  $\Delta[HbO_2]$  and  $\Delta[Hb]_{\text{total}}$  for a representative mammary adenocarcinoma 13762NF ( $12.7 \text{ cm}^3$ ). The exponential appearance of the curve matches the solution to the mathematical model, equation (19), and  $\Delta[HbO_2]$  dropped sharply and significantly by  $0.8723 \pm 0.0002$  ( $p < 0.0001$ ). In contrast, total hemoglobin concentration,  $[Hb]_{\text{total}}$ , decreased by  $0.0870 \pm 0.0001$ , only 10% of the change in  $[HbO_2]$ . This indicates that total tumor blood volume remained relatively constant, as compared to  $[HbO_2]$  during the course of the experiment. This also shows that the assumption of blood flow  $f = 0$  after KCl injection was reasonable. By fitting equation (19) to the data,  $[HbO_2]_0$  and  $\tau$  were found to be  $0.880 \pm 0.005$  and  $0.691 \pm 0.004$  (min), respectively. Figure 2(b) shows the time course profiles of tumor vascular  $\Delta[HbO_2]$  and  $\Delta[Hb]_{\text{total}}$  for a second tumor ( $15.7 \text{ cm}^3$ ). In this case,  $\Delta[HbO_2]$  dropped by  $1.444 \pm 0.005$  ( $p < 0.0001$ ), while  $\Delta[Hb]_{\text{total}}$  dropped  $0.488 \pm 0.002$ . As for the first breast tumor, the magnitude of the drop in  $\Delta[Hb]_{\text{total}}$  was much less than that in  $\Delta[HbO_2]$ . The values of  $[HbO_2]_0$  and  $\tau$  were determined as  $1.192 \pm 0.008$  and  $1.36 \pm 0.02$  (min), respectively, based on equation (19). For the five tumors, a strong linear relationship was found

between tumor  $[\text{HbO}_2]_0$  and tumor volume (Figure 3) and between the mean lifetime ( $\tau$ ) and tumor volume (Figure 4).

Figure 5 shows the relationships between the tumor oxygen consumption rates  $\dot{V}\text{O}_2$  as a function of time and tumor volume. To better separate the curves, the data only for the first four minutes after KCl injection were plotted. Each curve was obtained by substituting corresponding  $[\text{HbO}_2]_0$  and  $\tau$  values to equation (20). The same relationships were replotted in Figure 6 on a semilog graph, giving straight lines of slope  $1/\tau$ , according to equation (21). From these two figures, it appeared that smaller tumors had greater oxygen consumption rates before and right after KCl injection. It is more significant and important to be able to estimate the tumor oxygen consumption rate when the rats were alive. Considering that the rats were alive at  $t = 0$ ,  $\dot{V}\text{O}_2(\text{alive})$  was determined by setting  $t = 0$  in equation (20). Thus,  $\dot{V}\text{O}_2(\text{alive}) = \dot{V}\text{O}_2(t = 0) = [\text{HbO}_2]_0/\tau$ . Figure 7 shows a strong ( $R = 0.86$ ) inverse linear relationship between  $\dot{V}\text{O}_2(0)$  and tumor volume, indicating clearly that the larger the tumor, the smaller its oxygen consumption rate. Furthermore, Figure 8 shows the relationship between the mean tumor oxygen consumption rate  $\bar{\dot{V}}\text{O}_2$  and tumor volume after KCl injection. Again, a significant correlation was found ( $R = 0.86$ ), suggesting that, on average, the tumor oxygen consumption rate decreases with an increase in tumor volume.

## 5. Discussion and Conclusion

We developed a mathematical model for computing oxygen consumption rate in tumors and used NIRS to investigate the oxygen dynamics during KCl induced cardiac arrest. Although the procedure was invasive, we did not add additional invasiveness for the animal experiment

since the NIR readings in the study were taken during the final animal euthanasia. In this way, we could obtain extra and useful physiological parameters, leading to quantification of tumor oxygen consumption rate. Of course, this methodology has no relevance to be used in human studies, but the knowledge learned here can be useful in understanding solid tumor physiology and highly relevant for future improvement of tumor treatment.

The NIR signal has been found to be very sensitive to changes in tissue oxygenation in small blood vessels such as arterioles, capillary, and venules [41,42,43,44]. These are the places where the oxygen is consumed by tumor/tissue cells. In this study, Fick's Law was applied to extract and quantify the tumor oxygen consumption from the tumor oxygenation dynamics, since the rats died rapidly so that the tumor metabolism or oxygen consumption was not coupled to the tumor blood flow. The overall shapes of the  $\Delta[\text{HbO}_2]$  curves, as seen in Figures 2(a) and 2(b), were similar to those obtained by Steen *et al.*, who used subcutaneously implanted rat 9L gliosarcoma and pentobarbital overdose [27]. Time constant analysis showed that the time constant of oxygenation,  $\tau$ , determined here was of the same order as reported by Steen *et al.*, and that  $\tau$  was related to tumor oxygen consumption. Moreover, the observation that the magnitude of the drop in  $\Delta[\text{Hb}]_{\text{total}}$  was much less than that in  $\Delta[\text{HbO}_2]$  may indicate that the decrease in rat tumor  $\Delta[\text{HbO}_2]$  was mainly caused by tumor oxygen consumption rather than decrease in total tumor blood volume.

We noted that tumor  $[\text{HbO}_2]_0$  and tumor volume have a strong, positive linear relationship, as given in Figure 3. This correlation makes sense, intuitively, because it simply manifests the fact that the larger the tumor, the more oxygenated hemoglobin is included in the tumor volume. The positive linear relationship between the mean lifetime ( $\tau$ ) and tumor volume (Figure 4) indicates that, on average, the time that an oxyhemoglobin molecule is likely to

survive before it is dissociated to yield a deoxyhemoglobin molecule and four free oxygen molecules increases with increasing tumor volume. The close correlation between  $\tau$  and tumor volume suggests that tumor blood perfusion is becoming increasingly poor as the tumor increases in size, leading to increased tumor hypoxia with increasing tumor volume.

As shown in equation (20), tumor oxygen consumption rate  $\dot{V}O_2$  is an exponential function of  $t$  and is dependent on both the initial tumor oxy-hemoglobin concentration  $[HbO_2]_0$  and the time constant  $\tau$ . This means that tumor oxygen consumption rate  $\dot{V}O_2$  decreases exponentially with time after KCl administration. This phenomenon may be explained as follows: as oxygen is being depleted by tumor cellular metabolism, oxygen concentration or oxygen tension ( $pO_2$ ) gradient across tumor capillaries and tissues decreases. Since oxygen diffusion is linearly proportional to its concentration gradient according to Fick's Law of diffusion, a lower oxygen concentration gradient or a lower oxygen tension gradient results in decreased oxygen diffusion and, thus, less oxygen is available for tumor cellular aerobic respiration. This, in turn, results in less oxygen consumption. This is consistent with several studies, which have reported that oxygen consumption is proportional to the concentration of available oxyhemoglobin [25,45,46,47,48]. Also, a negative linear relationship between the mean tumor oxygen consumption rate  $\bar{V}O_2$  and tumor volume (Figure 8) has been observed, consistent with previous reports [49,50] that larger tumors have lower oxygen consumption. This might be attributed to larger necrotic fraction.

As mentioned in Section 1, there are numerous development and methodologies to quantify tissue oxygen consumption or consumption rate for skeletal muscles [14-18] and for neuronal activities in the brain [19-22], using either experimental or theoretical approaches. But those approaches need to be modified accordingly in order to be suitable for determination of

tumor oxygen consumption rate. The newly developed models for tissue oxygen consumption are relatively complex [23-25], without quantitative association between the tumor consumption rate and the measured NIR hemodynamic parameters. Our study reported in paper fulfills the need to develop a simplified mathematical model for extracting the tumor oxygen consumption rate from the NIR measurement. While our model is promising, it needs to be validated in our future study. One of the existing “gold standard” methods to validate tissue oxygen consumption is to employ a standard Clark oxygen electrode to measure partial oxygen pressure [51]. This method is invasive, so it is difficult to be utilized in human studies, but relatively easier in animal tumor studies [10,28]. The advantage of using the Clark oxygen electrode is mainly to provide absolute values of tissue oxygen consumption readings, while it detects only local area, perturbs local tissue vasculature, and creates difficulty for repeatable measurements. If our methodology is validated in the future by the Clark oxygen electrode, some of the disadvantages of oxygen electrodes can be overcome by the NIR approach. Moreover, since our current method uses relative  $\Delta[\text{HbO}_2]$  without the specific values of tumor DPF, the calculated tumor oxygen consumption rate in this paper can be treated more appropriately as a tumor oxygen consumption index. The methodology has the potential to provide absolute quantification of tumor  $\dot{V}\text{O}_2$  through NIR hemodynamic measurements once we develop a way to obtain tumor DPF.

While the present study demonstrates the possibility of evaluating oxygen consumption rates of tumors by NIRS following KCl administration, the animals have to be sacrificed to perform the measurements. However, similar assessment is also possible through local tissue clamping as performed by Steinberg et al for renal cell carcinoma in patients prior to resection [52]. It should be possible to estimate tumor oxygen consumption rate without sacrificing rats, if we could quantify the blood in-flow and out-flow of the tumors. This might be achieved by

introducing a respiratory challenge, such as altering inhaled gas from air to carbogen or oxygen. Indeed, the time course of  $\Delta[\text{HbO}_2]$  with respect to KCl arrest is not unlike that observed in switching from hyperoxic gas breathing to air as we have reported previously for rat breast and prostate tumors [12,13,29] or observed using blood oxygen level dependant (BOLD) contrast proton MRI [53,54]. It is also similar to the measurements of tissue  $\text{pO}_2$  observed in a perfused rat heart in response to induction of total global ischemia [55].

We have used a single channel NIRS in this study, which provides us with global and mean values of tumor oxygen consumption rate. Using a multi-channel NIRS will allow intratumoral heterogeneity to be investigated, and we are currently developing such a capability [56]. Indeed, others have reported spatially resolved NIRS for clinical applications to breast tumors [6,57]. Once NIR imaging approach is taken by employing multiple sources and detectors for the measurement, imaging reconstruction algorithms allow us to resolve and detect the tumors that are not superficial [6,8,58,59,60,61].

In summary, the tumor oxygen consumption rate was calculated by fitting the newly developed model to the measured  $\Delta[\text{HbO}_2]$  data. A strong negative linear relationship was found between the mean tumor oxygen consumption rate and tumor volume, indicating that larger tumors have smaller mean oxygen consumption rate. This study further demonstrates the utility of NIRS as an effective, real-time means to investigate tumor oxygen consumption rate, while further development is required to make it to be non-invasive in the future.

**Acknowledgement:**

Supported in part by Department of Defense Breast Cancer Pre-doctoral Research Fellowships BC962357 (YS), Breast Cancer Initiative IDEA award DAMD17-00-1-0459 (HL), and Cancer Imaging Program NIH P20 CA086354 (RPM). We thank Dr. Anca Constantinescu for technical assistance.

## Figure Captions

**Figure 1.** Schematic setup of one channel, near infrared, frequency domain IQ instrument for tumor investigation *in vivo*. Two fiber bundles were used to deliver and detect the laser light, at 758 and 785 nm, which were transmitted through the implanted tumor. The overdose of KCl was administered by tail vein injection after 5~10 min of  $\Delta[\text{HbO}_2]$  baseline measurement.

**Figure 2.** Effects of overdose KCl injection on tumor vascular  $\Delta[\text{HbO}_2]$  and  $\Delta[\text{Hb}]_{\text{total}}$  for two breast tumors: (a)  $12.7 \text{ cm}^3$  and (b)  $15.7 \text{ cm}^3$ .  $\Delta[\text{HbO}_2]$  dropped rapidly and significantly ( $p < 0.0001$ ). Both  $\Delta[\text{HbO}_2]$  and  $\Delta[\text{Hb}]_{\text{total}}$  are in arbitrary unit. The error bars indicate measurement uncertainties and are labeled at selected locations. (Some of them are too small to be seen.)

**Figure 3.** Relationship between tumor  $[\text{HbO}_2]_0$  and tumor volume for five mammary adenocarcinomas 13762NF.

**Figure 4.** Relationship between time constant  $\tau$  and tumor volume for five mammary adenocarcinomas 13762NF.

**Figure 5.** Relationships between the tumor oxygen consumption rates,  $|\bar{V}\text{O}_2|$ , as a function of time and tumor volume.

**Figure 6.** Relationship between tumor oxygen consumption rates,  $|\bar{V}\text{O}_2|$ , as a function of time and tumor volume plotted on a semilog scale.

**Figure 7.** Relationship between tumor oxygen consumption rate at  $t=0$ ,  $|\dot{V}O_2(0)|$  and tumor volume.

**Figure 8.** Relationship between the mean tumor oxygen consumption rate  $|\bar{V}O_2|$  and tumor volume after KCl injection.

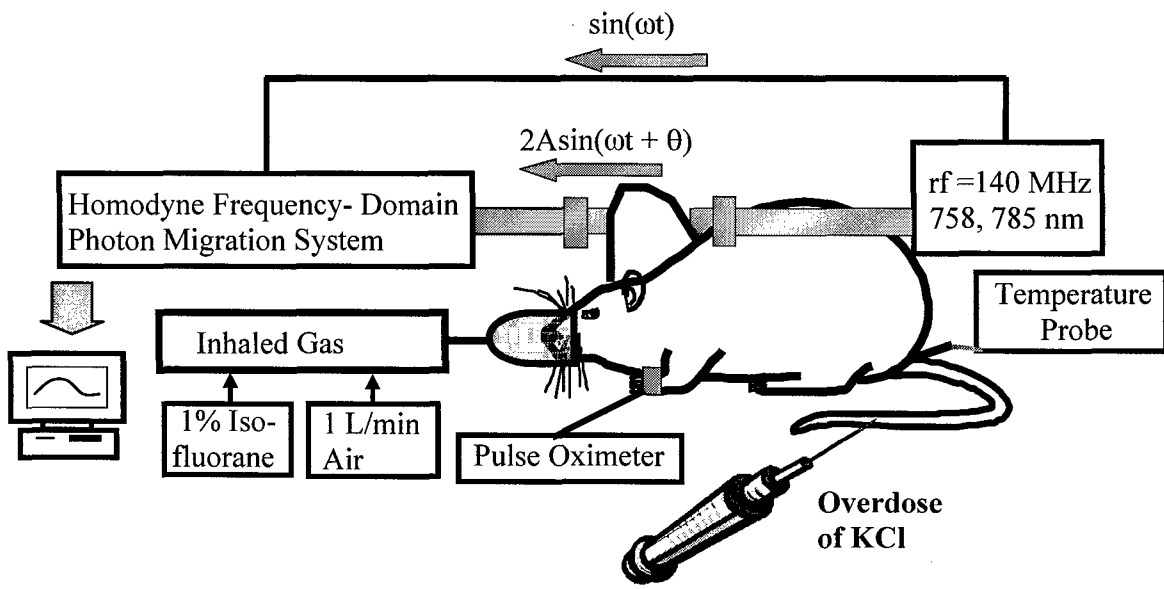


**Figure 1**

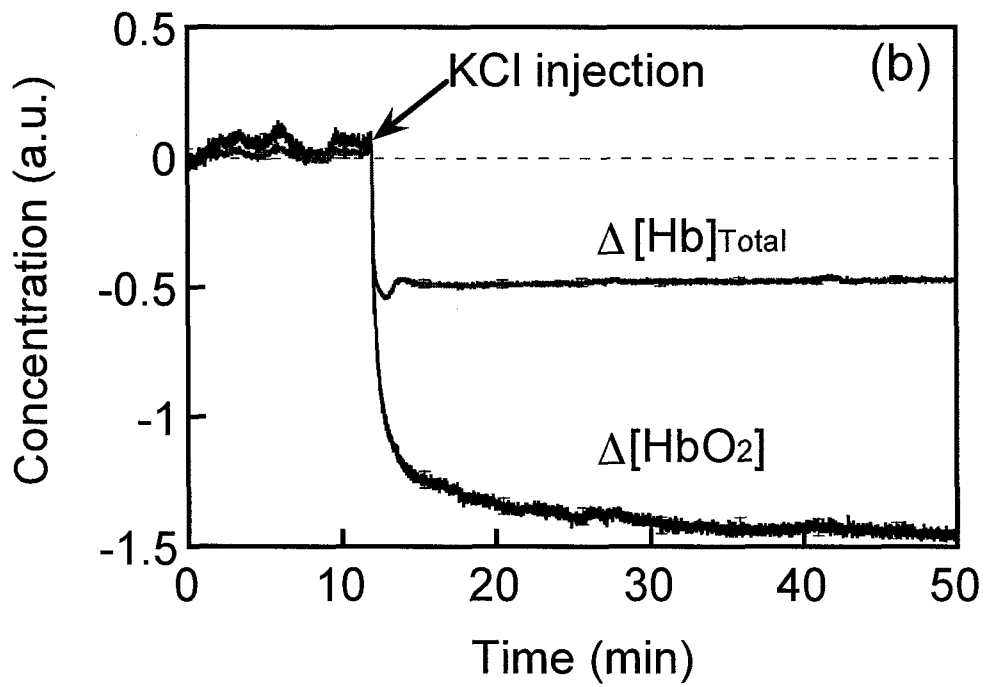
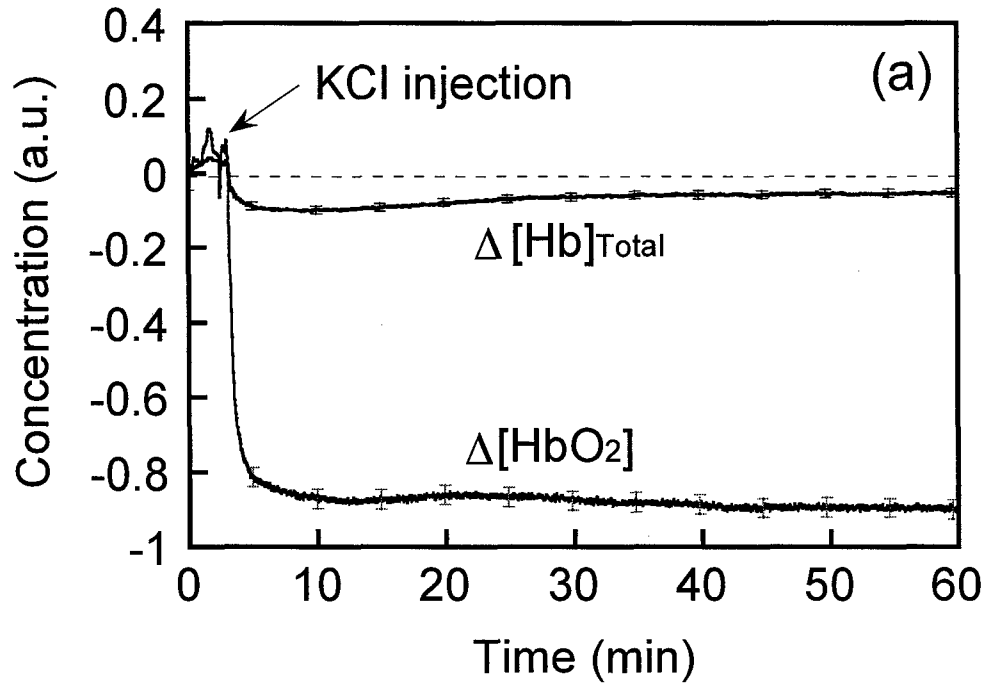


Figure 2

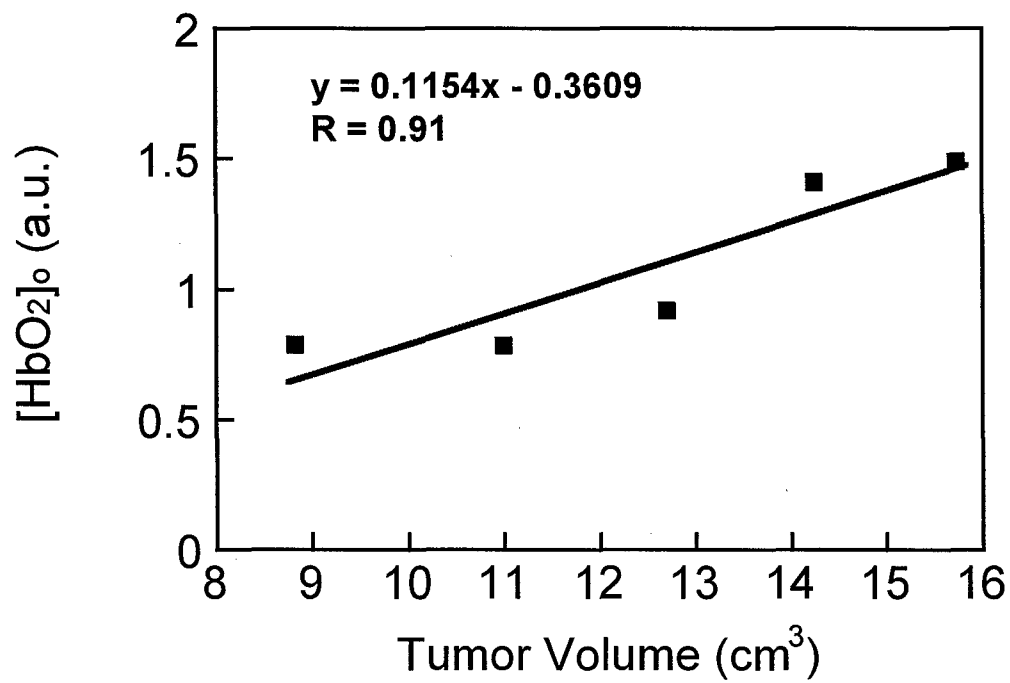


Figure 3

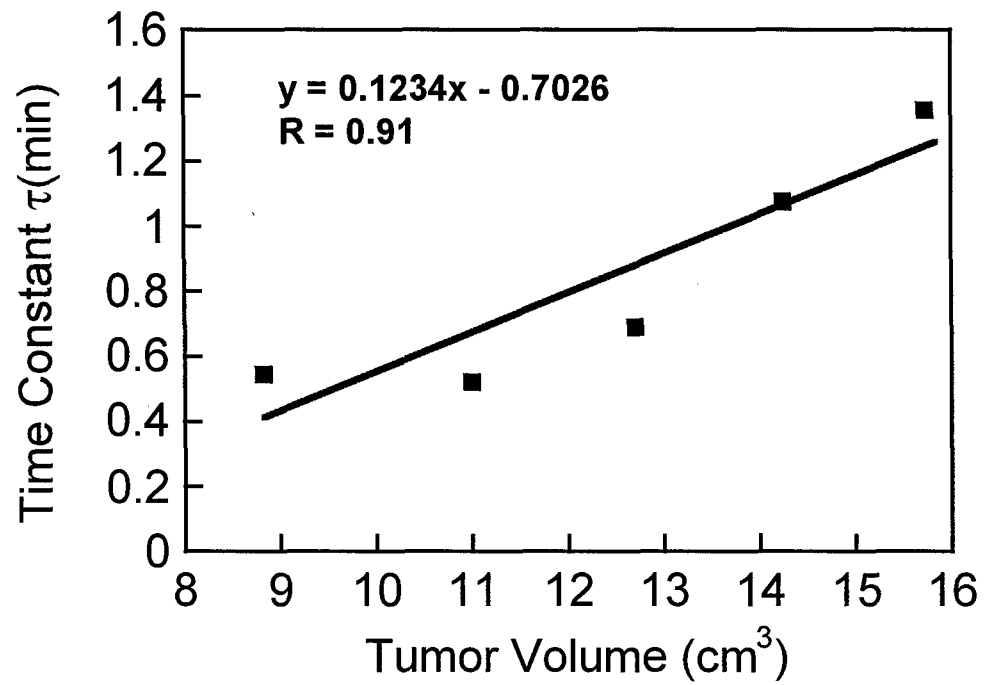


Figure 4

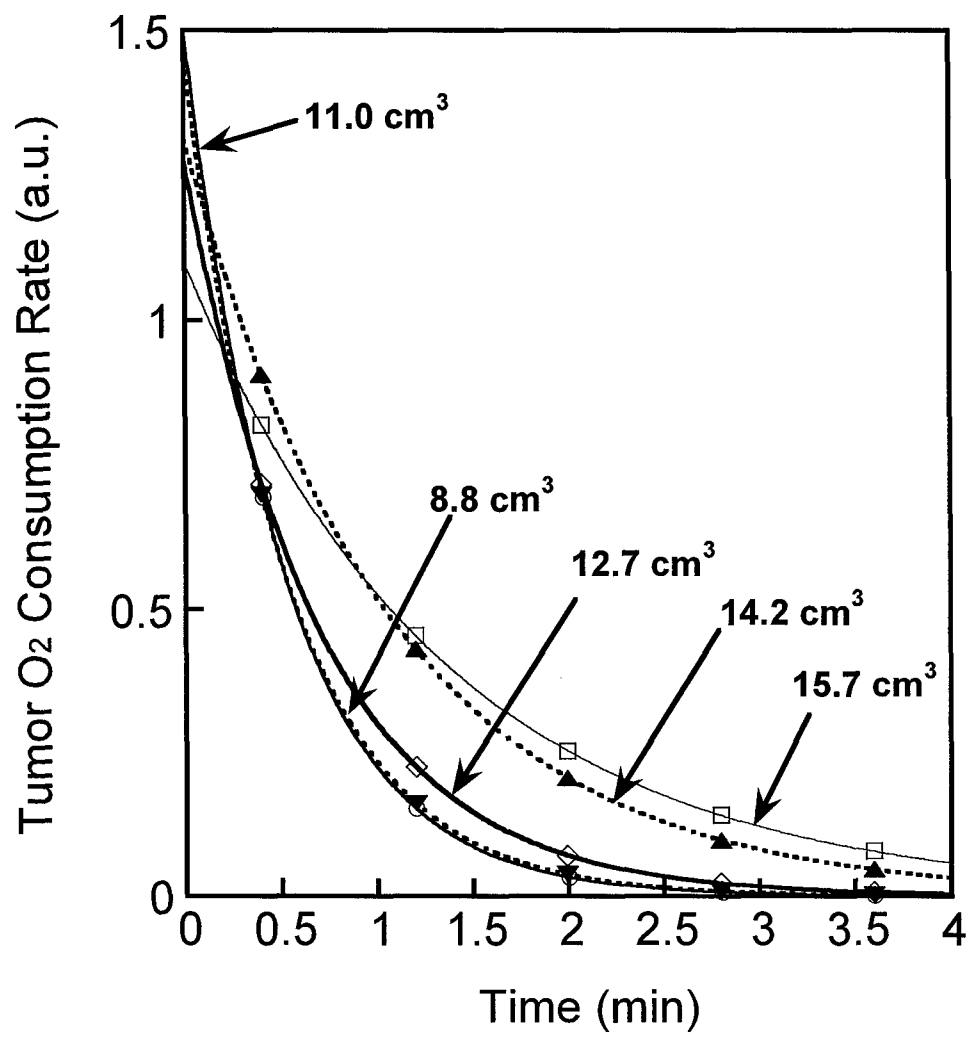


Figure 5

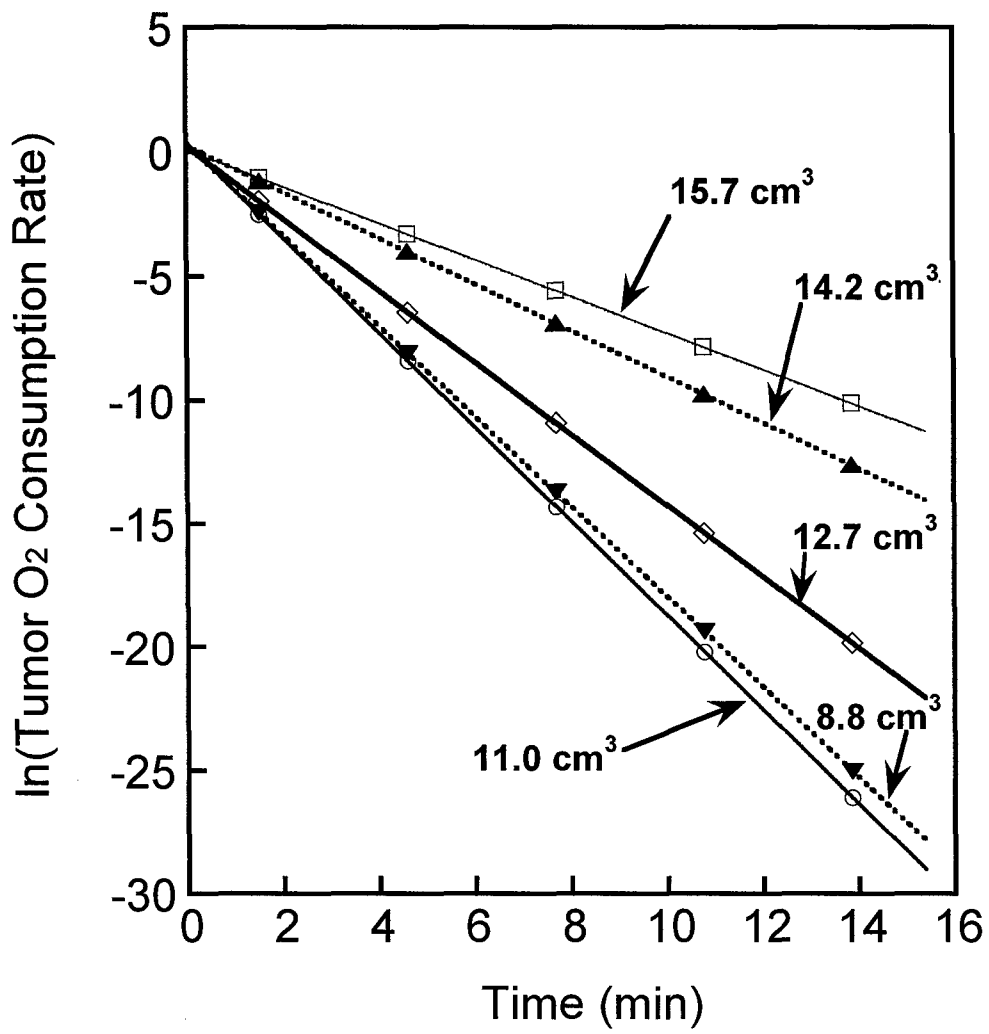


Figure 6

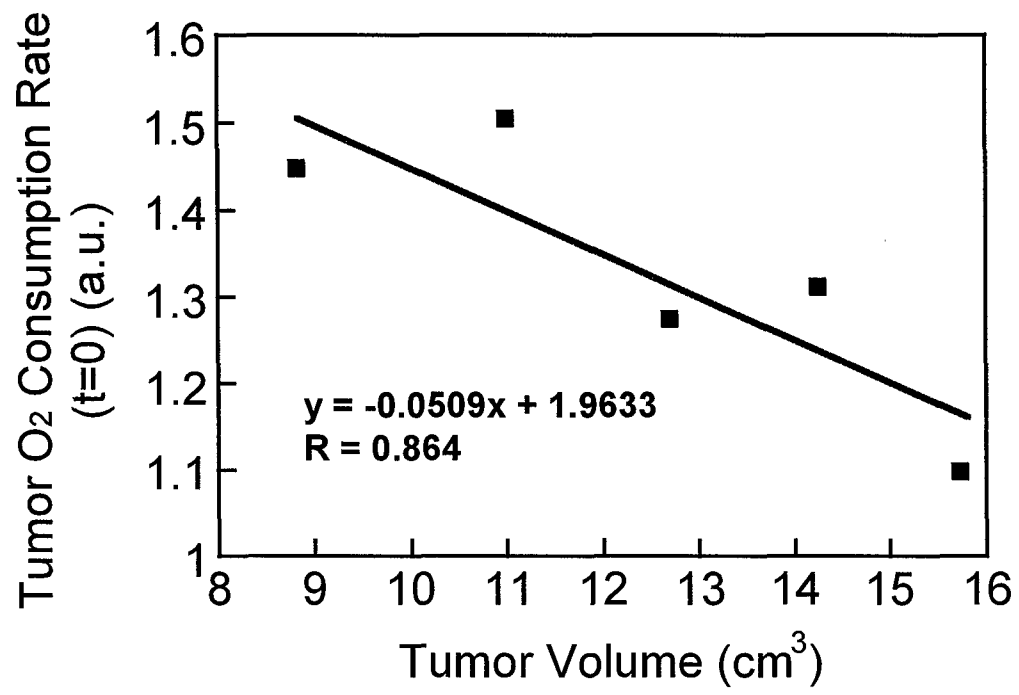


Figure 7

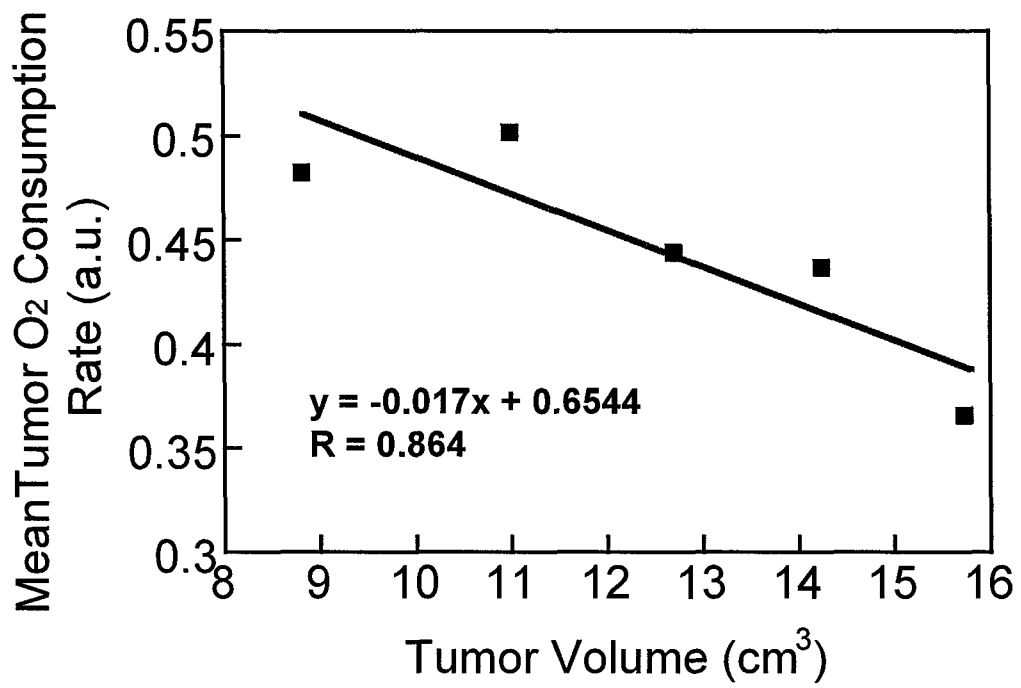


Figure 8

## References:

1. Brown, J. M. and Giaccia, A. J., (1998) "The unique physiology of solid tumors: opportunities (and problems) for cancer therapy," *Cancer Res.*, **58**: 1408-1416.
2. Höckel, M., Schlenger, K., Aral, B., Mitze, M., Schäffer, U., and Vaupel, P., (1996) "Association between tumor hypoxia and malignant progression in advanced cancer of the uterine cervix," *Cancer Res.* **56**, 4509-4515.
3. Höckel M. and Vaupel, P., (2001) "Tumor Hypoxia: Definitions and current clinical, biologic, and molecular aspects," *J Natl Cancer Inst.* **93**, 266-276.
4. Tromberg, B., Shah, N., Lanning, R., Cerussi, A., Espinoza, J., Pham, T., Svaasand, L., and Butler, J. (2000) "Non-invasive in vivo characterization of breast tumors using photon migration spectroscopy," *Neoplasia.* **2**, 26-40.
5. Fantini, S., Walker, S. A., Franceschini, M. A., Kaschke, M., Schlag, P. M., and Moesta, K. T., (1998) "Assessment of the size, position, and optical properties of breast tumors in vivo by noninvasive optical methods," *Appl. Opt.* **37**, 1982-1989.
6. McBride, T. O., Pogue, B. W., Jiang, S., Österberg, U. L., and Paulsen, K. D., (2001) "Initial studies of in vivo absorbing and scattering heterogeneity in near-infrared tomographic breast imaging," *Optics Letters.* **26**, 822-824.
7. Hull, E. L., Conover, D. L., and Foster, T., (1999) "Carbogen-induced changes in rat mammary tumour oxygenation reported by near infrared spectroscopy," *Br. J. Cancer.* **79**, 1709-1716.
8. Cheng, X. F., Mao, J. M., Bush, R., Kopans, D. B., Moore, R. H., Chorlton, M., (2003), "Breast cancer detection by mapping hemoglobin concentration and oxygen saturation," *Appl. Opt.* **42(31)**, 6412-6421.
9. Cheung, C., Culver, J. P., Takahashi, K., Greenberg, J. H., and Yodh, A. G., (2001) "In vivo cerebrovascular measurement combining diffuse near-infrared absorption and correlation spectroscopies," *Phys. Med. Biol.* **46**, 2053-2065.
10. Menon, C, Polin, G. M, Prabakaran, I, His, A, Cheung, C, Culver, J. P, Pingpank, J. F., Sehgal, C. S., Yodh, A. G., Buerk, D. G, Fraker, D. L., (2003) "An integrated approach to measuring tumor oxygen status using human melanoma xenografts as a model," *Cancer Res.* **63 (21)**, 7232-7240.
11. Pogue, B. W., Paulsen, K. D., O'Hara, J. A., Wilmot, C. M., and Swartz, H. M., (2001) "Estimation of oxygen distribution in RIF-1 tumors by diffusion model-based interpretation of pimonidazole hypoxia and Eppendorf measurements," *Radiat. Res.* **155**, 15-25.

- 
12. Kim, J. G., Song, Y., Zhao, D., Constantinescu, A., Mason, R. P., and Liu, H., (2003) "Interplay of Tumor Vascular Oxygenation and pO<sub>2</sub> in Tumors Using NIRS, 19F MR pO<sub>2</sub> Mapping, and pO<sub>2</sub> Needle Electrode," *J. Biomed. Opt.* **8(1)**, 53-62.
  13. Gu, Y., Bourke, V., Kim, J. G., Constantinescu, A., Mason, R. P., and Liu, H., (2003) "Dynamic Response of Breast Tumor Oxygenation to Hyperoxic Respiratory Challenge Monitored with Three Oxygen-Sensitive Parameters," *Appl. Opt.* **42(16)**, 2960-2967.
  14. De Blasi, R. A., Cope, M., Elwell, C., Safoue, F., and Ferrari, M., (1993) "Noninvasive measurement of human forearm oxygen consumption by near-infrared spectroscopy", *Eur. J. Appl. Physiol.*, **67**:20-25.
  15. De Blasi, R. A., Ferrari, M., Natali, A., Conti, G., Mega, A., and Gasparetto, A., (1994) "Noninvasive measurement of forearm blood flow and oxygen consumption by near-infrared spectroscopy", *J. Appl. Physiol.*, **76(3)**, 1388-1392.
  16. Homma, S., Eda, H., Ogasawara, S., and Kagaya, A., (1996) "Near-infrared estimation of O<sub>2</sub> supply and consumption ", *J. Appl. Physiol.*, **80**, 1279-1284.
  17. Binzoni, T., Quaresima, V., Barattelli, G., Hiltbrand, E., Gürke, L., Terrier, F., Cerretelli, R., and Ferrari, M., (1998) "Energy metabolism and interstitial fluid displacement in human gastrocnemius during short ischemic cycles", *J. Appl. Physiol.*, **85**, 1244-1251.
  18. Casavola, C., Paunescu, L.A., Fantini, S., Gratton, E., (2000) "Blood flow and oxygen consumption with near-infrared spectroscopy and venous occlusion: spatial maps and the effect of time and pressure of inflation," *J. Biomed. Opt.* **5(3)**, 269-276.
  19. Ferrari, M., Mottola, L., Quaresima, V., (2004) ""Principles, techniques, and limitations of near infrared spectroscopy," *Can. J. Appl. Physiol.* **29(4)**, 463-487.
  20. Sheth, S. A., Nemoto, M., Guiou, M., Walker, M., Pouratian, N., Toga, A.W., (2004) "Linear and nonlinear relationships between neuronal activity, oxygen metabolism, and hemodynamic responses," *Neurons* **42(2)**, 347-355.
  21. Boas, D. A., Dale, A. M., Franceschini, M. A., (2004) "Diffuse optical imaging of brain activation: approaches to optimizing image sensitivity, resolution, and accuracy," *NeuroImage*, **23**, S275-S288.
  22. Culver, J. P., Durduran, T., Furuya, T., Cheung, C., Greenberg, J. H., Yodh, A. G., (2003) "Diffuse optical tomography of cerebral blood flow, oxygenation, and metabolism in rat during focal ischemia," *J. Cerebr. Blood F. Met.* **23(8)**, 911-924.
  23. Fantini, S., (2002), "A haemodynamic model for the physiological interpretation of in vivo measurements of the concentration and oxygen saturation of haemoglobin," *Phys. Med. Biol.* **47(18)**, N249-N257.

- 
24. Boas, D. A., Strangman, G., Culver, J. P., Hoge, R. D., Jaszewski, G., Poldrack, R. A., Rosen, B. R., Mandeville, J. B., (2003) "Can the cerebral metabolic rate of oxygen be estimated with near-infrared spectroscopy?" *Phys. Med. Biol.* **48**, 2405-2418.
25. Dasu, A., Toma-Dasu, I., and Karlsson, M., (2003) "Theoretical simulation of tumour oxygenation and results from acute and chronic hypoxia," *Phys. Med. Biol.* **48**, 2829-2842.
26. Vaupel, P., (1997) "Vascularization, blood flow, oxygenation, tissue pH, and bioenergetic status of human breast cancer", *In: Nemoto and LaManna (eds), Oxygen Transport to Tissue XVIII*, Plenum Press: New York, 243-253.
27. Steen, R. G., Kitagishi, K., and Morgan, K., (1994) "In vivo measurement of tumor blood oxygenation by near-infrared spectroscopy: immediate effects of pentobarbital overdose or carmustine treatment", *J. Neuro-Oncol.*, **22**, 209-220.
28. Kawauchi, S., Morimoto, Y., Sato, S., Arai, T., Seguchi, K., Asanuma, H., Kikuchi, M., (2004) "Differences between cytotoxicity in photodynamic therapy using a pulsed laser and a continuous wave laser: study of oxygen consumption and photobleaching," *Laser Med. Sci.* **18(4)**, 179-183.
29. Liu, H., Song, Y., Worden K. L., Jiang X., Constantinescu, A., and Mason R. P., (2000) "Noninvasive investigation of blood oxygenation dynamics of tumors by near-infrared spectroscopy," *Appl. Opt.*, **39(28)**, 5231-5243.
30. Benesch, R., Macduff, G., and Benesch, R. E., (1965) "Determination of oxygen equilibria with a versatile new tonometer," *Anal. Biochem.*, **11**, 81-87.
31. Benesch, R. E., Benesch, R., and Yung, S., (1973) "Equations for the spectrophotometric analysis of hemoglobin mixtures," *Anal. Biochem.*, **55**, 245-248.
32. van Assendelft, O. W. and Zijlstra, W. G., (1975) "Extinction coefficients for use in equations for the spectrophotometric analysis of haemoglobin mixtures," *Anal. Biochem.*, **69**, 43-48.
33. Fishkin, J. B., Coquoz, O., Anderson, E. R., Brenner, M., Tromberg, B. J., (1997) "Frequency-domain photon migration measurements of normal and malignant tissue optical properties in a human subject," *Appl. Opt.*, **36(1)**, 10-.
34. "User Manual" for Near-Infrared, Non-Invasive Tissue Oximeter, ISS Inc., 1602 Newton Drive, Champaign IL 61822, USA.
35. Sevick, E. M., Chance, B., Leigh, J., Nioka, S., and Maris, M., (1991) "Quantitation of time- and frequency-resolved optical spectra for the determination of tissue oxygenation," *Anal. Biochem.* **195**, 330-351.

- 
36. Delpy, D. T. and Cope, M., (1997) "Quantification in tissue near infrared spectroscopy," *Philos. Trans. R. Soc. London B* **952**, 649-659.
37. Zijlstra, W. G., Buursma, A., and Meeuwse-van der Roest, W. P., (1991) "Absorption spectra of human fetal and adult oxyhemoglobin, de-oxyhemoglobin, carboxyhemoglobin, and methemoglobin," *Clin. Chem.*, **37**(9), 1633-1638.
38. Yang, Y., Liu, H., Li, X., and Chance, B., (1997) "A low cost frequency-domain photon migration instrument for tissue spectroscopy, oximetry, and imaging," *Opt. Eng.* **36**(5), 1562-1569.
39. Hahn, E. W., Peschke, P., Mason, R. P., Babcock, E. E., and Antich, P. P., (1993) "Isolated tumor growth in a surgically formed skin pedicle in the rat: a new tumor model for NMR studies", *Magn. Reson. Imaging*, **11**, 1007-1017.
40. Kety S. S., (1987) "Cerebral circulation and its measurement by inert diffusible racers," *Israel J. Med. Sci.* **23**, 3-7.
41. Chance, B., Dait, M. T., Zhang, C., Hamaoka, T., and Hagerman, F., (1992) "Recovery from exercise-induced desaturation in the quadriceps muscles of elite competitive rowers", *Am. J. Physiol.*, **262** (*Cell Physiol.* 31), C766-C775.
42. Mancini, D. M., Bolinger, L, Liu, H., Kendrick, K., Chance, B., and Wilson. J. R., (1994) "Validation of near-infrared spectroscopy in humans", *J. Appl. Physiol*, **77**, 2740-2747.
43. Hampson, N. B., and Piantadosi, C. A., (1988) "Near infrared monitoring of human skeletal muscle oxygenation during forearm ischemia", *J. Appl. Physiol*, **64**, 2449-2457.
44. Liu, H., Hielscher, A. H., Tittel, F. K., Jacques, S. L., and Chance, B., (1995) "Influence of blood vessels on the measurement of hemoglobin oxygenation as determined by time-resolved reflectance spectroscopy," *Med. Phys.* **22**, 1209-1217.
45. Vaupel, P.W. "Oxygenation of solid tumors," in *Drug Resistance in Oncology*, Ed by Teicher, BA, Marcel Dekker, New York, 53-85.
46. Gullino P. M., Grantham F. H., and Courtney A.H., (1967) "Utilization of oxygen by transplanted tumors in vivo," *Cancer Res.*, **27**, 1020-1029.
47. Kristensen, C. A., Roberge, S., Jain, R. K., (1997) "Effect of tumor necrosis factor alpha on vascular resistance, nitric oxide production, and glucose and oxygen consumption in perfused tissue-isolated human melanoma xenografts," *Clin. Cancer Res.* **3**(3), 319-324.
48. Dewhirst, M. W., Secomb, T. W., Ong, E. T., Hsu, R., and Gross, J. F., (1994) "Determination of local oxygen consumption rates in tumors," *Cancer Res.* **54**, 3333-6.

- 
49. Jain, R. K., and Ward-Hartley, K., (1984) "Tumor blood flow: characterization, modification and role in hyperthermia", *IEEE Trans. Sonics Ultrasonics*, **SU-31**, 504-526.
50. Song, C. W., (1984) "Effect of local hyperthermia on blood flow and microenvironment", *Cancer Res. (Suppl.)*, **44**, 4721s-4730s.
51. Lang, M. A., Rosenthal, S. J., Caplan, S. R., Essig, A., (1979) "Measurement of oxygen consumption in voltage-clamped epithelia," *Am. J. Physiol.* **236(2)**, F206-9.
52. Steinberg, F., Röhrborn H. J., Otto, T, Scheufler, K. M., Streffer, C., (1997) "NIR reflection measurements of hemoglobin and cytochrome aa3 in healthy tissue and tumors," *Adv. Exp. Med. Biol.*, **428**, 69-77.
53. Jiang, L., Zhao, D., Constantinescu, A., and Mason, R. P., (2004), "Comparison of BOLD contrast and Gd-DTPA dynamic contrast enhanced imaging in rat prostate tumor," *Magn. Reson. Med.*, **51**, 953-60.
54. Robinson, S. P., Howe F. A., and Griffiths J.R., (1995) "Noninvasive monitoring of carbogen-induced changes in tumor blood flow and oxygenation by functional MRI," *Int. J. Radiat. Oncol. Biol. Phys.*, **33**, 855-859.
55. Mason, R. P., Jeffrey, F. M. H., Malloy, C. R., Babcock, E. E., and Antich, P. P., (1992) "A noninvasive assessment of myocardial oxygen tension:  $^{19}\text{F}$  NMR spectroscopy of sequestered perfluorocarbon emulsion," *Magn. Reson. Med.*, **27**, 310-317.
56. Kim, J. G., Gu, Y., Constantinescu, A., Mason, R. P., and Liu, H., (2003) "Non-Uniform Tumor Vascular Oxygen Dynamics Monitored By Three-Channel Near-Infrared Spectroscopy", *Proc. SPIE-Int. Soc. Opt. Eng.* **4955**, 388-396.
57. Chance, B., (2002) "High sensitivity and specificity in human breast cancer detection with near-infrared imaging," *OSA Biomedical Topical Meetings, Technical Digest*, 450-455.
58. Hielscher, A. H., Klose, A. D., and Hanson, K. M., (1999) "Gradient-Based Iterative Reconstruction Scheme for Time-Resolved Optical Tomography," *IEEE Trans. Med. Imag.* **18**, 262-271.
59. Yao, Y. Q., Wang, Y., Pei, Y. L., Zhu, W. W., and Barbour, R. L., (1997) "Frequency-domain optical imaging of absorption and scattering distributions by Born iterative method," *J. Opt. Soc. Amer. A*, **14**, 325-342.
60. Paulsen, K. D. and Jiang, H., (1996). "Enhanced frequency domain optical image reconstruction in tissues through total variation minimization," *Appl. Opt.*, **35**, 3447-3458.
61. Schotland, J. C., (1997) "Continuous-wave diffusion imaging," *J. Opt. Soc. Am.*, **14**, 275-279.

# Investigation of bi-phasic tumor oxygen dynamics induced by hyperoxic gas intervention: *A numerical study*

Jae G. Kim and Hanli Liu\*

Joint Graduate Program in Biomedical Engineering,  
University of Texas Southwestern Medical Center at Dallas/ University of Texas at Arlington  
Arlington, TX 76019  
[hanli@uta.edu](mailto:hanli@uta.edu)

**Abstract:** This study intends to explore the underlying principle of the bi-phasic behavior of increases in oxygenated hemoglobin concentration that was observed *in vivo* from rat breast tumors during carbogen/oxygen inhalation. We have utilized the Finite Element Method (FEM) to simulate the effects of different blood flow rates, in several geometries, on the near infrared measurements. The results show clearly that co-existence of two blood flow velocities can result in a bi-phasic change in optical density, regardless of the orientation of vessels. This study supports our previous hypothesis that the bi-phasic tumor hemodynamic feature during carbogen inhalation results from a well-perfused and a poorly perfused region in the tumor vasculature.

©2005 Optical Society of America

**OCIS codes:** (000.4430) Numerical approximation and analysis; (170.3660) light propagation in tissues; (170.5280) photon migration; (170.6510) Spectroscopy, tissue diagnostics; (290.1990) diffusion.

---

## References and links

1. P. Vaupel, O. Thews, D. K. Kelleher, and M. Höckel, "Current status of knowledge and critical issues in tumor oxygenation," In: Hudetz and Bruley (eds), *Oxygen Transport to Tissue XX*, 591-602 (Plenum Press, New York, 1998).
2. P. Vaupel, "Vascularization, blood flow, oxygenation, tissue pH, and bioenergetic status of human breast cancer," In: Nemoto and LaManna (eds), *Oxygen Transport to Tissue XVIII*, 243-253 (Plenum Press, New York, 1997).
3. P. Vaupel, "Oxygen transport in tumors: Characteristics and clinical implications," *Adv. Exp. Med. Biol.*, **388**, 341-351 (1996).
4. R. H. Thomlinson, and L. H. Gray, "The histological structure of some human lung cancers and the possible implications for radiotherapy," *Br. J. Cancer*, **9**, 539-549 (1955).
5. E. E. Schwartz, *The biological basis of radiation therapy* (Lippincott, Philadelphia, 1966).
6. B. Teicher, J. Lazo, and A. Sartorelli, "Classification of antineoplastic agents by their selective toxicities toward oxygenated and hypoxic tumor cells," *Cancer Res.*, **41**, 73-81 (1981).
7. J. D. Chapman, C. C. Stobbe, M. R. Arnfield, R. Santus, J. Lee, and M. S. McPhee, "Oxygen dependency of tumor cell killing in vitro by light activated photofrin II," *Radiat. Res.*, **126**, 73-79 (1991).
8. P. Bergsjö and P. Kolstad, "Clinical trial with atmospheric oxygen breathing during radiotherapy of cancer of the cervix," *Scand. J. Clin. Lab. Invest. Suppl.*, **106**, 167-171 (1968).
9. H. D. Suit, N. Marshall, and D. Woerner, "Oxygen, oxygen plus carbon dioxide, and radiation therapy of a mouse mammary carcinoma. *Cancer*," *Cancer*, **30**, 1154-1158 (1972).
10. H. Liu, Y. Song, K. L. Worden, X. Jiang, A. Constantinescu, and R. P. Mason, "Noninvasive Investigation of Blood Oxygenation Dynamics of Tumors by Near-Infrared Spectroscopy," *Appl. Opt.*, **39**, 5231-5243 (2000).
11. J. G. Kim, D. Zhao, Y. Song, A. Constantinescu, R. P. Mason, and H. Liu, "Interplay of Tumor Vascular Oxygenation and Tumor pO<sub>2</sub> Observed Using NIRS, pO<sub>2</sub> Needle Electrode and <sup>19</sup>F MR pO<sub>2</sub> Mapping," *J. of Biomed. Opt.*, **8**, 53-62 (2003).

12. Y. Gu, V. A. Bourke, J. G. Kim, A. Constantinescu, R. P. Mason, and H. Liu, "Dynamic response of breast tumor oxygenation to hyperoxic respiratory challenge monitored with three oxygen-sensitive parameters," *Appl. Opt.*, **42**, 2960-2967 (2003).
13. S. S. Kety, "The theory and applications of the exchange of inert gas at the lungs and tissue," *Pharmacol. Rev.*, **3**, 1-41 (1951).
14. A.H. Hielscher, S. L. Jacques, L. Wang, and F. K. Tittel, "The influence of boundary conditions on the accuracy of diffusion theory in time-resolved reflectance spectroscopy of biological tissues," *Phys. Med. Biol.*, **40**, 1957-1975 (1995).
15. R.A. Groenhuis, A.A. Ferwerda, and J. J. T. Bosch, "Scattering and absorption of turbid materials determined from reflection measurements. 1: Theory," *Appl. Opt.*, **22**, 2456-2462 (1983)
16. J. B. Mandeville, J.J.A. Marota, C. Ayata, G. Zaharchuk, M.A. Moskowitz, B. R. Rosen, and R. M. Weisskoff, "Evidence of a cerebrovascular postarteriole windkessel with delayed compliance," *J. Cereb. Blood Flow Metab.*, **19**, 679-689 (1999).
17. M. E. Brevard, T. Q. Duong, J. A. King, and C. F. Ferris, "Changes in MRI signal intensity during hypercapnic challenge under conscious and anesthetized conditions," *Magn. Res. Imaging.*, **21**, 995-1001 (2003).
18. H. Liu, A. H. Hielscher, F. K. Tittel, S. L. Jacques, and B. Chance, "Influence of Blood Vessels on the Measurement of Hemoglobin Oxygenation as Determined by Time-Resolved Reflectance Spectroscopy," *Medical Physics*, **22**, 1209-1217 (1995).
19. Y. Gu, R. Mason, and H. Liu, "Estimated fraction of tumor vascular blood contents sampled by near infrared spectroscopy and <sup>19</sup>F magnetic resonance spectroscopy," *Optics Express*, **13**, 1724-1733 (2005).  
<http://www.opticsexpress.org/abstract.cfm?URI=OPEX-13-5-1724>
20. M. Xia and H. Liu, "A model of the hemodynamic response of tumor in rats with hyperoxic gas challenge", *Optical Tomography and Spectroscopy of Tissue VII*, B. Chance, R. R. Alfano, B. J. Tromberg, M. Tamura, and E. M. Sevick-Muraca, eds., Proc. SPIE 5693, in press (2005).
21. D. A. Boas, G. Strangman, J. P. Culver, R. D. Hoge, G. Jaszewski, R. A. Poldrack, B. R. Rosen, and J. B. Mandeville, "Can the cerebral metabolic rate of oxygen be estimated with near-infrared spectroscopy?" *Phys. Med. Biol.*, **48**, 2405-2418 (2003).
22. A. R. Padhani, A. Dzik-Jurasz, "Perfusion MR imaging of extracranial tumor angiogenesis," *Top. Magn. Reson. Imaging*, **15**, 41-57 (2004).
23. A. Y. Bluestone, M. Stewart, J. Lasker, G.S. Absoulaev, and A. H. Hielscher, "Three-dimensional optical tomographic brainimaging in small animals, part I: hypercapnia," *J. Biomed. Opt.*, **9**, 1046-1062 (2004).
24. E. Rostrup, I. Law, F. Pott, K. Ide and G. M. Knudsen, "Cerebral hemodynamics measured with simultaneous PET and near-infrared spectroscopy in humans," *Brain research*, **954**, 183-193 (2002).
25. R.B. Buxton, E.C. Wong, and L.R. Frank, "Dynamics of blood flow and oxygenation changes during brain activation: the balloon model," *Magn. Reson. Med.*, **39**, 855-864 (1998).
26. K. J. Friston, A. Mechelli, R. Turner and C. J. Price, "Nonlinear Responses in fMRI: The Balloon Model, Volterra Kernels, and Other Hemodynamics," *NeuroImage*, **12**, 466-477 (2000).
27. A. Mechelli, C. J. Price and K. J. Friston, "Nonlinear Coupling between Evoked rCBF and BOLD Signals: A Simulation Study of Hemodynamic Responses," *NeuroImage*, **14**, 862-872 (2001).
28. Y. Zheng, J. Martindale, D. Johnston, M. Jones, J. Berwick, and J. Mayhew, "A Model of the hemodynamic Response and Oxygen Delivery to Brain," *NeuroImage*, **16**, 617-637 (2002).
29. R. B. Buxton, K. Uludağ, D. J. Dubowitz, and T. T. Liu, "Modeling the hemodynamic response to brain activation," *NeuroImage*, **23**, S220-S233 (2004).
30. K. Lu, J. W. Clark, Jr., F. H. Ghorbel, C. S. Robertson, D. L. Ware, J. B. Zwischenberger, and A. Bidani, "Cerebral autoregulation and gas exchange studied using a human cardiopulmonary model," *Am. J. Physiol. Heart. Circ. Physiol.*, **286**, H584-H601 (2004).
31. R. K. Jain, "Determinants of tumor blood flow: a review," *Cancer Res.*, **48**, 2641-2658 (1988).
32. R. K. Jain, "Barriers to drug delivery in solid tumors," *Sci. Am.*, **271**, 58-65 (1994).
33. R. Mazurchuk, R. Zhou, R. M. Straubinger, R. I. Chau, and Z. Grossman, "Functional magnetic resonance (fMR) imaging of a rat brain tumor model: implications for evaluation of tumor microvasculature and therapeutic response," *Magn. Reson. Imaging*, **17**, 537-548 (1999).
34. Y. Song, A. Constantinescu, R.P.Mason, "Dynamic breast tumor oximetry: the development of prognostic radiology," *Technology in Cancer Research & Treatment*, **1**, 1-8 (2002).

---

## 1. Introduction

It is well known that solid tumors develop regions of hypoxia during their growth due to an imbalance between the rate of tumor cell proliferation and branching-of the blood vessels [1-3]. Tumor hypoxia can contribute to the failure of radiotherapy [4,5], some forms of chemotherapy [6], and photodynamic therapy [7]. Therefore, increasing tumor oxygenation could be very helpful to improve cancer therapy efficacy. As one means to improve tumor oxygenation, breathing a hyperoxic gas has been used to enhance the cancer treatment [8,9]. Our previous *in vivo* animal studies have clearly demonstrated that either carbogen (95% CO<sub>2</sub>

and 5% O<sub>2</sub>) or 100% oxygen inhalation can improve the vascular oxygen level of breast and prostate tumors [10-12]. Specifically, the observed changes in oxygenated hemoglobin concentration ( $\Delta[\text{HbO}_2]$ ) of tumor vasculature exhibited a bi-phasic feature: a rapid increase, followed by a gradual but significant increase, in response to carbogen intervention (Fig. 1) [12].

To explain this biphasic behavior of tumor hemodynamics, we established a mathematical model based on Kety's approach [13] in our earlier publication [10]. We formed a hypothesis in Ref. 10 that tumor vasculature is comprised of a well-perfused and poorly perfused region that can be detected with the two time constants through  $\Delta[\text{HbO}_2]$  readings derived from near infrared spectroscopy (NIRS). The mathematical model basically allowed us to associate the bi-phasic  $\Delta[\text{HbO}_2]$  amplitudes and time constants to the ratio of vascular coefficients and vascular perfusion rates in the two different regions [10]. While the mathematical model seemed useful for interpretation of tumor hemodynamics and physiological factors, it was a suggested model without experimental or computational proof or confirmation at the time. To provide solid support and better understanding for this model and to further investigate heterogeneities of tumor vasculature, we have used a computational approach to validate the dynamic NIRS measurements. The computational results given in this study strongly demonstrates that with our bi-phasic mathematical model, tumor vascular dynamics can be determined and monitored non-invasively using NIRS while a perturbation of hyperoxic gas intervention is given.

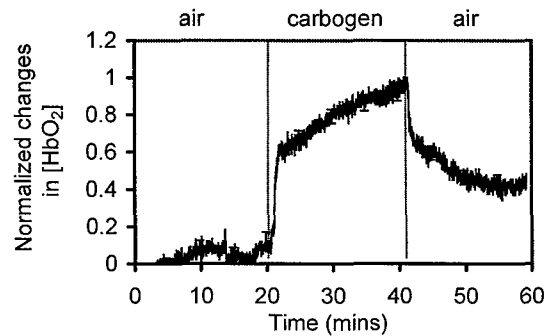


Fig. 1 Normalized hemodynamic changes of tumor blood oxygenation,  $\Delta[\text{HbO}_2]$ , obtained with the NIRS measurement from a rat breast tumor while the breathing gas was switched from air to carbogen (Gu *et al.* Applied Optics, 2003) [Error! Bookmark not defined.].

## 2. Review of the our mathematical model of tumor vascular oxygenation

In our previous report [10], we followed an approach used to quantify regional cerebral blood flow ( $r\text{CBF}$ ) with diffusible radiotracers, as originally developed by Kety [13] in the 1950's. By applying Fick's principle and defining  $\gamma$  as the ratio of  $\Delta[\text{HbO}_2]$  in the vascular bed to that in veins,  $\Delta[\text{HbO}_2]$  induced by hyperoxic gas intervention in tumor vasculature could be mathematically modeled as Eq. (1):

$$\Delta[\text{HbO}_2]_{\text{vasculature}}(t) = \gamma H_o [1 - \exp(-t/\gamma)] = A [1 - \exp(-t/\tau)], \quad (1)$$

where  $\gamma$  was defined as the vasculature coefficient of the tumor ( $=\Delta[\text{HbO}_2]_{\text{vasculature}}/\Delta[\text{HbO}_2]_{\text{vein}}$ ),  $H_o$  was the arterial oxygenation input,  $f$  represented the blood perfusion rate in  $\text{cm}^3/\text{sec}$ ,  $\tau$  is the time constant,  $A=\gamma H_o$ , and  $\tau=\gamma/f$ .

If a tumor has two distinct perfusion regions and the measured NIRS signals result from the both regions (Figure 2), it is reasonable to include two different blood perfusion rates,  $f_1$  and  $f_2$ , and two different vasculature coefficients,  $\gamma_1$  and  $\gamma_2$ , in the model. Eq. (1) becomes Eq. (2) to count for the double exponential feature observed in the NIRS experiments:

$$\begin{aligned}\Delta[\text{HbO}_2]_{\text{vasculature}}(t) &= \gamma_1 H_0 [1 - \exp(-f_1 t / \gamma_1)] + \gamma_2 H_0 [1 - \exp(-f_2 t / \gamma_2)] \\ &= A_1 [1 - \exp(-t / \tau_1)] + A_2 [1 - \exp(-t / \tau_2)]\end{aligned}\quad (2)$$

where  $f_1$  and  $\gamma_1$  are the blood perfusion rate and vasculature coefficient in the well perfused region, respectively;  $f_2$  and  $\gamma_2$  represent the same respective meanings for the poorly perfused region, and  $A_1 = \gamma_1 H_0$ ,  $A_2 = \gamma_2 H_0$ ,  $\tau_1 = \gamma_1 / f_1$ ,  $\tau_2 = \gamma_2 / f_2$ . Since  $A_1$ ,  $A_2$ ,  $\tau_1$ , and  $\tau_2$  can be determined by fitting Eq. (2) with  $\Delta[\text{HbO}_2]$  readings taken from the NIRS measurements, we can obtain the ratios of two vasculature coefficients and the two blood perfusion rates as:

$$\frac{\gamma_1}{\gamma_2} = \frac{A_1}{A_2} \quad \frac{f_1}{f_2} = \frac{A_1 / \tau_1}{A_2 / \tau_2}\quad (3)$$

With these two ratios, we are able to understand more about tumor vascular structures and blood perfusion rates. In this paper, we report our computational evidence to support the tumor hemodynamics model by quantifying  $\gamma_1 / \gamma_2$  and  $f_1 / f_2$  from three different locations of the simulated tumor dynamic phantoms.

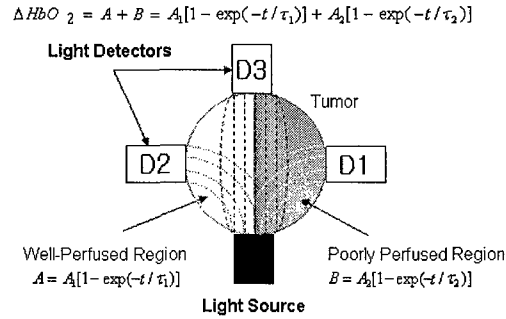


Fig. 2. A schematic diagram of light transmitting patterns in a tumor when the tumor has two distinct perfusion regions. The right side of tumor with gray color represents the poorly perfused region, whereas the left side of tumor corresponds to a well-perfused region. As shown, different detectors may interrogate different tumor volumes.

### 3. Computer simulations using the finite element method

The Finite Element Method (FEM) was utilized to simulate the bi-phasic behavior of increases in  $\Delta[\text{HbO}_2]$  with FEMLAB software (COMSOL Inc. Burlington, MA). It uses the numerical approach to solve partial differential equations (PDE) in modeling and simulating various engineering problems. The geometry of our FEM simulations is given in Figure 3, representing the simplified tumor vascular model (Fig. 2). E1 represents an overall tumor volume (diameter = 4 cm), and R5 shows the location of light source. Blood vessels in two different perfusion regions are represented by several rectangles (0.1 cm x 2.4 cm): R1 and R2 represent vessels with a fast flow rate, and R3 and R4 denote vessels with a slow flow rate.

As given in Eq. (4), the diffusion equation was applied to predict the measured NIR light intensities along the boundary of simulated model as the simulated oxygenated blood flows through the blood vessels with two different perfusion rates in tumors:

$$(1/c)(\partial/\partial t)\phi(r,t) - D\nabla^2\phi(r,t) + \mu_a\phi(r,t) = S(r,t)\quad (4)$$

where  $\phi(r,t)$  is the diffuse photon fluence rate at the position  $r$ ,  $c$  is the speed of light in tissue,  $S(r,t)$  describes the photon source,  $D = [3(\mu_a + \mu_s')]^{-1}$  is the diffusion coefficient,  $\mu_a$  is the light absorption coefficient in tissue, and  $\mu_s'$  is the reduced light scattering coefficient in tissue. For the boundary conditions, the extrapolated boundary condition which mathematically assumes

that photon flux vanishes at the extrapolated distance,  $Z_e$  [14], was applied to the FEM model as given below:

$$Z_e = \phi(z=0) / [(\partial / \partial z)\phi(r, z, t)]_{t=0} = 2AD, \quad \phi(r, z = z_e, t) = 0 \quad (5)$$

where  $A=(1+r_d)/(1-r_d)$ , and  $r_d$  is the internal reflectance caused by the refractive index mismatch between air and tissue. This can be estimated using the following empirically determined equation [15]:

$$r_d = -1.440 n^2 + 0.710 n^{-1} + 0.668 + 0.0636 n \quad (6)$$

with  $n = n_{\text{tissue}}/n_{\text{air}}$ .

In the simulation, 1.4 and 1.0 were used for  $n_{\text{tissue}}$  and  $n_{\text{air}}$ , respectively, to obtain  $A$ . A value of  $D=0.033$  cm was chosen for both the background and vasculature of phantom with  $\mu_s'=10$  cm<sup>-1</sup>. The values of 0.03 cm<sup>-1</sup> and 1.5 cm<sup>-1</sup> were selected as absorption coefficients of the tissue background (E1) and oxygenated blood flowing through the simulated vessels (R1, R2, R3 and R4), respectively. In this simulation model, the absorption coefficients of perfused blood prior to carbogen intervention was assumed to be the same as tissue background since we are measuring only changes of tumor blood oxygenation from the baseline (air) to carbogen intervention. Therefore, the value of 1.5 cm<sup>-1</sup> used in R1-R4 can be considered as a difference in absorption between preperfused blood and oxygenated blood after carbogen intervention. The simulation model was generated with FEMLAB having 1147 elements and 609 nodes. Finally, the model was solved using the stationary nonlinear solver type.

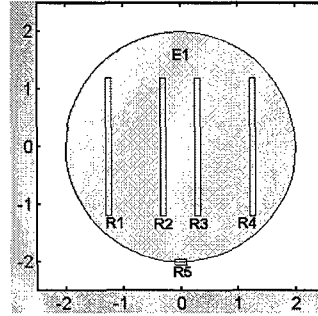


Fig. 3. The geometry used in our FEM simulations for a simplified tumor vascular model. R1 and R2 rectangles are located in a fast flow region, while R3 and R4 are in a slow flow region within tumor. The units for both the X-axis and Y-axis are cm. The distances from R1 to R2 and from R2 to R3 are 1 cm and 0.5 cm, respectively.

To model the dynamic NIR signals, multiple FEM runs of the diffusion model with Eqs. (4)–(6) were performed repeatedly with different lengths of R1, R2 and R3, R4, where the  $\mu_a$  value of 1.5 cm<sup>-1</sup> was used to simulate oxygenated blood within R1, R2, R3, and R4 regions. Each of the computed run/frame from the model was associated with the blood perfusion in the two vascular regions at a selected time. By assuming both vascular regions in tumors are having a same vascular density, the perfusion rates of two regions is directly proportional to the blood flow rates. Therefore, the two different flow rates/perfusion rates passing through the two regions in tumors were mimicked by progressing the lengths of R1, R2 from 0 to 2.4 cm with an increment of 0.4 cm per frame to represent the fast flow process, and the lengths of R3, R4 with a smaller increment of 0.02 cm per frame were used to evolve the slow flow.

Figure 4 shows an example of a series of continuous FEM outputs for the fast flow case, where each of the output frames corresponds to a time interval of 2 seconds. The frame rate in the calculation was kept the same for both fast and slow cases; thus, a series of discrete outputs of the FEM model can replicate the time-dependent NIR signals taken from the *in vivo*

tumor model with a flow rate difference as large as 20 times between the two different perfusion regions.

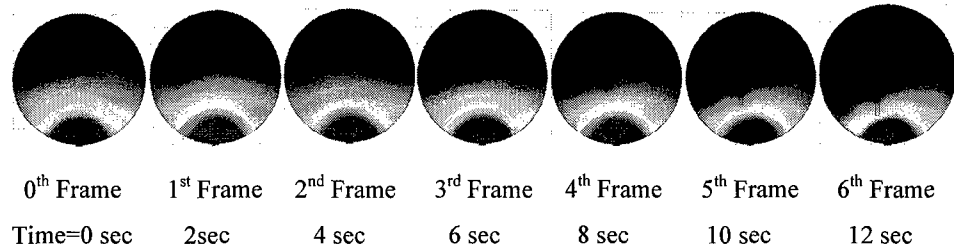


Fig. 4. Light distribution inside of a simplified tumor vascular model simulated by FEM with the increase of R1 and R2 length to mimic the oxygenated blood flow in the well perfused region. (Movie: 267 KB)

To investigate if the bi-phasic hemodynamic feature depends on the orientations of the vessels, we also changed the position of source light to examine the effect of vessel geometry on NIR signals taken from the tumor hemodynamic measurements. We have simulated the light source to be a) perpendicular to the vessels of the phantom and b) at the center of the phantom. In the former case, the light penetrates the slow-flow vessels first and then the fast-flow vessels. Such a simulation allowed us to investigate if in this geometry, the dynamic changes of NIR signals still have the bi-phasic behavior.

Changes in optical density ( $\Delta O.D.$ ) are used to calculate changes in photon fluence rates,  $\phi$ , induced by the simulated flows along the boundary of phantom. Such  $\Delta O.D.$  values are analogous to those observed in our previous animal experiments [10]; they are expressed as:

$$\Delta O.D. = \log \left( \frac{\phi_{initial}}{\phi_{transient}} \right) \quad (7)$$

where  $\phi_{initial}$  and  $\phi_{transient}$  are the photon fluence rates at the initial and transient states.

#### 4. Results from the FEM simulation

Figure 4 given above shows light distributions in a simplified tumor vascular model from seven simulation outputs to mimic a fast oxygenated blood flow in tumor by increasing the length of R1 and R2 with an increment of 0.4 cm per each frame, or 0.2 cm per second. The 0th frame shows the light distribution in tumor vascular model when there is no blood flow, and all the other frames represent the light distributions with a fast oxygenated blood flow in R1 and R2. In a similar fashion, a slow flow rate of oxygenated blood in the poorly perfused region was simulated by increasing the length of R3 and R4 with a much slower rate of 0.02cm/frame (0.01 cm/sec).

Figure 5(a1) presents the light distribution of the simulated model when a fast oxygenated blood flow passed through R1 and R2 with a rate of 0.2 cm/sec; similarly, Fig. 5(b1) shows the light distribution when an oxygenated blood flow went into R3 and R4 with a slow flow rate of 0.01 cm/sec. Finally, Fig. 5(c1) shows the combined light distribution in the phantom with both fast and slow flows in the two different regions. Figure 5(a1) is the result at the 6th frame, while Fig. 5(b1) results from the 120th frame. Figure 5(c1) is also the simulation output at the 120th frame when the oxygenated blood flows passed through the entire lengths of all the simulated vessels.

In comparison with the results from our animal experiments [10-12], we extracted the light intensity values (proportional to the photon fluence rates,  $\phi$ ) at three positions of (2,0), (-2,0) and (0,2) from each frame of the simulations to calculate  $\Delta O.D.$  values, which are plotted in

the right column of Fig. 5. These three positions are corresponding to D1, D2 and D3 in Fig. 2. The time unit in these plots was obtained by associating each frame to 2 seconds. Thus,  $\Delta O.D.$  shown in Fig. 5(a1) has 12 seconds to reach the maximum  $\Delta O.D.$  since it has only 6 frames to simulate a fast flow rate, with a velocity of 0.2cm/sec. Similarly,  $\Delta O.D.$  values in Fig. 5(b1) and 5(c1) will have 240 seconds to achieve their maximums because they have 120 frames to simulate a slow flow rate, with a velocity of 0.01 cm/sec.

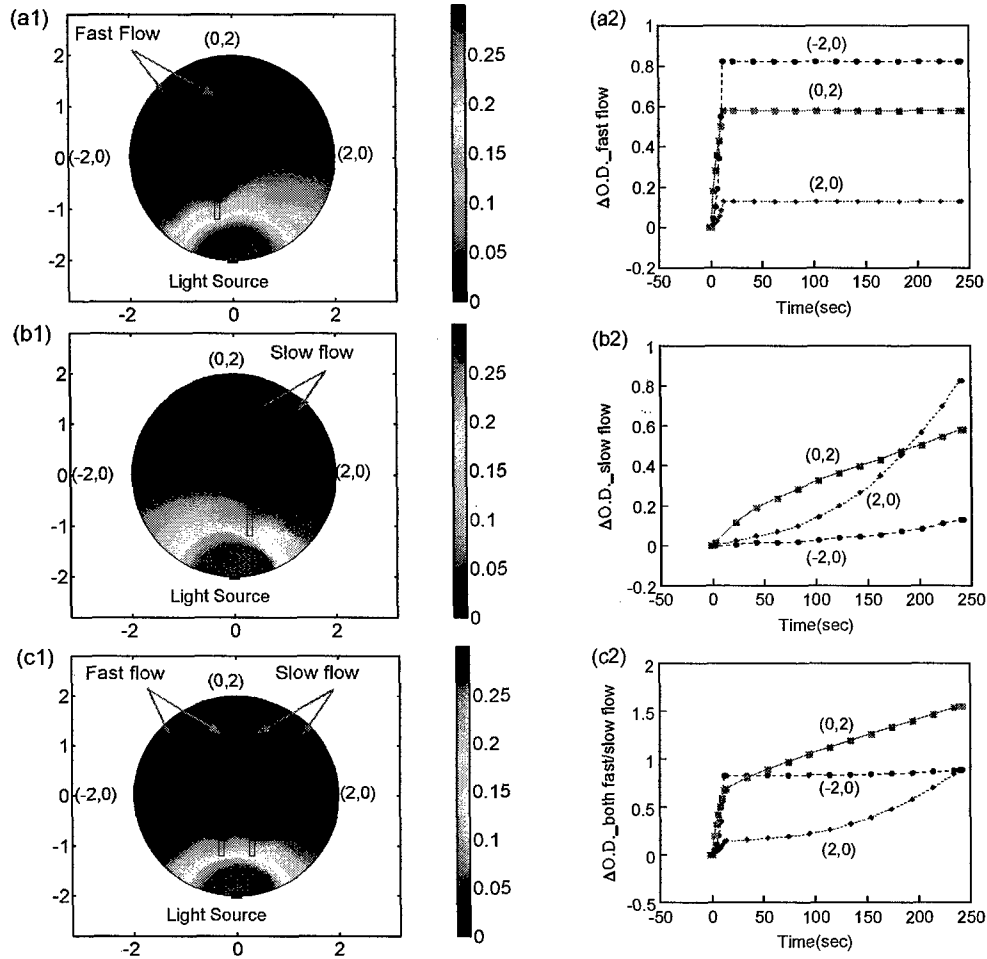


Fig. 5. Light distributions inside of a simplified tumor vascular model simulated by the FEM. Left column: (a1) is the output result with an only fast simulated flow rate (R1 and R2), (b1) is the result with an only slow flow rate (R3 and R4) (Movie: 1,763 KB), and (c1) is the result with both fast and slow flow combined (R1, R2, R3 and R4) (Movie: 1,643 KB). Right column: Optical density changes measured at three locations, (2,0), (-2,0), and (0,2), in the FEM simulations during fast flow only (a2), slow flow only (b2), and both fast and slow flow combined (c2).

Figure 5(a2) and 5(b2) show temporal  $\Delta O.D.$  profiles taken from the three positions during a fast flow only and a slow flow only simulation, respectively. The former one shows that the  $\Delta O.D.$  is the largest at (-2, 0) position and is the smallest at (2, 0) position when an oxygenated blood flow passes only into the vessels (R1 and R2) near D2 in the simulation. Similar results are observed when the blood flowed only into the vessels in the slow perfusion

region (R3 and R4), as seen in Fig. 5(b2). Namely, the  $\Delta O.D.$  values are much larger at (2, 0) position than at (-2, 0). Moreover, Fig. 5(c2) shows that the temporal profiles of  $\Delta O.D.$  taken at (2, 0) and (-2, 0) positions do not change significantly in comparison with those given in Figs. 5(a2) and 5(b2). However, in this case, the temporal  $\Delta O.D.$  profile at (0, 2) position clearly shows a bi-phasic behavior, similar to that shown in Fig. 1, as we often observed in the animal tumor studies [10-12]. Notice that the portions in the  $\Delta O.D.$  profile seem to be equally weighted by the fast and slow flows, implying that the fast and slow flows contribute to the measured NIR signals approximately equivalently. This indeed supports that it is necessary to contain two distinct flow or perfusion rates within tumors in order to exhibit the bi-phasic blood oxygenation dynamics during carbogen/oxygen inhalations.

We also changed the position of light source to be perpendicular to the vessels on the simulated phantom, as shown in Fig. 6(a1), or to be at the center of the phantom, shown in Fig. 6(b1). In this way, we can investigate how blood vessel geometry within the tumor/phantom affects the bi-phasic feature of the tumor hemodynamics.

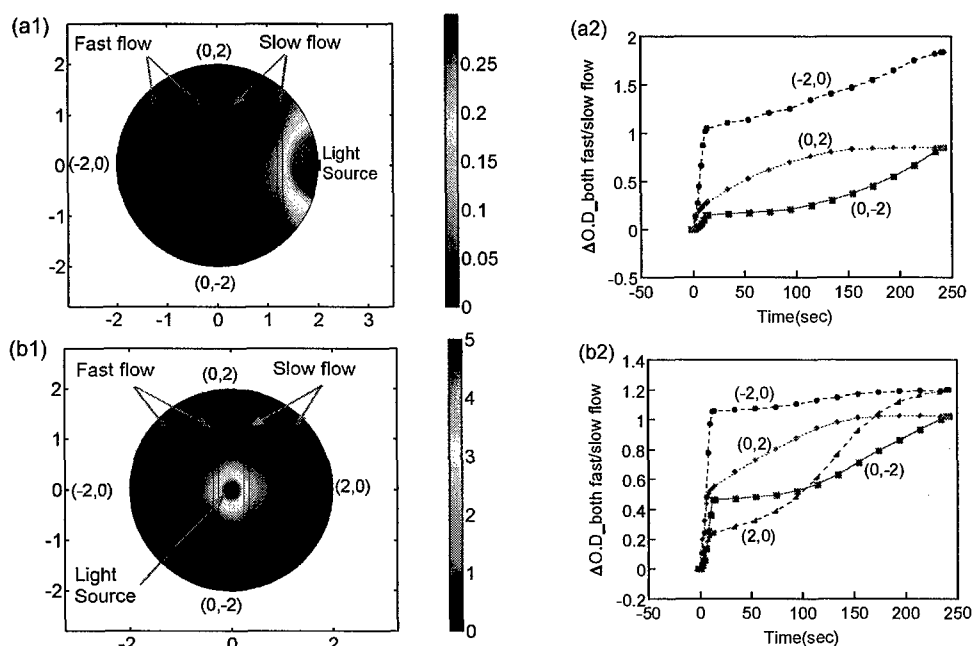


Fig. 6. FEM simulations of light distribution inside of a simplified tumor vascular model. Left column: (a1) shows the results when the light source is located perpendicular to the vessels (Movie: 1,539 KB), (b1) presents the results when the light source is located in the center of the model (Movie: 1,540 KB). Right column: Changes in O.D. measured at three locations, as labeled in Fig. 6(a1), with a fast and slow flow combined. (a2) plots three  $\Delta O.D.$  profiles measured at the respective locations; (b2) reveals four  $\Delta O.D.$  temporal profiles during the combined fast and slow flow.

Similar to Fig. 5(c1), Fig. 6(a1) shows light distribution within the simulated model when an oxygenated blood flow passed through R1 and R2 with a fast flow rate of 0.2 cm/sec and through R3 and R4 with a slow rate of 0.01 cm/sec. Temporal profiles of  $\Delta O.D.$  at the three corresponding positions were quantified and plotted in Figs. 6(a2). It shows that the detector at (0, 2) sees the change in optical density with a single-exponential shape, more dominated by the slow flow, while the detector at (0, -2) detects a small initial rise in  $\Delta O.D.$  induced by the fast flow, followed by a gradual plateau and then a large increase by the slow flow. Such features can be expected based on their detection positions. Interestingly, the  $\Delta O.D.$  profile

taken at (-2, 0) exhibits an unambiguous bi-phasic exponential curve that results from both the fast and slow flow. This curve resembles very well the previously observed feature in our animal studies (see Fig. 1 as an example).

Figures 6(b1) and 6(b2) simulate the light distribution and  $\Delta O.D.$  profiles, respectively, obtained from the four positions of the tumor vascular dynamic phantom with the light source located at the center. The latter one displays that the detector at (-2, 0) is most sensitive to the signal from the fast flow only, while the readings of  $\Delta O.D.$  at (2, 0) is affected by the fast flow at the initial onset and followed by a gradual increase. Furthermore, the  $\Delta O.D.$  readings at (0, 2) and (0, -2) reveal somewhat bi-phasic behaviors with a fast increase in  $\Delta O.D.$  initially, followed by an exponential and delayed exponential rise, respectively. These two bi-phasic profiles can be attributed to the fact that the detected NIR signals at (0, 2) and (0, -2) interrogated both fast and slow perfusion regions.

## 5. Discussion and conclusion

In this study, we employed the FEM method to simulate the bi-phasic behavior that was frequently observed in blood oxygenation from animal tumors during carbogen/oxygen inhalation. We believe that the bi-phasic feature of tumor blood oxygenation during hyperoxic gas inhalation results from two distinct vascular structures of the tumor, namely, a well-perfused and poorly perfused region. Our numerical simulations were performed to explore what can cause tumor hemodynamics to have two time constants, i.e., the bi-phasic feature. From the simulation results, it is confirmed that co-existence of two blood flow velocities can result in a bi-phasic change in optical density, thus leading further to a bi-phasic change in hemodynamics in tumor vasculature.

A comparison between Figs. 5(c2) and 6(a2) reveals that the bi-phasic or bi-exponential feature can be well present if both slow and fast perfusion regions exist within the interrogated area or volume of NIR source and detector, regardless of the orientation of vessels. Single exponential or non-exponential component of  $\Delta O.D.$  exists if the NIR source and detector interrogates only the fast or slow perfusion area. Moreover, the contribution of each perfusion region to the NIR signal appears to be proportional to the vascular area or volume, i.e., the areas of R1, R2, R3, and R4 in this study. While we learned that different flow velocities gave rise to bi-exponential profiles, such differences in flow velocity could arise from different blood vessel diameters with the same blood flow rate or from different blood flow rates with the same vessel diameter, both of which tumor vasculatures have. Detailed association between the measured NIR signals and vascular density and vessel sizes needs to be explored further in our future studies.

In comparison, such a bi-phasic change in hemodynamics has been observed in MRI (Magnetic Resonance Imaging) studies during hypercapnic intervention or brain functional stimulation [16,17]. Mandeville *et al.* have developed a modified Windkessel model to explain the bi-phasic increase of relative cerebral blood volume (rCBV) during 30 seconds of electrical stimulation on rat forepaw [16]. They explained the acute increase of rCBV by the fast elastic response from both capillary and vein and the slow increase of rCBV by a delayed venous compliance. Functional MRI can detect signals from large blood vessels such as artery and vein as well as those from small vessels including capillaries, while the NIRS measurement is most sensitive to microvessels [18,19]. Therefore, the bi-phasic changes of  $\Delta[HbO_2]$  observed by NIRS during carbogen intervention may not necessarily follow the same principle as explained by the modified Windkessel model.

In addition, the response of rCBV and relative cerebral blood flow (rCBF) in the brain due to stimulation is much faster than the blood oxygenation changes in tumor during carbogen intervention. The time constants of rapid and slow increases in rCBV were  $1.9 \pm 0.7$  second and  $14 \pm 13$  second [16], respectively, while the time constants of increases in  $\Delta[HbO_2]$  in rat breast tumors during carbogen inhalation were much slower, varying from 3.9 sec to 150 seconds (mostly 20-60 second) for the rapid increase and 180 to 1500 sec during the gradual increase [10-12]. This suggests that the bi-phasic feature obtained in  $\Delta[HbO_2]$  during tumor

oxygenation may be a physiological and hemodynamic characteristic different from that observed in the brain. We are currently investigating the association between our experimental data and the modified Windkessel model [20], following the approach that estimates the relative cerebral metabolic rate of oxygen ( $rCMRO_2$ ) developed by Boas et al [21].

Padhani and Dzik-Jurasz have reviewed the heterogeneity in perfusion from extracranial tumors measured by dynamic contrast-enhanced MR imaging (DCE-MRI) [22]. They have shown that the kinetics of signal intensity changes obtained from T2\*- or T1-weighted images are significantly varying within a tumor. Especially, Figs. 4 and 5 in their paper clearly support that the bi-phasic increase of  $\Delta[HbO_2]$  from rat breast tumors during carbogen intervention could be from different perfusion rates in tumors, given that our single channel NIRS obtains global changes in tumor hemodynamics. In addition, other reports presented cerebral oxygenation during a relatively long period of hypercapnic challenge, e.g. 2 minutes [23] or 10 minutes [24], and did not show the bi-phasic feature in  $\Delta[HbO_2]$ .

Various mathematical models have been proposed to understand the cerebral hemodynamic parameters, including BOLD MRI signal,  $rCMRO_2$ ,  $rCBV$ ,  $rCBF$  during stimulation or hypercapnic intervention [16,25-30]. Since  $\Delta[HbO_2]$  was showing large changes during carbogen inhalation in our NIRS measurements, we have adopted  $\Delta[HbO_2]$  as a sensitive parameter to obtain tumor hemodynamic features, just like changes in deoxyhemoglobin concentration used in BOLD MRI. Solid tumors are known to have both temporal and spatial heterogeneity in blood flow [31], and tumor blood vessels are much leakier and more porous than normal blood vessels [32]. Therefore, tumor hemodynamics may not follow the currently established mathematical models that estimate cerebral hemodynamics by considering autoregulation and vessel reactivity. Based on the fact that solid tumors develop hypoxic regions which are poorly perfused in the center as they grow [33,34], we hypothesized that the bi-phasic feature of  $\Delta[HbO_2]$  stems from two different perfusion rates in tumors. Our approach is a simpler mathematical model in comparison with those presented for cerebral hemodynamic models. In our current study, we do not measure blood flow changes in tumor, and thus we could only obtain the ratio of vascular coefficients and perfusion rates by fitting the increase of  $\Delta[HbO_2]$  [10]. To overcome this limitation, recently, we have followed an approach that estimates the  $rCMRO_2$  developed by Boas et al. [21] to evaluate changes in tumor blood flow and metabolic rate of oxygen in tumor [20].

In this numerical study, we have simplified the physiological complex of tumors in their hemodynamic structures by assuming the same absorption coefficients for the perfused blood prior to carbogen intervention and tissue background. While this simplified assumption is not realistic in actual tumors, the overall trend of mathematical simulations would remain the same. This is because the numerical simulations will always provide us with changes in light intensity during tumor blood oxygenation, if an absorption difference exists in blood vasculature between the baseline (air) and carbogen intervention. With our current assumption and modeling setup, we are able to enhance the bi-phasic feature for easy observation.

While the tumor vasculature and hemodynamics is very complex and chaotic, a simple numerical model, as we demonstrated in this study, can support an initial mathematical hypothesis for tumor modeling, help us understand and interpret our experimental data, and lead to further development of more complex and realistic models for tumor investigations. The goal of this numerical study is not to develop a comprehensive computational model for tumors, but rather focusing on numerical support to better understand our experimental observation during tumor oxygenation measured with NIRS.

In summary, we have previously used a single-channel NIRS system for global measurements of  $\Delta[HbO_2]$  in tumors during respiratory challenges [10-12], demonstrating that NIRS is a portable, low cost, and real time measurement system that can monitor changes of vascular oxygen levels in tumor tissues non-invasively. Now, the current study confirms that an NIRS multi-channel approach has great potential to detect and monitor tumor heterogeneity under therapeutic or adjuvant interventions. With an appropriate mathematical model, tumor vascular dynamics can be determined and monitored non-invasively while a

perturbation of hyperoxic gas intervention is given. Our future work includes 1) to further investigate and understand the meaning of vasculature coefficient,  $\gamma$  and 2) to develop an NIR imaging system to be used as a monitoring tool for the efficacy of cancer therapy.

**Acknowledgements**

This work was supported in part by the Department of Defense Breast Cancer Research grants DAMD17-03-1-0353 (JGK) and DAMD17-00-1-0459 (HL) as well as by the National Institutes of Health 1R21CA101098-01 (HL).

# Investigation of bi-phasic tumor oxygen dynamics induced by hyperoxic gas intervention:

## *The dynamic phantom approach*

Jae G. Kim and Hanli Liu\*

Joint Graduate Program in Biomedical Engineering,

University of Texas Southwestern Medical Center at Dallas/ University of Texas at Arlington

Arlington, TX 76019

©2005 Optical Society of America

### ***OCIS codes:***

- OCIS #:* 170.1470, *blood/tissue constituent monitoring;*  
*OCIS #:* 170.3660, *light propagation in tissues;*  
*OCIS #:* 170.4580, *optical diagnostics for medicine;*  
*OCIS #:* 170.5280, *photon migration;*  
*OCIS #:* 170.6510, *Spectroscopy, tissue diagnostics;*  
*OCIS #:* 290.1990, *diffusion;*  
*OCIS #:* 290.7050, *turbid media.*

## ABSTRACT

We have developed dynamic tumor vascular phantoms and utilized them to investigate the bi-phasic behavior of increases in oxygenated hemoglobin concentration that was observed *in vivo* from rat breast tumors during carbogen/oxygen inhalation. The experimental setup included a continuous-wave, multi-channel, near infrared spectroscopy (NIRS) system and syringe pumps to drive the simulated blood through the dynamic vascular phantoms. The results from such phantom experiments show clearly that the two time constants observed in tumor oxygenation dynamics *in vivo* can result from two different perfusion rates or two different blood velocities. This study basically demonstrates that with an appropriate mathematical model, tumor vascular dynamics can be determined and monitored non-invasively while a perturbation of hyperoxic gas intervention is given. In such a way, non-invasive NIRS measurements may have useful and prognostic values to quantify the therapeutic effects of cancer treatments.

## 1. Introduction

Solid tumors are known to exhibit heterogeneous blood flow distribution,<sup>1,2</sup> and various methods have been used to study tumor perfusion heterogeneity, such as Doppler ultrasound,<sup>3</sup> dynamic contrast MRI,<sup>4</sup> diffuse correlation spectroscopy,<sup>5</sup> and the use of tumors grown in window chambers.<sup>6</sup> Intensive studies using <sup>19</sup>F Magnetic Resonance FREDOM (Fluorocarbon Relaxometry using Echo planar imaging for Dynamic Oxygen Mapping) by Mason *et al* have revealed intratumoral heterogeneities of tumor pO<sub>2</sub> and their heterogeneous responses to hyperoxic gas breathing.<sup>7,8,9</sup> The severe pO<sub>2</sub> heterogeneity in tumors can be attributed to the heterogeneous distribution of blood flow since tissue pO<sub>2</sub> level is determined by a balance between the supply of oxygen from blood vessels and the oxygen consumption rate of tissue cells.<sup>10</sup> Unlike FREDOM, near-infrared spectroscopy (NIRS) techniques measure hemoglobin oxygenation and concentration *in vivo*, providing possible quantification and monitoring of vascular oxygenation *in vivo* of the measured sample/organ non-invasively. This is why in recent years, NIRS has been widely utilized to investigate hemoglobin oxygenations of muscles,<sup>11,12,13</sup> the brain,<sup>14,15,16</sup> and animal tumors.<sup>17,18,19</sup>

The heterogeneity of blood perfusion in tumors also results in the developing regions of hypoxia during tumor growth. It is well known that in comparison to well oxygenated tumor cells, hypoxic cells in tumor are known to be highly resistant to radiation therapy.<sup>20,21</sup> Some forms of chemotherapy<sup>22</sup> and photodynamic therapy<sup>23</sup>. A number of clinical studies have shown that the tumor oxygenation level affects greatly the survival probability of cancer patients, as measured either by tumor regression or by local control.<sup>24</sup> Therefore, tumor oxygenation needs to be increased during therapy to improve the efficacy of cancer treatments. Breathing a

hyperoxic gas, such as carbogen (95% O<sub>2</sub> and 5% CO<sub>2</sub>) or 100% oxygen, has been used to enhance the cancer treatment as a mean of improving tumor oxygenation.<sup>25,26</sup> However, oxygen delivery from blood vessels to tumor cells in the hypoxic region can be prohibited by the poor vascular perfusion in tumors. Thus, measurements of local vascular oxygenation and perfusion in tumors can be important for tumor treatment planning and to evaluate methods designed to modulate tumor oxygenation.

In our previous studies, we have demonstrated that improvement of tumor vascular oxygenation during hyperoxic gas intervention could be monitored by NIRS.<sup>19,27,28</sup> A bi-phasic feature that has a rapid increase, followed by a gradual but significant increase, in response to carbogen intervention was observed from the changes of oxyhemoglobin concentration ( $\Delta[\text{HbO}_2]$ ) in tumor vasculature (Figure 1)<sup>28</sup>. We established a mathematical model based on Kety's approach<sup>29</sup> to explain this biphasic behavior of tumor hemodynamics in our earlier publication<sup>19</sup>. In that study, we formed a hypothesis that tumor vasculature was comprised of a well-perfused and poorly perfused region that could be detected with the two time constants through  $\Delta[\text{HbO}_2]$  readings derived from the NIRS. The mathematical model basically allowed us to associate the bi-phasic  $\Delta[\text{HbO}_2]$  amplitudes and time constants with the ratio of vascular coefficients and vascular perfusion rates in the two different regions.<sup>19</sup>

Even though the developed mathematical model was useful for interpretation of tumor hemodynamics and physiological parameters, it was lack of any proof or confirmation at the time. To provide solid support for this model and to further investigate heterogeneities of tumor vasculature, we have developed dynamic tumor vascular phantoms and have performed three-channel NIRS experiments on the dynamic phantoms. In this paper, we will report 1) our design and implementation for the dynamic vascular phantoms, 2) the experimental setup and

measurements for the NIRS readings from the dynamic phantoms, 3) the relationship between the NIRS time constants and flow velocities passing through the phantoms, and 4) the evidence to support our mathematical model. The results from this study show clearly that the two time constants observed in tumor oxygenation dynamics *in vivo* can result from two different perfusion rates or two different blood velocities. We conclude that with our bi-phasic mathematical model, tumor vascular dynamics can be determined and monitored non-invasively using NIRS while a perturbation of hyperoxic gas intervention is given.

## 2. Materials and Methods

### A. Review of the Our Mathematical Model of Tumor Vascular Oxygenation

In 1951, Kety developed a model to quantify regional cerebral blood flow (rCBF) with diffusible radiotracers.<sup>29</sup> In our previous report,<sup>19</sup> we have developed a mathematical model by following Kety's approach. We give a brief review here: by applying Fick's principle and defining  $\gamma$  as the ratio of  $\Delta[\text{HbO}_2]$  in the vascular bed to that in veins,  $\Delta[\text{HbO}_2]$  that was induced by hyperoxic gas intervention in tumor vasculature could be mathematically modeled as Eq. (1):

$$\Delta[\text{HbO}_2]^{\text{vasculature}}(t) = \gamma H_o [1 - \exp(-ft/\gamma)] = A [1 - \exp(-t/\tau)], \quad (1)$$

where  $\gamma$  was defined as the vasculature coefficient of the tumor ( $=\Delta[\text{HbO}_2]^{\text{vasculature}}/\Delta[\text{HbO}_2]^{\text{vein}}$ ),  $H_o$  was the arterial oxygenation input,  $f$  represented the blood perfusion rate,  $\tau$  is the time constant,  $A=\gamma H_o$ , and  $\tau=\gamma/f$ . Our measured signal,  $\Delta\text{HbO}_2^{\text{vasculature}}(t)$ , is the change of  $[\text{HbO}_2]$  in vasculature within the light interrogated tissue volume per unit time, and perfusion rate,  $f$ , is defined as the rate of total blood flow per a unit mass or volume of tissue/organ which has a unit

of ml/min/100g or ml/min/cm<sup>3</sup> while blood flow rate is the rate of blood flow within the blood vessels (ml/min).

If a tumor has two distinct perfusion regions, and the measured NIRS signals result from both regions (Figure 2), then it is reasonable to include two different blood perfusion rates,  $f_1$  and  $f_2$ , and two different vasculature coefficients,  $\gamma_1$  and  $\gamma_2$ , in the model. Eq. (1) then becomes Eq. (2) to count for the double exponential feature observed in the NIRS experiments:

$$\begin{aligned}\Delta\text{HbO}_2^{\text{vasculature}}(t) &= \gamma_1\text{H}_0[1-\exp(-f_1t/\gamma_1)] + \gamma_2\text{H}_0[1-\exp(-f_2t/\gamma_2)] \\ &= A_1[1-\exp(-t/\tau_1)] + A_2[1-\exp(-t/\tau_2)]\end{aligned}\quad (2)$$

where  $f_1$  and  $\gamma_1$  are the blood perfusion rate and vasculature coefficient in the well perfused region, respectively;  $f_2$  and  $\gamma_2$  represent the same respective meanings for the poorly perfused region, and  $A_1 = \gamma_1\text{H}_0$ ,  $A_2 = \gamma_2\text{H}_0$ ,  $\tau_1 = \gamma_1/f_1$ ,  $\tau_2 = \gamma_2/f_2$ . Since  $A_1$ ,  $A_2$ ,  $\tau_1$ , and  $\tau_2$  can be determined by fitting Eq. (2) with  $\Delta[\text{HbO}_2]$  readings taken from the NIRS measurements, we can obtain the ratios of two vasculature coefficients and the two blood perfusion rates as:

$$\frac{\gamma_1}{\gamma_2} = \frac{A_1}{A_2}; \quad \frac{f_1}{f_2} = \frac{A_1/\tau_1}{A_2/\tau_2}.\quad (3)$$

With these two ratios, we are able to understand more about tumor vascular structures and blood perfusion rates. In this paper, we report our experimental evidence to support the tumor hemodynamics model by quantifying  $\gamma_1/\gamma_2$  and  $f_1/f_2$  from three different locations of the tumor dynamic phantoms with the use of three-channel NIRS.

## B. Design and Implementation of the Dynamic Tumor Vascular Phantom

To represent two different perfusion regions in tumors, we designed a vascular mimic device (VMD) by winding a small diameter tube around a big diameter core tube, as shown in Figure 3. VMD-1 was fabricated by wrapping ethyl vinyl acetate microbore tubing (0.51 mm ID) around a tygon lab tube (14.4 mm OD), and VMD-2 was fabricated by winding polyethylene tubing (0.86 mm ID) around another piece of tygon lab tube (14.4 mm OD) to represent two kinds of vasculature with small (0.51 mm ID) and large (0.86 mm ID) diameters of blood vessels, respectively. All tubing materials were purchased from Cole-Parmer Company (Vernon Hills, IL).

The dynamic tumor vascular phantom was fabricated by embedding the two VMDs into a cylindrical soft gelatin, which represented non-vascular tissues. Specifically, the tissue mimic gelatin was prepared by mixing 50 g of gelatin powder (Sigma, Gelatin Type A, St. Louis, MO) with 350 ml of boiling water, and the solution was stirred thoroughly until the gelatin powder was dissolved completely. When the solution was cooled down to around 50 °C, 200 ml of 20% Intralipid solution (Intralipid® 20%, Baxter Healthcare Corp., Deerfield, IL) was added and mixed thoroughly to simulate light scattering in tumor tissues. Just when the solution started to be solidified, it was poured into a cylindrical container (diameter=4.5 cm, height=3.5 cm), containing the two VMDs and also into a box-shaped container (length=15 cm, width=15 cm, and height= 5 cm). After completely being cooled down, the solution became a soft gelatin phantom with the two VMDs embedded inside. The optical properties of gelatin phantoms were measured from the gelatin phantom in the box-shaped container using an NIR tissue oximeter (model: 96208, ISS Inc., Champaign, IL), and those values were close to tissue optical properties with  $\mu_a = 0.032 \text{ cm}^{-1}$  and  $\mu_s' = 9.2 \text{ cm}^{-1}$  at 750 nm.

Two kinds of dynamic tumor vascular phantoms were fabricated: Phantom 1 contained one VMD-1 and one VMD-2, while phantom 2 had two of VMD-1s. A stream of diluted black ink solution with  $\mu_a=1.5 \text{ cm}^{-1}$  at 730 nm (measured by a regular spectrophotometer) was used to go through the VMDs to simulate a blood flow through tumor vasculature. By pumping the ink solution through VMD-1 and VMD-2 with the same flow rate in phantom 1, we could simulate the effects of different sizes of blood vessels on the bi-phasic behavior of changes in NIRS signals. In the meanwhile, by injecting the ink solution through the two VMD-1s in phantom 2 with two different flow rates, we would be able to associate the bi-phasic feature of NIRS with the flow rate. In this way, we could mimic the dynamic fluid dependence of a breast tumor, with a hyperoxic gas inhalation, on different sizes of blood vessels and on different perfusion rates.

### C. Multi-Channel NIR Spectroscopy

We used a multi-channel, continuous wave, NIRS system with one light source at 730 nm and three detectors to monitor light absorption changes from the dynamic tumor vascular phantoms in this study. Based on the modified Beer-Lambert's law<sup>30</sup>, the data presented in this paper were analyzed using the measured amplitudes to quantify changes in optical density (O.D.) induced by absorber concentration changes (Eq. 4).

$$\Delta O.D = O.D._T - O.D._B = \log(I_B/I_T) / L, \quad (4)$$

where  $L$  is the optical path length between the source and detector, and  $I_B$  and  $I_T$  are baseline and transient amplitudes of the measured optical signals, respectively. It is known that  $L$  is in proportion to the source and detector separation,  $d$ , with a factor of  $DPF$  (Differential Pathlength Factor)<sup>19,31</sup>, i.e.,  $L=d*DPF$ . In principle, the  $DPF$  factor depends on both the absorption and reduced scattering coefficients,  $\mu_a$  and  $\mu_s'$ , respectively.<sup>32</sup> Although a  $DPF$  value of 2.5 for

tumors has been used by others<sup>33</sup>, little is known about  $DPF$  for solid tumors because of its finite size and high heterogeneity. Thus, in common with our recent approaches<sup>34,35</sup>, we included the  $DPF$  factor within the unit as  $\text{cm}^{-1}/DPF$  for  $\Delta O.D.$  in the relative measurements since our focus is on the dynamic features. Equation (4) then becomes Eq. (5), permitting us to quantify  $\Delta O.D.$  in the dynamic phantom measurements.

$$\Delta O.D = O.D._T - O.D._B = \log (I_B/I_T) / d. \quad (5)$$

Equation (5) was repeatedly utilized for each of the three channels for individual data analysis.

#### **D. Experimental Setup and Procedures of Dynamic Phantom Measurements**

The schematic experimental setup for dynamic phantom measurements is shown in Figure 4(a). Near infrared light at 730 nm was delivered from a multi-channel NIRS system to the dynamic tumor vascular phantom, and three optical detectors were placed on the side of the cylindrical phantom to collect the NIR signals at three different locations. A diluted ink solution was injected into the VMDs using 5 ml B-D™ disposable syringes (Cole-Parmer, Vernon Hills, IL) by two syringe infusion pumps (model KDS200, KdScientific Inc., New Hope, PA), and the ink wastes were collected in a waste beaker. We used two separate syringe infusion pumps so that we could control the flow rate of each VMD independently. Figure 4(b) shows the close-up geometry of light source and three optical detectors around dynamic phantom 1 with the two imbedded VMDs. The light source was placed between the two VMDs, and detector D3 was located across the light source in transmission mode so that it would detect the signal passing through both VMDs. Other two detectors (D1 and D2) were placed in the semi-reflectance geometry with respect to the light source so that D1 and D2 would get the NIR signals mostly

from only VMD-1 or VMD-2, respectively. The setup was the same for dynamic phantom 2, containing two VMD-1s instead of one VMD-1 and one VMD-2.

In phantom 1 measurement, VMD-1 and VMD-2 were initially filled with water to obtain the NIR baseline readings. Next, the ink solution was injected into VMD-2 first with a flow rate of 20 ml/hr to simulate the dynamic process of blood flow, followed by a washout with water. As the third step, the dynamic procedure was repeated with the ink solution injected into VMD-1 with the same flow rate. Lastly, the measurement was reproduced while the ink solution was infused simultaneously into both VMD-1 and VMD-2 with the same flow rate (20 ml/hr). The last step was planned to observe a bi-phasic increase in light absorption, which is expected due to two different perfusion velocities through VMD-1 and VMD-2 having two tube diameters, while the applied solution flow rates in both VMDs kept the same. The relationship between the ink flow velocity,  $v$  (cm/sec), and ink flow rate,  $Q$  (cm<sup>3</sup>/sec), is given as

$$Q = V/t = S \times v = \pi r^2 \times v, \quad (6)$$

where  $V$  and  $S$  are the volume and cross-section area of a tube, respectively, and  $r$  is the inner radius of simulated blood vessel or tube. Equation (2) shows clearly that  $v$  will be different for two vessels or tubes with different sizes if they have the same flow rate,  $Q$ . In phantom 2 measurement, the same dynamic protocols were used to fill the two identical VMD-1s separately and simultaneously for the dynamic NIRS readings, with the same flow rate (20 ml/hr) followed by a washout of water. In addition, the ink solution was injected into the two VMD-1s with two different flow rates, i.e., 5 and 20 ml/hr for the top and bottom VMD-1, respectively, and water was used to wash out VMD-1s.

For both of the phantom experiments, the changes in NIR light intensity were measured through the whole experiment. The time constants during the dynamic changes were obtained by fitting the data with Eqs. (1) or (2) using Kaleidagraph (Synergy Software, Reading, PA)

### 3. Results

#### A. NIR Measurements Taken from Dynamic Tumor Vascular Phantom 1

To observe the correlation between the flow rate and time constant, we have utilized a range from 1 to 60 ml/hr and measured optical density changes ( $\Delta O.D.$ ) from the dynamic tumor vascular phantoms with the source and detector located at S and D3, respectively (Fig. 4b). The actual  $\Delta O.D.$  values were calculated based on Eq. (5), and a set of temporal  $\Delta O.D.$  data are shown in Fig. 5(a). The optical density changes with flow rates from 15 to 60 ml/hr are shown in Fig. 5(b) separately since they are too close to the curve with 10 ml/hr. These figures clearly show that the detected change in light absorption occurs faster with a high flow rate, exhibiting a smaller time constant obtained with a single-exponential curve fitting using Eq. (1). Figure 6(a) plots the relationship between the time constants and flow rates of the ink solution using both the linear (bottom and left axis) and logarithmic scale (top and right axis). It is seen here that the time constant rapidly drops as the flow rate increases, and a strong exponential correlation between them ( $R=0.99$ ), as given in Eq. (10), is confirmed by the straight line in the logarithmic plot.

$$\tau = 419.71 Q^{-1.13}, \quad (10)$$

where  $Q$  is in  $\text{cm}^3/\text{sec}$ , and  $\tau$  is in sec.

On the one hand, the velocity of ink solution at each flow rate can be quantified by dividing the large tube length (25 mm, see Fig. 3) by the duration of time when the ink solution

inside the small tube entered the phantom at one end and came out at the other. We recorded this temporal duration using a stop watch for each measurement. In this way, we have calculated the velocities of ink solutions and plotted them in Fig. 6(b). On the other hand, given the flow rate and diameters of the small wrapping tubes used for VMDs inside the phantom, the velocity of ink solution flow can be calculated by using Eq. (6) (i.e.,  $v = Q / (\pi r^2)$ ). For example, velocity of ink flow at 10ml/hr flow rate can be obtained as follows. Since the radius of small tube is 0.255 mm, the area of tube cross section is  $0.2043 \text{ mm}^2 (= \pi * 0.255^2)$ . The flow rate of 10ml/hr is equal to  $2.78 \text{ mm}^3/\text{sec}$  after converting the unit of time from hour to second and also after converting the unit of volume from ml to  $\text{mm}^3$ . Then, the velocity of ink solution flowing inside the small tube results in  $13.6 \text{ mm}/\text{sec} (= 2.78 \text{ mm}^3 \cdot \text{sec}^{-1} / 0.2043 \text{ mm}^2)$ . However, D3 detector measured optical signal changes from the dynamic phantom while the ink solution flowed spirally along the large tube. Therefore, the calculated velocity of ink flow seen by the NIRS needs to be converted to a longitudinal velocity along the big tube (25 mm, see Fig. 3). Given the total length of the wrapped small tube, which was 750 mm, we obtained a factor of 30 ( $= 750 \text{ mm} / 25 \text{ mm} = \text{the length of small tube wrapping around the large tube} / \text{large tube length}$ ). With this conversion factor, we arrived at  $0.453 \text{ mm}/\text{sec} (= 13.6 \text{ mm} \cdot \text{sec}^{-1} / 30)$  as a final calculated velocity for the 10 ml/hr flow rate with the 0.51-mm-diameter tube. Figure 6(b) shows the consistency between the calculated and measured velocities using the two different approaches. It also exhibits a strong correlation between the flow rate and the velocity of ink solution measured from the dynamic tumor vascular phantom ( $R=0.99$ ). It is worthy to point out that these ink flow velocities shown are within the biological range of velocities of red blood cells (i.e., 1~20 mm/sec in arterioles and 1~8 mm/sec in venules from normal mice<sup>36</sup>).

Figure 7(a) shows the optical density changes ( $\Delta O.D.$  at 730 nm) at three different positions taken from dynamic tumor vascular phantom 1 when the ink solution was injected into the VMDs. The first step in this experiment was injecting the diluted ink into only VMD-2, having a large diameter tube (0.86 mm ID) with a flow rate of 20 ml/hr. As seen in this figure, the readings from D2 and D1 show the largest and smallest increase in  $\Delta\mu_a$ , respectively, since the changes of O.D. in VMD-2 would be detected most sensitively by D2 and least sensitively by D1 (see Fig. 4(b)). The increase in  $\Delta O.D.$  obtained from D3 is between those from D1 and D2, as expected. A similar pattern is also displayed at step 2, when the diluted ink flowed only into VMD-1 (at 20 ml/hr) having a smaller diameter for the wrapping tube (0.51 mm ID). In this case, the readings at D1 offered the largest increase in  $\Delta O.D.$ , and D2 had a smallest  $\Delta O.D.$  increase (Fig. 4(b)), as expected. Steps 1 and 2 clearly illustrate that an NIRS detector collects optical signals more sensitively from an adjacent VMD than from a distant one. The third step in the measurement was to inject the solution into both VMD-1 and VMD-2 simultaneously with the same flow rate as before (20 ml/hr). At this step, we could observe two features: 1) the time profile taken at D1 had a faster transition time than that at D2, and 2) the time profile taken at D3 had a clear bi-phasic characteristic, very similar to those we often observed in our animal tumor dynamic measurements.<sup>19,27,28,34</sup>

To understand this set of results, we consider the ink flow velocities at each tube. Although the flow rate was kept the same in both VMDs ( $Q_{VMD-1} = Q_{VMD-2}$ ), the velocities of ink solutions in the two VMDs were different because of the different inner diameters of wrapping tubes. Since  $Q_{VMD-1} = Q_{VMD-2}$ , Eq. (6) leads to Eq. (10) with  $r_{VMD-1} = 0.255$  mm and  $r_{VMD-2} = 0.43$  mm:

$$\frac{v_{VMD-1}}{v_{VMD-2}} = \frac{r_{VMD-2}^2}{r_{VMD-1}^2} = \frac{0.43^2}{0.255^2} = 2.84, \quad (11)$$

where  $v_{VMD-1}$ , and  $v_{VMD-2}$  are velocities of the ink solution in the VMD-1 (ID=0.51 mm) and VMD-2 (ID=0.86 mm), respectively, and  $r_{VMD-1}$ , and  $r_{VMD-2}$  present the radii of the VMD-1 and VMD-2, respectively. This velocity difference may be the reason why the transition time in VMD-1 seen by D1 (see Fig. 4) is faster than that in VMD-2 detected by D2. Furthermore, since D3 was in the transmission geometry and nearly equal distanced to both of the VMDs, the signal obtained at D3 may sense the dynamic changes in light absorption within both VMD-1 and VMD-2. We expect that the bi-phasic feature recorded by D3 results from a superposition of two different dynamic transitions at VMD-1 and VMD-2.

To confirm our expectation, the  $\Delta O.D.$  values detected from all three detectors at step 3 given in Fig. 7(a) were fitted with Eq. (2) to obtain amplitudes and time constants. The fitted values for each curve are listed in Table 1, and the corresponding curves are shown in Fig. 7(b). The results show that when the ink solution flows into both VMD-1 and VMD-2, the fast time constant ( $\tau_1=11.7 \pm 3.5$  sec) and slow time constant ( $\tau_2=35.2 \pm 7.3$  sec) observed at D3 are close to  $\tau_1 (=7.3 \pm 0.3$  sec) obtained from D1 near VMD-1 and  $\tau_1 (=42.8 \pm 1.5$  sec) obtained from D2 near VMD-2, respectively. The ratio between the fast and slow time constants, i.e.,  $\tau_1/\tau_2$ , is near 1/3 ( $\approx 11.7$  sec/35.2 sec), almost equal to the reciprocal ratio of  $\frac{v_{VMD-1}}{v_{VMD-2}} = 2.84$ . This can be

further expressed mathematically, using Eq. (6) and (10):

$$\frac{\tau_1}{\tau_2} = \left( \frac{419.7Q_1}{419.7Q_2} \right)^{-1.13} = \left( \frac{r_1^2 v_1}{Q_2} \right)^{-1.13}$$

Since the relationship between flow rate and velocity is expressed as a linear equation  $v=0.046*Q$  from Fig. 6(b), we can obtain the correlation between time constant and ink velocity by substituting the flow in Fig. 6(a) with velocity values as follows.

$$\begin{aligned}
 \tau_1 &= 419.71Q_1^{-1.13} \\
 &= 419.71 \cdot (21.74v_1)^{-1.13} \\
 &= 12.94 v_1^{-1.13}
 \end{aligned} \tag{11}$$

Therefore, if  $v_2$  is  $b$  times faster than  $v_1$ , then  $\tau_2$  will be

$$\begin{aligned}
 \tau_2 &= 12.94v_2^{-1.13} \\
 &= 12.94(b \cdot v_1)^{-1.13} \\
 &= b^{-1.13} \tau_1
 \end{aligned} \tag{12}$$

In this case, since  $v_{VMD-1}$  ( $v_2$ ) is 2.86 times faster than  $v_{VMD-2}$  ( $v_1$ ) intrinsically due to the differences in radius,  $\tau_{VMD-1}$  can be obtained by multiplying 0.31 ( $=2.86^{-1.13}$ ) to the value of  $\tau_{VMD-2}$  results in 10.9 sec ( $=0.31*35.2$ ) which is close to the measured value (11.7 sec). This indeed leads to several important conclusions: 1) the two-exponential behavior of tumor blood oxygenation during carbogen inhalation can be closely associated with two different sizes of blood vessels in tumors, 2) the bi-phasic time constants are closely associated with the blood flow velocities in tumors, independent of sizes of tumor blood vessels.

This clearly demonstrates that a fast flow can give rise to the fast transient component seen by the NIRS, and a slow flow component results from a slow flow

The data taken from Phantom 1 basically demonstrate that we can experimentally mimic the bi-phasic increase of  $\Delta[\text{HbO}_2]$  in tumor during carbogen inhalation by applying two different velocities from two different diameter VMDs. This knowledge may help us understand the bi-

phasic features observed in the breast tumor vascular oxygenation measurements under carbogen inhalation. Furthermore, the next phantom 2 experimental results demonstrate that the bi-exponential dynamics may also result from different flow rates, given the same diameters for the two VMDs.

### **B. NIR Measurements Taken from Dynamic Tumor Vascular Phantom 2**

Figure 8a shows the experimental results from tumor vascular dynamic phantom 2, and this phantom is different from phantom 1 by having two VMD-1s instead of one VMD-1 and one VMD-2 in tumor phantom 1. Since we now have two VMD-1s, the velocities of dye in VMDs will be totally depending on the ink flow rates controlled by two syringe pumps. The source and detector positions were same as the phantom 1 experiment, which is shown in detail in the Fig. 4b, and we observed the results similar to those shown in the Fig. 7a by alternating flow rates.

The first step for this experiment was injecting ink solution only into bottom VMD-1 with a flow rate of 20 ml/hr. As a result, D1 showed the largest increase of  $\Delta O.D.$  while D2 showed the least increase of  $\Delta O.D.$  because D2 was located quite away from the bottom VMD-1. For the second step, top VMD-1 was injected with ink at the same flow rate of 20 ml/hr. Here, D2 showed the largest increase of  $\Delta O.D.$  and D1 showed the smallest increase of  $\Delta O.D.$  In both of the above cases, the signals from D3 showed similar profiles as the others, without showing a clear bi-phasic feature. Then, as the third step, the ink was injected into both top and bottom VMD-1s with the same flow rate (20 ml/hr). Similarly, we did not observe any clear features of the two-exponential increase of  $\Delta O.D.$  from D3. For the fourth step, we injected a ink into both VMD-1s, but with two different flow rates: 5 ml/hr for the top VMD-1 and 20 ml/hr for the bottom VMD-1. Now we can see that bi-exponential behavior appears on D3 since D3 is detecting signals from both top and bottom VMD-1s, which have two different ink flow rates.

Once again, time constant analysis was performed for the increase of  $\Delta O.D.$  from three detectors at step 4 in Fig. 8(a) and is shown in Fig. 8(b). This time constant analysis shows that  $\Delta O.D.$  increases from D1 and D2 are well fitted by a mono exponential model while the  $\Delta O.D.$  increase from D3 is fitted better with a double exponential model. As we can see from the Table 2, which the values of fitted parameters are summarized, fast time constant ( $\tau_1 = 18.13 \pm 0.87$ ) and slow time constant ( $\tau_2 = 133.66 \pm 11.36$ ) from D3 are well matched with  $\tau_1$  in D1 ( $20.92 \pm 0.53$ ) and  $\tau_1$  in D2 ( $131.19 \pm 3.46$ ). This suggests that the dynamic signals obtained from D3 with a fast and a slow component indeed result from two different dye flow rates in VMD-1s. In addition, the values of  $A_1$  ( $0.068 \pm 0.0024$ ) and  $A_2$  ( $0.047 \pm 0.0018$ ) from D3 in step 4 are well matched to the values of  $A_1$  from D3 in step 1 ( $A_1 = 0.060 \pm 0.001$ ) and step 2 ( $A_1 = 0.043 \pm 0.001$ ). This indeed shows that the  $\Delta O.D.$  measured from D3 at step 4 is a summation of  $\Delta O.D.s$  from both VMD-1s.

#### 4. Discussion

Dynamic tumor vascular phantom experiments results supported our hypothesis that the bi-phasic tumor hemodynamic feature during carbogen inhalation results from a well-perfused and a poorly perfused region in the tumor vasculature. Through our phantom study, we were able to find that the main cause for having a bi-phasic behavior is coming from different blood flow rate, more precisely from different blood velocity in tumor. These differences in velocity can be from different blood vessel diameters with a same blood flow rate or from different blood flow rate with a same vessel diameter, which tumor vasculatures have both. Our mathematical model carries this information. Since  $\tau$  is equal to  $\gamma$  divided by  $f$ , the value of time constant is affected by both  $\gamma$  and  $f$  (Eq. 1). By assuming that  $f$  is constant, then  $\tau$  will be depending on the value of  $\gamma$ .

According to the definition of  $\gamma$ , it is a ratio of  $\Delta[\text{HbO}_2]$  in vasculature and  $\Delta[\text{HbO}_2]$  in vein. In our case,  $\Delta[\text{HbO}_2]$  in vasculature is limited to  $\Delta[\text{HbO}_2]$  in microvessels within a light interrogated tissue volume since our measurement is sensitive to the small size blood vessels rather than the large blood vessels including veins. Therefore,  $\Delta[\text{HbO}_2]_{\text{vasculature}}$  can be altered by the amount of  $\Delta[\text{HbO}_2]$  in microvessels which will be decided by the microvessel density and also by the diameter of microvessels when oxygen consumption rate and arterial input function,  $\Delta[\text{HbO}_2]_{\text{artery}}$ , are constants which were assumed in our mathematical model. This leads us to predict that the time constant value will be increased when there is a large volume of  $\Delta[\text{HbO}_2]_{\text{ink}}$  by having more microvessels/tubes within the light interrogated tissue/phantom volume or by having a larger diameter microvessels/tubes in tissue/phantom which was confirmed by our phantom 1 experiment. In other case,  $\tau$  will be depending on the value of  $f$  by assuming  $\gamma$  is constant. Perfusion rate,  $f$ , will be linearly increased to the increase of blood/ink flow rate when the microvessel/tube density and the diameter of microvessel/tube are fixed. Therefore,  $\tau$  will become small when flow rate of blood/ink increases which is shown by phantom 2 experiment.

Tumor blood vessels are known to be very leaky, longer in vessel lengths, larger in vessel diameter, and also their local microvessel density is much more heterogeneous compare to normal tissues.<sup>1</sup> In addition, solid tumors usually develop hypoxia, which can be from poor perfusion in the central region when they grow bigger. Meanwhile, the peripheral region of tumor is normally well perfused so that it can be well provided with nutrition and oxygen. Therefore, tumor vasculature can be a mixed structure between well-perfused region and poorly perfused region, which can be observed as a bi-phasic feature of hemodynamics with respiratory challenges. The multi-channel NIRS system will allow us to study the dynamic heterogeneity at

different locations, showing that the tumor vasculature in the poorly perfused region (with a lower perfusion rate) can be eventually oxygenated if the two dynamic components are observed. On the other hand, if only the fast component can be found during the tumor blood oxygenation from a hyperoxic gas intervention (mono exponential model), it suggests that the poorly perfused region in the tumor is not going to be improved for its vascular oxygenation under respiratory intervention.

As we described in the materials and methods section earlier,  $\gamma_1/\gamma_2$  may be associated with the vascular volume or density of two regions, and  $f_1/f_2$  is related to the ratio of blood perfusion rates between region 1 and 2. Our dynamic tumor vascular phantom experiments showed that  $A$  or  $\gamma$  values are related with the amount of absorption changes of VMDs in tumor phantoms, and  $\tau$  values are related to the velocity of dye flow. The intensity of absorption changes that measured from detectors depends on the absorption coefficient of dye, the tube length or diameter in VMD, the wrapping number of small tubing around big tubing, and the location of detectors. Time constant is mainly depending on a dye flow velocity which is affected by both  $\gamma$  and perfusion rate as described earlier in this section. For a tumor experiment, the  $\mu_a$  of dye during phantom experiments corresponds to the level of blood oxygenation, and the VMDs in phantoms can be thought as a blood vessel network. The number of winding small tubing around big tubing can be thought as a vascular density in tumor, which will affect the values of both  $\gamma$  and  $f$ .

To compare the results from tumor vascular dynamic phantom experiments with our previous FEM simulation results,<sup>37</sup> we divided  $\Delta O.D.$  by maximum value of  $\Delta O.D.$  from each detector for normalization. (Figure 9a and 9b) Figure 9a is a normalized plot of step 4 in Fig. 8a (dynamic tumor vascular phantom experiment) and Fig. 9b is another normalized plot of Fig.

$5(c2)^{37}$  in our previous study (FEM simulation). These figures show how much FEM simulation results are close to tumor vascular dynamic phantom experiments. Both of them show that  $\Delta O.D.$  increases from D3 and (0,2) position can be well fitted by using our double exponential model. The early time of  $\Delta O.D.$  increases from D3 and (0,2) position (inside the circle) have larger  $\Delta O.D.s$  than D1, D2, (-2,0) and (2,0), which can be explained by locations of detectors. Since the ink flow started from D3 or (0,2) side, both D3 and (0,2) position could detect  $\Delta O.D.$  changes earlier than those from the other detectors (D1, D2, (-2,0), and (2,0)), which were located a little far from the ink flow starting position. These results indeed show that FEM simulation can well explain the results from tumor phantom experiments by using a light diffusion equation.

Our previous measurements of animal tumors were performed in a transmittance mode by one channel NIRS, which could obtain only a global measurement of tumor hemodynamics. Therefore, those results could not show intratumoral or intertumoral vascular heterogeneities. However, multi-channel NIRS, by comparing  $\gamma_1/\gamma_2$  and  $f_1/f_2$  among the signals taken at different locations from the same tumor or from different tumors, will enable us to study intratumoral or intertumoral heterogeneity. Since tumor vascular structure will be modified during therapies, we will be able to observe the changes of  $\gamma_1/\gamma_2$  and  $f_1/f_2$  through time by giving respiratory challenges such as carbogen or pure oxygen inhalation. Therefore, multi-channel NIRS or imaging not only can detect vascular heterogeneity of tumor but also can be a prognostic tool for monitoring the early effects of tumor treatments such as radiotherapy, photodynamic therapy, or chemotherapy. The detection of early effects of cancer therapies will benefit patients to have a higher survival rate by treating the patients with proper therapies.

## 5. Conclusion

We developed tumor vascular dynamic phantom models to demonstrate our hypothesis on tumor hemodynamics during hyperoxic gases inhalation. We believe that bi-phasic feature of tumor blood oxygenation increases during carbogen/oxygen inhalation is from tumors' distinct vascular structure, which is composed of well-perfused region and poorly perfused region. Our tumor phantom experiments were performed to find what can cause tumor hemodynamics to have two time constants when it is fitted with our mathematical model. We found that two time constants in tumor hemodynamic models can be from different blood flow velocities or anything that can cause changes in blood flow velocities such as a blood vessel diameter, and the geometry of blood vessel network. In addition, we also found that two different amplitudes in tumor hemodynamic models are from two different absorptions in two regions, which are possibly due to different blood oxygenation level (oxyhemoglobin concentration), or vascular density.

NIRS is a portable, low cost, and real time measurement system that can monitor changes of vascular oxygen levels in tissues by using two wavelengths. We have previously used a single-channel NIRS system with one light source and one detector for global measurements of  $\Delta[\text{HbO}_2]$  and  $\Delta[\text{Hb}_{\text{total}}]$  in tumors during respiratory challenges.<sup>19</sup> Now, this study demonstrates that the NIRS multi-channel approach has the great potential to detect and monitor tumor heterogeneity under therapeutic or adjuvant interventions. In the future we propose 1) to further investigate and understand the meaning of vasculature coefficient,  $\gamma$ , and 2) to develop an NIR imaging system to be used as a monitoring tool for the efficacy of cancer therapy.

## **ACKNOWLEDGEMENTS**

This work was supported in part by the Department of Defense Breast Cancer Research grants DAMD17-03-1-0353 (JGK) and DAMD17-00-1-0459 (HL) as well as by the National Institutes of Health 1R21CA101098-01 (HL). The authors acknowledge the support of the multi-channel NIRS system from Dr. Britton Chance at the University of Pennsylvania, Philadelphia as well as to Dr. Kevin Nelson for the support of syringe pumps.

Table 1. Summary of fitted parameters obtained at the three detectors in Figure 6b.

Parameters	Mono-Exponential fitting $\Delta\text{HbO}_2 = A_1[1-\exp(-t/\tau_1)]$		Double-Exponential fitting $\Delta\text{HbO}_2 = A_1[1-\exp(-t/\tau_1)] + A_2[1-\exp(-t/\tau_2)]$
	Detector D2 (near VMD 2 with 0.51 mm diameter)	Detector D1 (near VMD 1 with 0.86 mm diameter)	Detector D3 (equal distanced between VMD 1 and VMD 2)
$A_1$ (mM/DPF)	$0.49 \pm 0.007$	$0.34 \pm 0.001$	$0.092 \pm 0.041$
$\tau_1$ (min)	$42.8 \pm 1.53$	$7.3 \pm 0.25$	$11.71 \pm 3.49$
$A_2$ (mM/DPF)			$0.18 \pm 0.038$
$\tau_2$ (min)			$35.17 \pm 7.25$
$\chi^2$	0.039	0.016	0.0018
R	0.99	0.98	0.99

Table 2. Summary of fitted parameters obtained at the three detectors in the Fig. 7b.

Parameters	Mono-Exponential fitting $\Delta\text{HbO}_2 = A_1[1-\exp(-t/\tau_1)]$		Double-Exponential fitting $\Delta\text{HbO}_2 = A_1[1-\exp(-t/\tau_1)] + A_2[1-\exp(-t/\tau_2)]$
	Detector D2	Detector D1	Detector D3
$A_1$ (mM/DPF)	$0.26 \pm 0.003$	$0.17 \pm 0.001$	$0.068 \pm 0.0024$
$\tau_1$ (min)	$131.19 \pm 3.46$	$20.92 \pm 0.53$	$18.13 \pm 0.87$
$A_2$ (mM/DPF)			$0.047 \pm 0.0018$
$\tau_2$ (min)			$133.66 \pm 11.36$
$\chi^2$	0.057	0.019	0.0018
R	0.98	0.97	0.99

## Figure captions

Figure 1. Normalized hemodynamic changes of tumor blood oxygenation,  $\Delta[\text{HbO}_2]$ , obtained with the NIRS measurement from a rat breast tumor while the breathing gas was switched from air to carbogen. (Yueqing *et al.* Applied Optics, 2003)[28]

Figure 2. A schematic diagram of light transmitting patterns in tumor when tumor has two distinct perfusion regions. Center of tumor represents poorly perfused region and peripheral region of tumor with gray color is representing a well-perfused region. Since the light transmitting volume is different in each detector, each detector will show the different fitted parameters.

Figure 3. A schematic diagram for one vascular modeling device (VMD). Two different inner diameter (I.D.) sizes of tubing have been used to wind outside of core tubing to simulate different blood vessel diameters within a breast tumor.

Figure 4. A experimental setup for the tumor dynamic phantom study. (a) Two syringe pumps were connected to two VMDs in tumor vascular dynamic phantom individually to have different dye flow rates for each VMD. Light was transmitted from light source through tumor vascular dynamic phantom and was collected at three different detectors for data processing in computer, (b) Enlarged tumor vascular dynamic phantom embedded with two VMDs. Tumor phantom 1 has VMD-1 and VMD-2 as shown here, and tumor phantom 2 has two VMD-1s.

Figure 5. (a) Absorption changes measured from the dynamic tumor vascular phantom with increasing a flow rate from 1 to 30 ml/hr. The symbols and curves are obtained from the phantom experiments and from one-exponential curve fitting, respectively. (b) A correlation between time constants and flow rates plotted with the linear scale (left and bottom axis) and logarithmic scale (top and right axis).

Figure 6. (a) A temporal profiles of 3-channel NIRS measurements results from D1, D2, and D3 on a tumor dynamic phantom 1 that has two different sizes of VMDs (VMD-1 and VMD-2). Three traces represent the readings at D3 (in transmission mode and located between the two VMDs), D1 (near the VMD-2), and D2 (near the VMD-1). (b) Absorption changes obtained from D1, D2, and D3 during step 3 at Fig. 7a. Open symbols represent the raw data of absorption changes and solid lines are either mono-exponential model fitting curve (D1 and D2) or bi-exponential model fitting curve (D3).

Figure 7. (a) 3-channel NIRS results measured on a tumor dynamic phantom 2 that has two VMD-1s. Three traces represent the readings at D3 (in transmission mode and located between the two VMDs), D1 (near the top VMD-1), and D2 (near the bottom VMD-1). (b) Temporal profiles of the NIRS measurements from D1, D2, and D3 with mono-exponential model fitting curves (D1, and D2) and bi-exponential model fitting curve (D3).

Figure 8. Normalized  $\Delta\mu_a$  plots are shown to compare the results between a tumor vascular dynamic phantom experiment and a FEM simulation: (a) Normalized  $\Delta\mu_a$  plots of step 4 in Fig. 8a, (b) Normalized  $\Delta\mu_a$  plots of Fig. 10c.

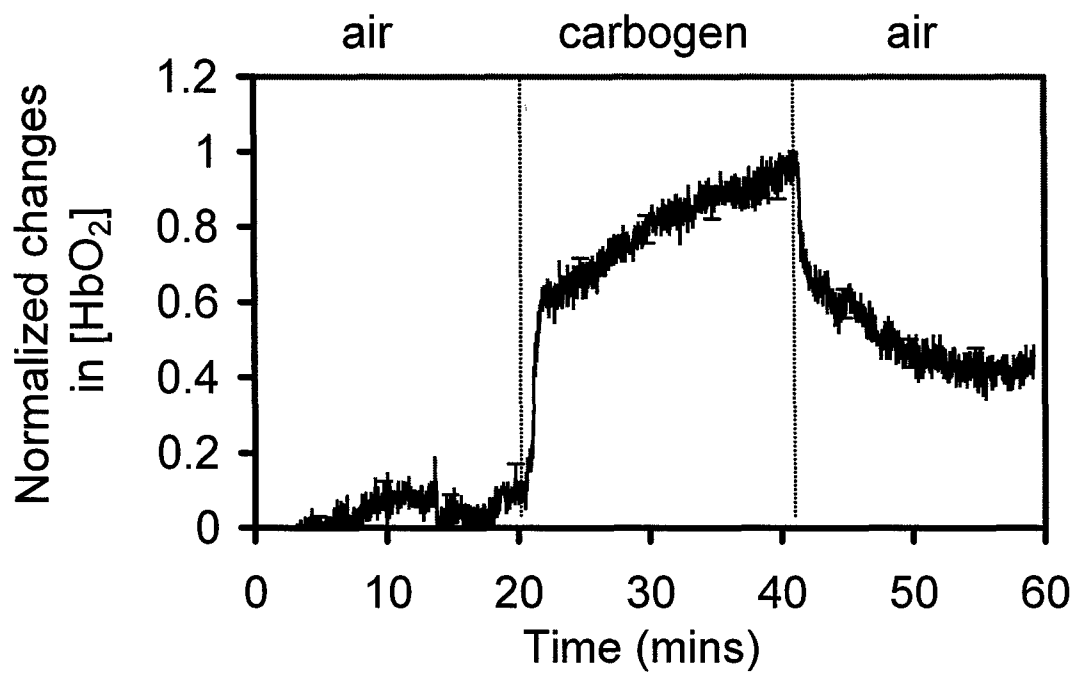


Figure 1

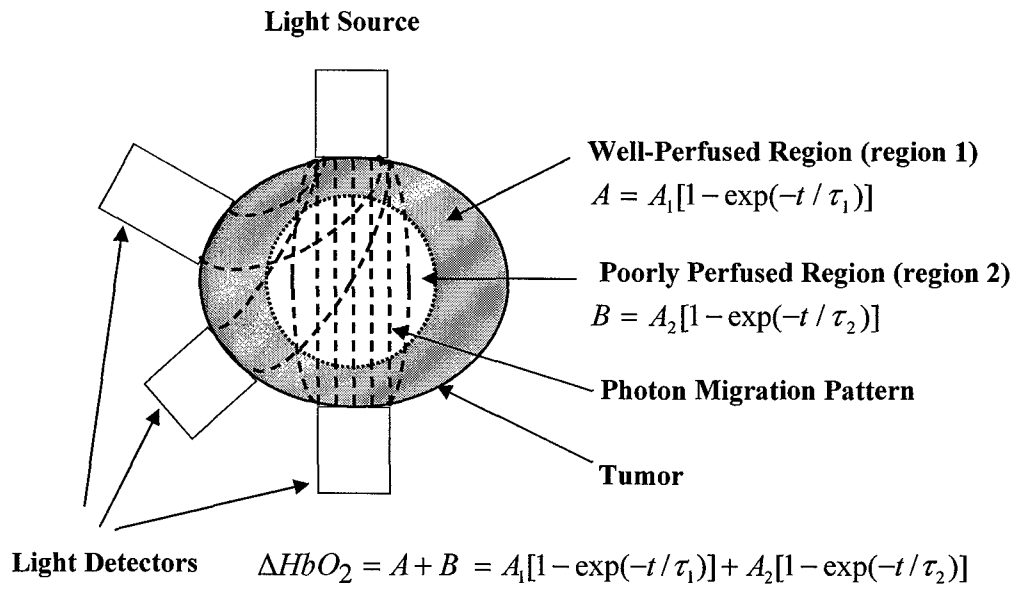


Figure 2

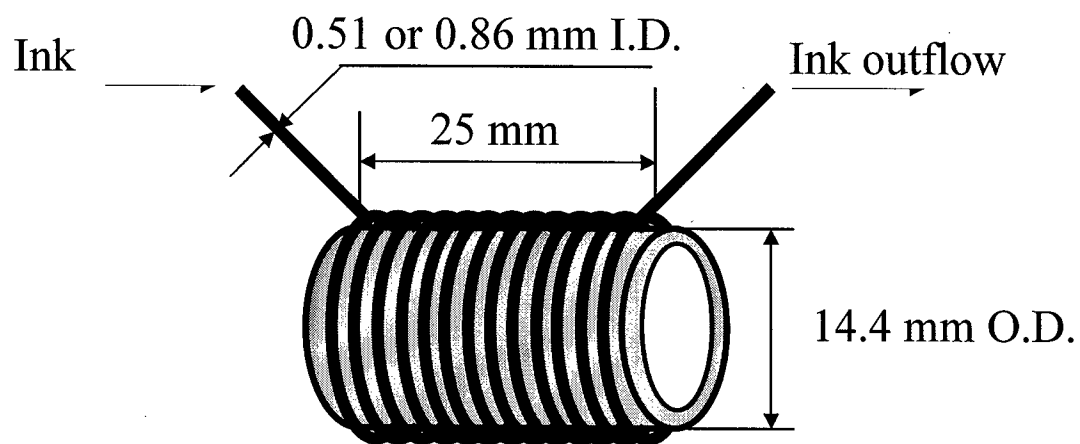


Figure 3

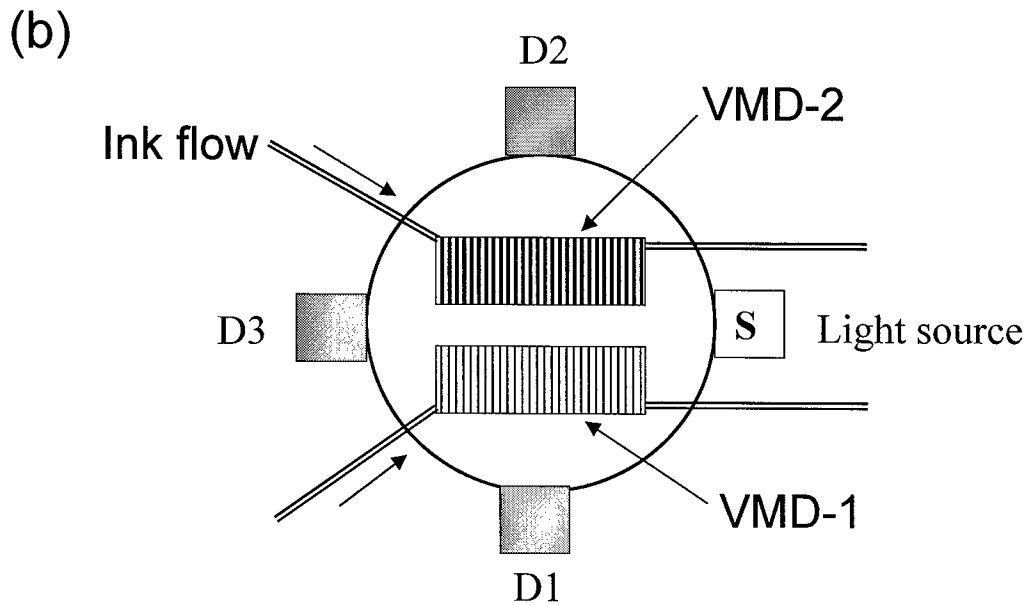
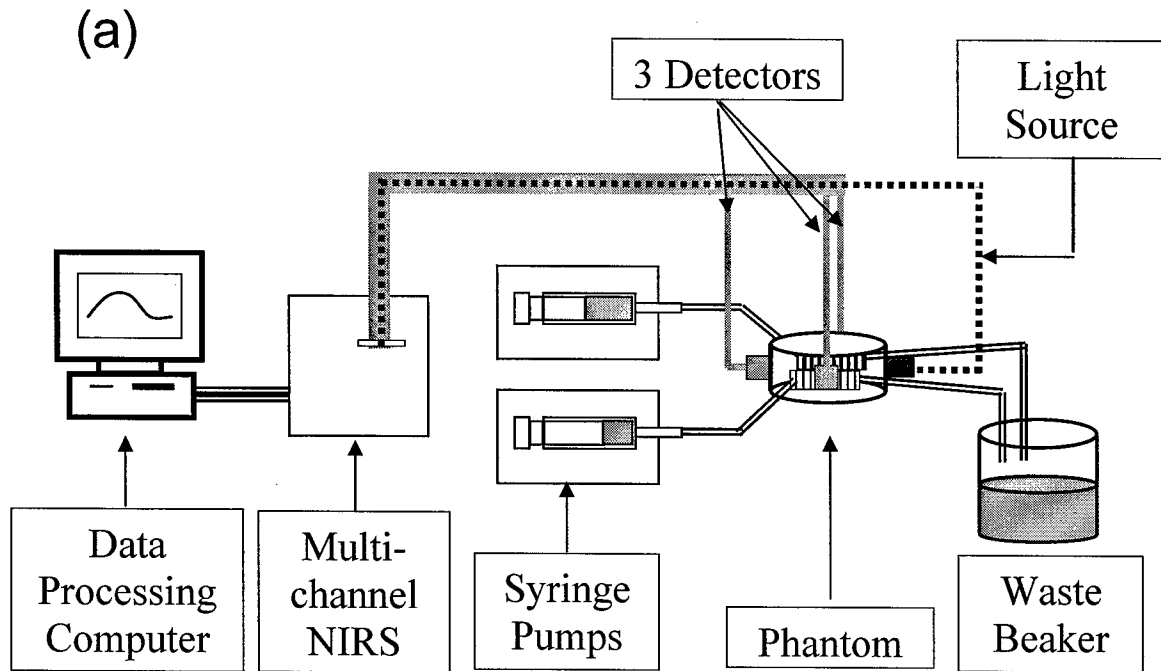


Figure 4

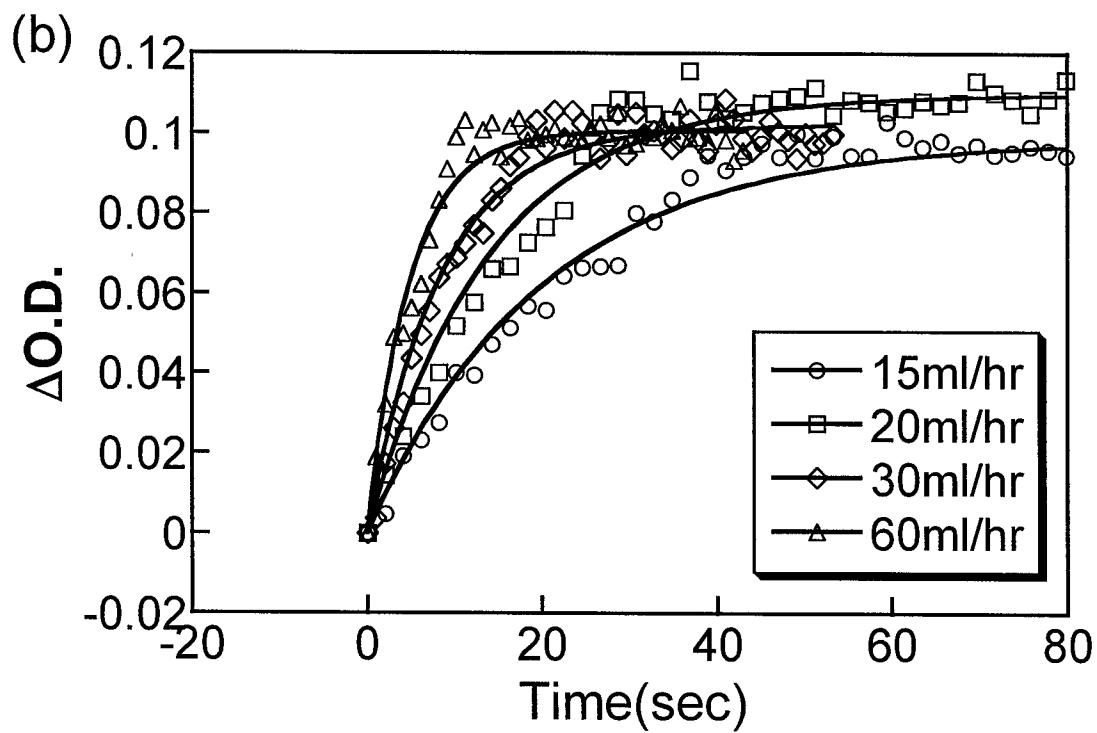
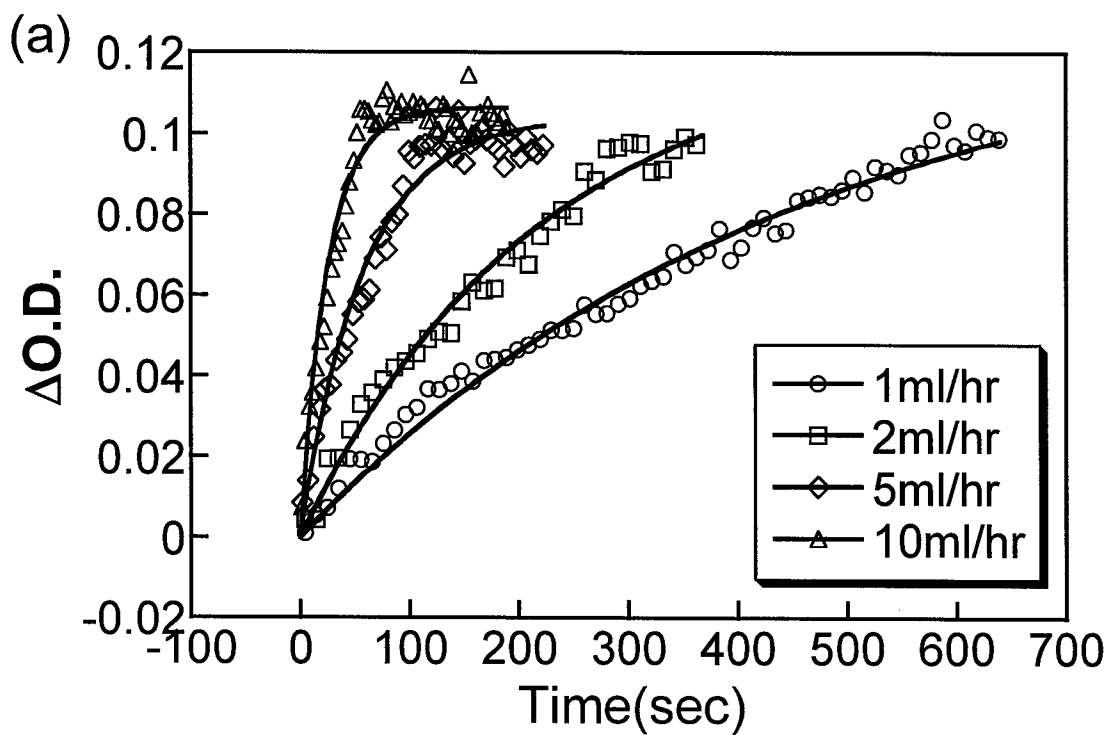


Figure 5

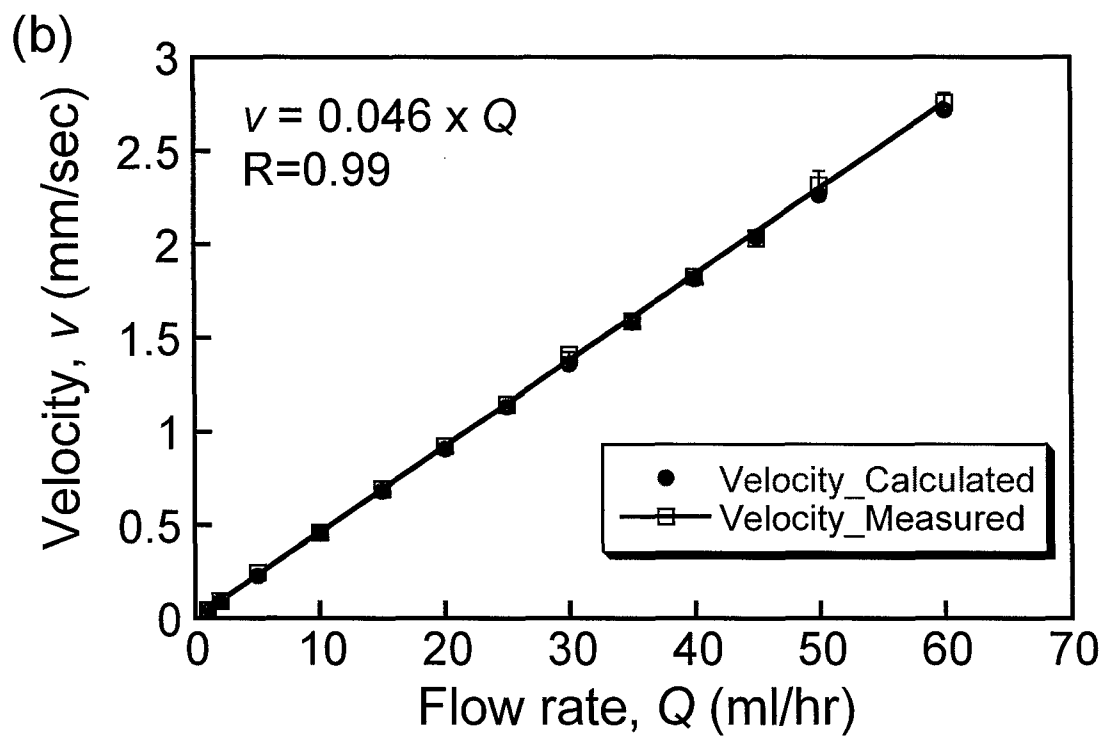
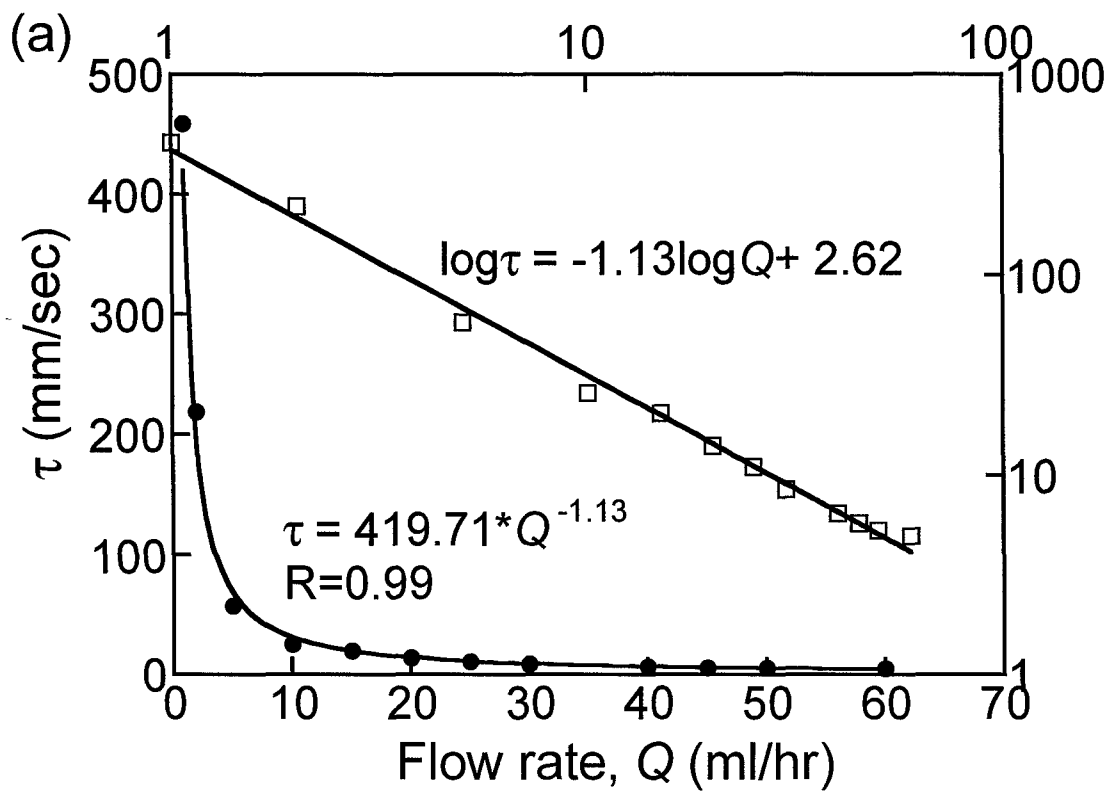


Figure 6

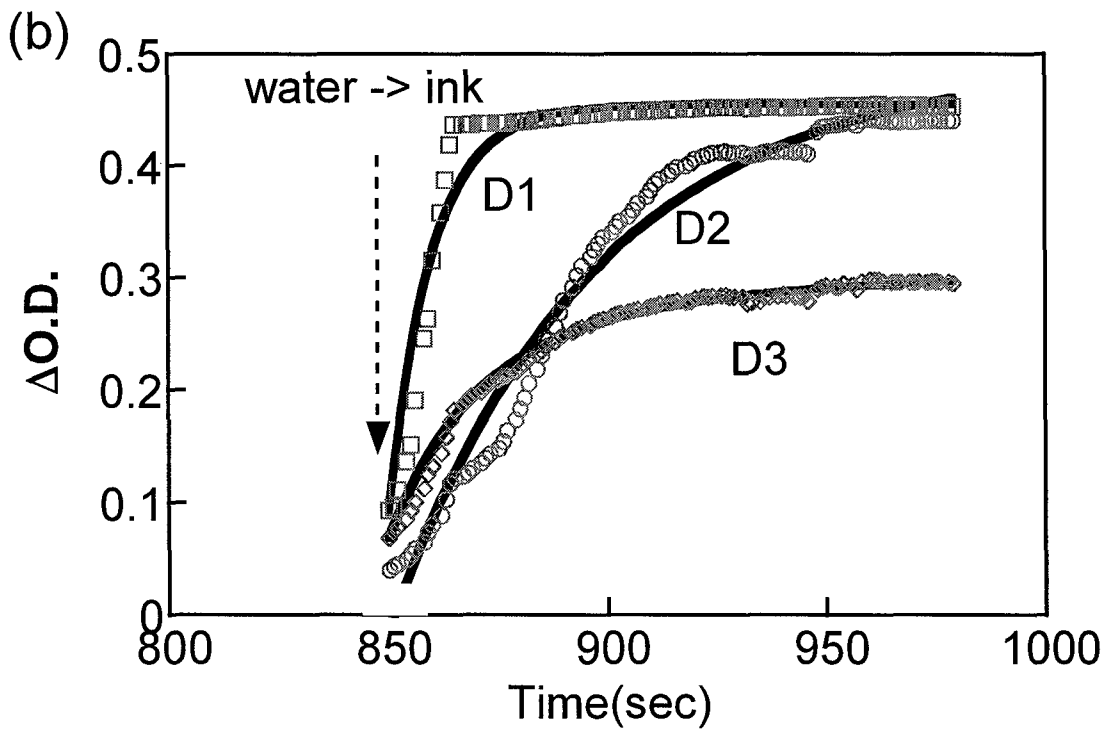
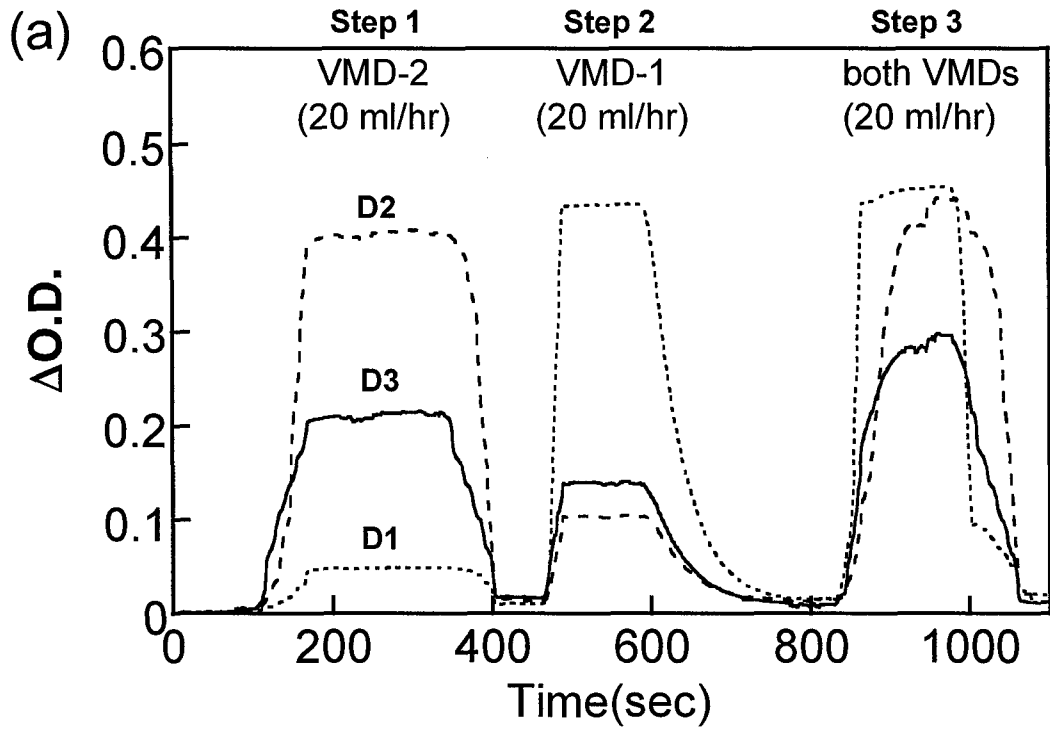


Figure 7

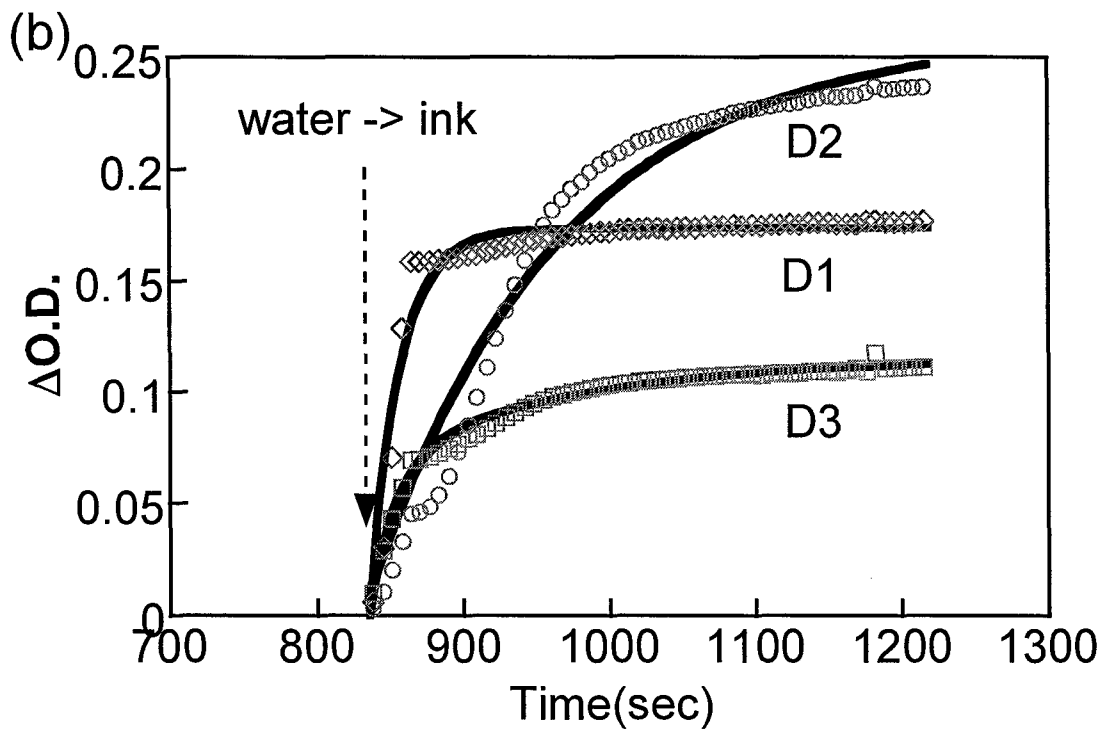
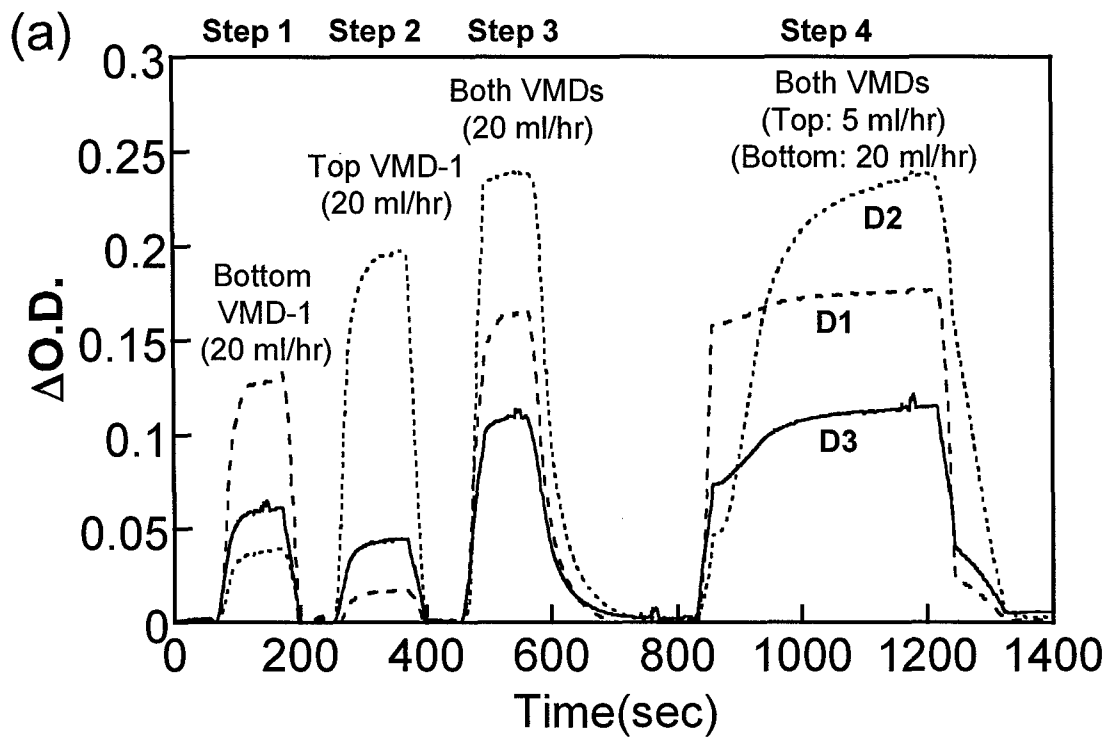


Figure 8

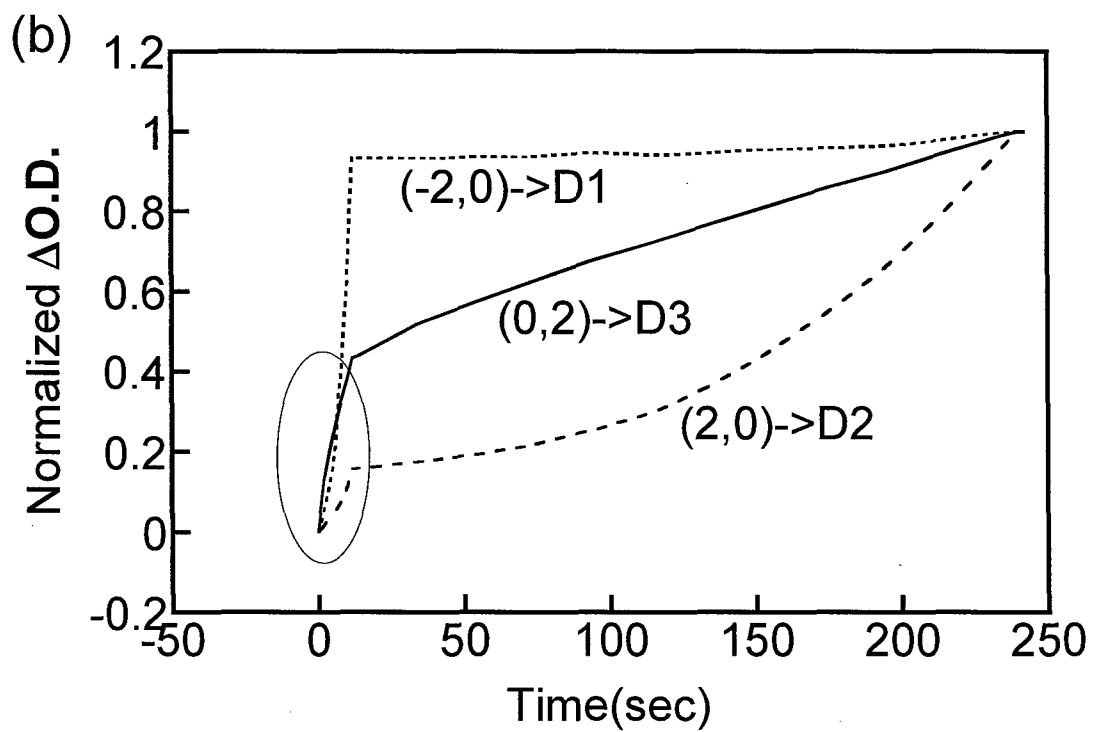
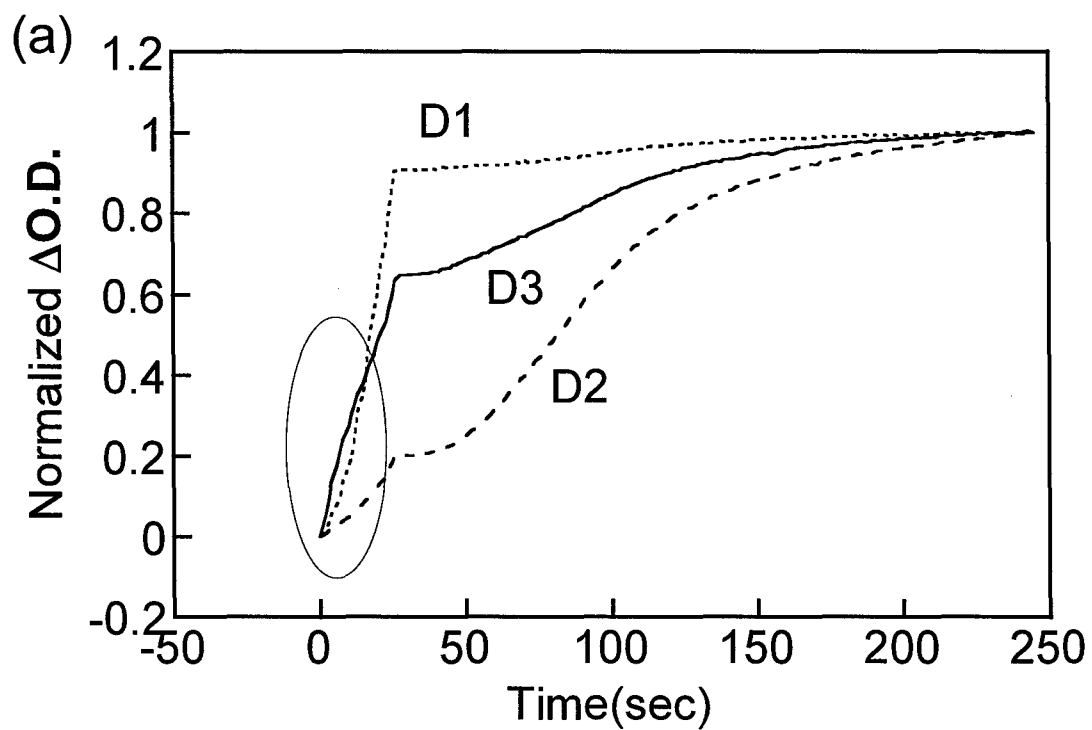


Figure 9

## REFERENCES

1. R. J. Gillies, P. A. Schornack, T. W. Secomb, and N. Raghunand, "Causes and effects of heterogeneous perfusion in tumors," *Neoplasia*, **1** (3), 197-207 (1999).
2. D. R. Tailor, H. Poptani, J. D. Glickson, J. S. Leigh, and R. Reddy, "High-Resolution Assessment of Blood Flow in Murine RIF-1 Tumors by Monitoring Uptake of H<sub>2</sub> <sup>17</sup>O With Proton T<sub>1</sub>ρ-Weighted Imaging," *Magn. Reson. Med.*, **49**, 1-6 (2003).
3. J. C. Acker, M. W. Dewhirst, G. M. Honore, T. V. Samulski, J. A. Tucker, and J. R. Oleson, "Blood perfusion measurements in human tumors, evaluation of laser Doppler methods," *Int. J. Hypertherm.*, **6**, 287-304 (1990).
4. J. Griebel, N. A. Mayr, A. de Vries, M. V. Knopp, T. Gneiting, C. Kremser, M. Essig, H. Hawighorst, P. H. Lukas, and W. T. Yuh, "Assessment of tumor microcirculation: a new role of dynamic contrast MR imaging," *J. Magn. Reson. Imaging*, **7**, 111-119 (1997).
5. T. Durduran, "Non-invasive measurements of tissue hemodynamics with hybrid diffuse optical methods," PhD dissertation, University of Pennsylvania (2004)
6. M. W. Dewhirst, C. Gustafson, J. F. Gross, and C. Y. Tso, "Temporal effects of 5.0 Gy radiation in healing subcutaneous microvasculature of a dorsal flap window chamber", *Radiat. Res.*, **112**, 581-591 (1987).
7. R. P. Mason, A. Constantinescu, S. Hunjan, D. Le, E. W. Hahn, P. P. Antich, C. Blum, and P. Peschke, "Regional tumor oxygenation and measurement of dynamic changes." *Radiat. Res.*, **152**, 239-249 (1999).

- 
8. 8. D. Zhao, A. Constantinescu, E. W. Hahn and R. P. Mason. "Tumor oxygenation dynamics with respect to growth and respiratory challenge: Investigation of the Dunning prostate R3327-HI tumor," *Radiat. Res.*, **156**(5), 510-520 (2001).
  9. 9. S. Hunjan, D. Zhao, A. Constantinescu, E. W. Hahn, P. Antich, and R. P. Mason, "Tumor oximetry: demonstration of an enhanced dynamic mapping procedure using fluorine-19 echo planar magnetic resonance imaging in the dunning prostate R3327-AT1 rat tumor," *Int. J. Radiat. Oncol. Biol. Phys.*, **49**, 1097-1108 (2001).
  10. 10. M. Höckel, P. Vaupel, "Tumor hypoxia: definitions and current clinical, biologic, and molecular aspects", *J Natl Cancer Inst.*, **93**, 266-76 (2001).
  11. 11. B. Chance, S. Nioka, J. Kent, K. McCully, M. Fountain, R. Greenfield, and G. Holtom, "Time resolved spectroscopy of hemoglobin and myoglobin in resting and ischemic muscle", *Anal. Biochem.*, **174**,698-707 (1988).
  12. 12. S. Homma, T. Fukunaga,, and A. Kagaya, "Influence of adipose tissue thickness on near infrared spectroscopic signals in the measurement of human muscle", *J. Biomed. Opt.*, **1**(4), 418-424 (1996).
  13. 13. M. Ferrari, Q. Wei, L. Carraresi, R. A. De Blasi, and G. Zaccanti, "Time-resolved spectroscopy of the human forearm", *J. Photochem. Photobiol. B: Biol.*, **16**,141-153 (1992).
  14. 14. B. Chance, E. Anday, S. Nioka, S. Zhou, L. Hong, K. Worden, C. Li, T. Murray, Y. Ovetsky, D. Pidikiti, and R. Thomas, "A novel method for fast imaging of brain function non-invasively with light", *Optics Express*, **2**(10), 411-423 (1998).
  15. 15. R. Wenzel, H. Obrig, J. Ruben, K. Villringer, A. Thiel, J. Bernarding, U. Dirnagl, and A. Villringer, "Cerebral blood oxygenation changes induced by visual stimulation in humans", *J. Biomed. Opt.*, **1**(4),399-404 (1996).

- 
16. 16. M. Cope, and D. T. Delpy, "A system for long term measurement of cerebral blood and tissue oxygenation in newborn infants by near infrared transillumination", *Med. Biol. Eng. Comp.*, **26**, 289-294 (1988).
  17. 17. R. G. Steen, K. Kitagishi, and K. Morgan, "In vivo measurement of tumor blood oxygenation by near-infrared spectroscopy: immediate effects of pentobarbital overdose or carmustine treatment", *J. Neuro-Oncol.*, **22**, 209-220 (1994).
  18. 18. H. D. Sostman, S. Rockwell, A. L. Sylvia, D. Madwed, G. Cofer, H. C. Charles, R. Negro-Vilar, and D. Moore, "Evaluation of BA1112 rhabdomyosarcoma oxygenation with microelectrodes, optical spectrophotometry, radiosensitivity, and magnetic resonance spectroscopy", *Magn. Reson. Med.*, **20**, 253-267 (1991).
  19. 19. H. Liu, Y. Song, K. L. Worden, X. Jiang, A. Constantinescu, and R. P. Mason, "Noninvasive Investigation of Blood Oxygenation Dynamics of Tumors by Near-Infrared Spectroscopy", *Applied Optics*, **39**(28), 5231-5243 (2000).
  20. 20. R. H. Thomlinson, and L. H. Gray, "The histological structure of some human lung cancers and the possible implications for radiotherapy", *Br. J. Cancer*, **9**, 539-549 (1955).
  21. 21. E. E. Schwartz, *The biological basis of radiation therapy* (Lippincott, Philadelphia, 1966).
  22. 22. B. Teicher, J. Lazo, and A. Sartorelli, "Classification of antineoplastic agents by their selective toxicities toward oxygenated and hypoxic tumor cells", *Cancer Res.*, **41**, 73-81 (1981).
  23. 23. J. D. Chapman, C. C. Stobbe, M. R. Arnfield, R. Santus, J. Lee, and M. S. McPhee, "Oxygen dependency of tumor cell killing *in vitro* by light activated photofrin II", *Radiat. Res.*, **126**, 73-79 (1991).

- 
24. 24. A. W. Fyles, M. Milosevic, R. Wng, M. C. Kavanagh, M. Pintile, A. Sun, W. Chapman, W. Levin, L. Manchul, T. J. Keane, and R. P. Hill, "Oxygenation predicts radiation response and survival in patients with cervix cancer", *Radiother. Oncol.*, **48**, 149-156 (1998).
25. 25. P. Bergsjö, P. Kolstad, "Clinical trial with atmospheric oxygen breathing during radiotherapy of cancer of the cervix," *Scand. J. Clin. Lab. Invest. Suppl.*, **106**, 167-171 (1968).
26. 26. H. D. Suit, N. Marshall, D. Woerner, "Oxygen, oxygen plus carbon dioxide, and radiation therapy of a mouse mammary carcinoma. Cancer," *Cancer*, **30**(5), 1154-1158 (1972).
27. <sup>27</sup> J. G. Kim, D. Zhao, Y. Song, A. Constantinescu, R. P. Mason, and H. Liu, "Interplay of Tumor Vascular Oxygenation and Tumor pO<sub>2</sub> Observed Using NIRS, pO<sub>2</sub> Needle Electrode and <sup>19</sup>F MR pO<sub>2</sub> Mapping", *J. of Biomed. Opt.*, **8**(1), 53-62 (2003)
28. <sup>28</sup> Y. Gu, V. A. Bourke, J. G. Kim, A. Constantinescu, R. P. Mason, and H. Liu, "Dynamic response of breast tumor oxygenation to hyperoxic respiratory challenge monitored with three oxygen-sensitive parameters", *Appl. Opt.*, **42**(16), 2960-2967 (2003)
29. 29. S. S. Kety, "The theory and applications of the exchange of inert gas at the lungs and tissue," *Pharmacol. Rev.*, **3**, 1-41 (1951)
30. 30. Jae G. Kim, Mengna Xia, Hanli Liu, "Extinction coefficients of hemoglobin for near-infrared spectroscopy of tissue", *IEEE Eng. in Med. & Biol. Magazine*, **24**(2), 118-121 (2005)
31. 31. D. T. Delpy, M. Cope, P. van der Zee, S. Arridge, S. Wray, and J. Wyatt, "Estimation of optical pathlength through tissue from direct time of flight measurement," *Phys. Med. Biol.* **33**(12), 1433-1442 (1988).

- 
32. 32. S. R. Arridge, M. Cope, and D. T. Delpy, "The theoretical basis for the determination of optical pathlengths in tissue: temporal and frequency analysis," *Phys. Med. Biol.*, **37**(7), 1531-1560 (1992).
33. 33. R. G. Steen, K. Kitagishi, and K. Morgan, "In vivo measurement of tumor blood oxygenation by near-infrared spectroscopy: Immediate effects of pentobarbital overdose or carmustine treatment," *J. Neuro-Oncol.* **22**, 209-220 (1994).
34. 34. Y. Gu, R. Mason, and H. Liu, "Estimated fraction of tumor vascular blood contents sampled by near infrared spectroscopy and <sup>19</sup>F magnetic resonance spectroscopy," *Opt. Express* **13**, 1724-1733 (2005),  
<http://www.opticsexpress.org/abstract.cfm?URI=OPEX-13-5-1724>
35. <sup>35</sup>. Y. Gu, W. R. Chen, M. Xia, S. W. Jeong, and H. Liu, "Effect of photothermal therapy on breast tumor vascular contents: Non-invasive monitoring by near infrared spectroscopy," *Photochem. Photobiol.* accepted (2005)
36. <sup>36</sup>. V. S. Kalambur, H. Mahaseth, J. C. Bischof, M. C. Kielbik, T. E. Welch, Å. Vilbäck, D. J. Swanlund, R. P. Hebbel, J. D. Belcher, G. M. Vercellotti, "Microvascular blood flow and stasis in transgenic sickle mice: Utility of a dorsal skin fold chamber for intravital microscopy," *Am. J. Hematol.*, **77**, 117-125 (2004).
37. <sup>37</sup>. J.G.Kim and H. Liu, "Investigation of bi-phasic tumor oxygen dynamics induced by hyperoxic gas intervention: *The numerical study*" accepted to *Opt. Express* (2005).

## Chemotherapeutic (Cyclophosphamide) Effects on Rat Breast Tumor Hemodynamics Monitored by Multi-Channel NIRS.

Jae G. Kim<sup>a</sup>, Dawen Zhao<sup>b</sup>, Ralph P. Mason<sup>b</sup>, Hanli Liu<sup>\*a</sup>

<sup>a</sup>Joint Graduate Program of Biomedical Engineering,  
University of Texas Southwestern Medical Center at Dallas/ University of Texas at Arlington  
Arlington, TX 76019

<sup>b</sup>Advanced Radiological Sciences, Department of Radiology  
University of Texas Southwestern Medical Center at Dallas  
Dallas, TX 75390

### ABSTRACT

We previously suggested that the two time constants quantified from the increase of tumor oxyhemoglobin concentration,  $\Delta[\text{HbO}_2]$ , during hyperoxic gas intervention are associated with two blood flow/perfusion rates in well perfused and poorly perfused regions of tumors. In this study, our hypothesis is that when cancer therapy is applied to a tumor, changes in blood perfusion will occur and be detected by the NIRS. For experiments, systemic chemotherapy, cyclophosphamide (CTX), was applied to two groups of rats bearing syngeneic 13762NF mammary adenocarcinomas: one group received a single high dose i. p. (200 mg/kg CTX) and the other group continuous low doses (20 mg/kg CTX i. p. for 10 days). Time courses of changes in tumor  $\Delta[\text{HbO}_2]$  were measured at four different locations on the breast tumors non-invasively with an inhaled gas sequence of air-oxygen-air before and after CTX administration. Both rat body weight and tumor volume decreased after administration of high dose CTX, but continuous low doses showed decrease of tumor volume only. Baselines (without any therapy) intra- and inter-tumor heterogeneity of vascular oxygenation during oxygen inhalation were similar to our previous observations. After CTX treatment, significant changes in vascular hemodynamic response to oxygen inhalation were observed from both groups. By fitting the increase of  $\Delta[\text{HbO}_2]$  during oxygen inhalation, we have obtained changes of vascular structure ratio and also of perfusion rate ratio before and after chemotherapy. The preliminary results suggest that cyclophosphamide has greatest effect on the well perfused tumor vasculature. Overall, our study supports our earlier hypothesis, proving that the effects of chemotherapy in tumor may be monitored non-invasively by using NIRS to detect changes of hemodynamics induced with respiratory challenges.

**Keywords:** Breast Cancer, Cyclophosphamide, Hemodynamics, NIR Spectroscopy, Tumor vascular oxygenation

### 1. INTRODUCTION

In addition to surgical resection, many other types of cancer therapy are available for patients including radiotherapy, photodynamic therapy and chemotherapy. Chemotherapy plays an important role to treat cancers even though it has some side effects. Currently, the effect of chemotherapy is monitored by MRI or CT that can measure the tumor volume changes during cancer treatment. However, it can take up to 3 weeks to detect such changes, and this is considerably late for clinicians to decide whether initial therapeutic strategy should be continued or modified. This delay in detection of chemotherapy effect can reduce the quality of a patient's life and ineffective therapy is costly. Therefore, many researchers are trying to develop tools that can detect the early response to cancer treatment. For example, Li *et al.* have used <sup>31</sup>P nuclear magnetic resonance spectroscopy (NMRS) to measure the effectiveness of cyclophosphamide (CTX) treatment in radiation-induced fibrosarcoma (RIF).<sup>1</sup> They found that the ratio of inorganic phosphate to other phosphate metabolites in CTX treated group was significantly decreased during the tumor growth delay period compared to age-matched controls. Poptani *et al.* studied the effects of CTX treatment in RIF-1 tumors in terms of tumor oxygenation

and glycolytic rate changes by utilizing  $^{13}\text{C}$  MRS, Eppendorf electrode, and Redox scanning.<sup>2</sup> They observed that CTX treatment caused reduction in glycolytic rate, a significant decrease in tumor tissue  $\text{pO}_2$ , and also an increase of NADH levels 24 hours after the treatment while tumor volume did not show any significant difference between the CTX-treated and control groups. Zhao *et al.* have reported significant changes in rat breast tumor perfusion following either single dose CTX or continuous low dose “metronomic” therapy.<sup>3</sup>

In the last decade, near infrared spectroscopy (NIRS) has been developed to examine tissue oxygenation and has been widely applied to investigate hemoglobin oxygenations of muscles,<sup>4,5,6</sup> the brain,<sup>7,8,9</sup> and animal tumors.<sup>10,11,12,13,20</sup> Since tumors have higher vascular density and also higher metabolism than normal tissues, total hemoglobin concentration ( $[\text{Hb}_{\text{total}}]$ ), oxyhemoglobin concentration ( $[\text{HbO}_2]$ ), and reduced scattering coefficient ( $\mu_s'$ ) were used as markers to identify tumors from the human breast by using NIRS.<sup>14,15,16</sup> In addition, an NIR spectrometer is a low-cost, portable, and real-time display instrument. Therefore, NIRS has a good potential to be used as a monitoring tool for tumor treatment planning and tumor prognosis.

We have previously studied breast tumor oxygenation under gas intervention using NIRS and found that oxyhemoglobin concentration changes ( $\Delta[\text{HbO}_2]$ ) during gas intervention can be fitted by a two-exponential equation containing two time constants.<sup>12</sup> Based on the model, we formed a hypothesis that changes in oxygenated hemoglobin concentration result from well perfused and poorly perfused regions of an animal tumor to explain why there are two different time constants in the  $\Delta[\text{HbO}_2]$  data. The model further allows us to associate the signal amplitudes and time constants to the ratio of vascular density and the ratio of the perfusion rates in the two different regions, respectively.

In this study, we applied the NIRS system to monitor the tumor oxygenation changes during oxygen intervention before and after CTX administration. The purpose for this study is to explore the NIRS as a possible tool for monitoring tumor responses to chemotherapy. This work is based on the following hypothesis: when tumor is treated with chemotherapy, changes in blood perfusion and vascular density in the tumor will occur and will be seen as changes of the two fitted parameters from the NIRS measurements. In addition, by developing a non-invasive tool for monitoring cancer therapy, we are not only monitoring the reduction of tumor size, but also detecting the changes of tumor physiological conditions, which are essential for tumor treatment planning and tumor prognosis.

## 2. MATERIALS AND METHODS

### 2.1 Tumor Model and Experimental Procedure

Rats were divided into three groups for this study. Two groups were treated with CTX at different doses, and the other group was administered saline instead of CTX as a control group. Cyclophosphamide was chosen as a chemotherapeutic agent for this study since our tumor line is highly responsive to alkylating agents and platinum chemotherapeutic agents.<sup>17</sup> CTX is an antineoplastic alkylating agent, and it has been used to treat lymphomas, cancers of the ovary, breast and bladder, and chronic lymphocytic leukaemia.<sup>18,19</sup> The tumor line was rat mammary adenocarcinomas 13762NF (cells originally provided by the Division of Cancer Therapeutics, NCI), and the tumors were implanted in the hind limb of adult female Fisher 344 rats (~200 g).

The rats were anesthetized with 0.2 ml ketamine HCl (100 mg/ml; Aveco, Fort Dodge, IA) when the tumors reached approximately 1 cm in diameter and maintained under general gaseous anesthesia using a small animal anesthesia unit with air ( $1 \text{ dm}^3/\text{min}$ ) and 1% isoflurane through a mask placed over the mouth and nose. During the experiments, the rat was placed on a warm blanket to maintain body temperature, which was monitored with a rectally inserted thermal probe connected to a digital thermometer (Digi-Sense, model 91100-50, Cole-Parmer Instrument Company, Vernon Hills, IL). Tumors were shaved before measurements to improve optical contact for transmitting light. A pulse oximeter (model: 8600V, Nonin, Inc.) was placed on the hind foot to monitor arterial oxygenation ( $\text{S}_a\text{O}_2$ ) and heart rate. For the single high dose group ( $n=5$ ), a light source and four detectors from a multi-channel, CW (continuous wave) NIRS (NIM, Inc, Philadelphia, PA) were attached to the tumor using posts and swivel post clamps (see Figure 1(a)). For the multi low dose ( $n=3$ ) and control ( $n=3$ ) groups, we have used four-channel, frequency domain (FD), NIRS (ISS, Champaign, IL). In the latter case, the four sets of light sources replaced four detectors shown in Figure 1(b), and one detector fiber was placed on the top center of the tumor to obtain signals from four different regions of tumor.

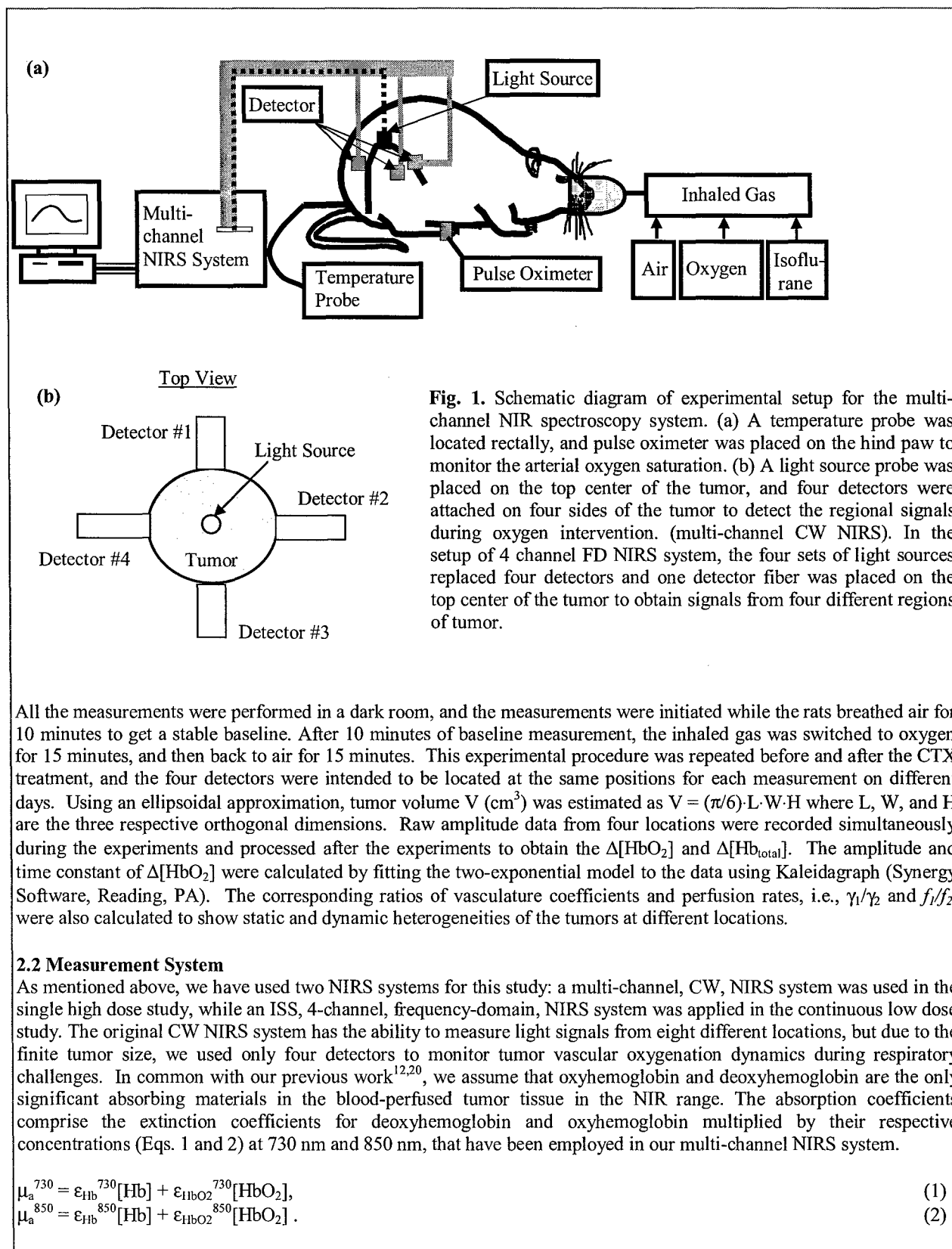


**Fig. 1.** Schematic diagram of experimental setup for the multi-channel NIR spectroscopy system. (a) A temperature probe was located rectally, and pulse oximeter was placed on the hind paw to monitor the arterial oxygen saturation. (b) A light source probe was placed on the top center of the tumor, and four detectors were attached on four sides of the tumor to detect the regional signals during oxygen intervention. (multi-channel CW NIRS). In the setup of 4 channel FD NIRS system, the four sets of light sources replaced four detectors and one detector fiber was placed on the top center of the tumor to obtain signals from four different regions of tumor.

All the measurements were performed in a dark room, and the measurements were initiated while the rats breathed air for 10 minutes to get a stable baseline. After 10 minutes of baseline measurement, the inhaled gas was switched to oxygen for 15 minutes, and then back to air for 15 minutes. This experimental procedure was repeated before and after the CTX treatment, and the four detectors were intended to be located at the same positions for each measurement on different days. Using an ellipsoidal approximation, tumor volume  $V$  ( $\text{cm}^3$ ) was estimated as  $V = (\pi/6) \cdot L \cdot W \cdot H$  where  $L$ ,  $W$ , and  $H$  are the three respective orthogonal dimensions. Raw amplitude data from four locations were recorded simultaneously during the experiments and processed after the experiments to obtain the  $\Delta[\text{HbO}_2]$  and  $\Delta[\text{Hb}_{\text{total}}]$ . The amplitude and time constant of  $\Delta[\text{HbO}_2]$  were calculated by fitting the two-exponential model to the data using Kaleidagraph (Synergy Software, Reading, PA). The corresponding ratios of vasculature coefficients and perfusion rates, i.e.,  $\gamma_1/\gamma_2$  and  $f_1/f_2$ , were also calculated to show static and dynamic heterogeneities of the tumors at different locations.

## 2.2 Measurement System

As mentioned above, we have used two NIRS systems for this study: a multi-channel, CW, NIRS system was used in the single high dose study, while an ISS, 4-channel, frequency-domain, NIRS system was applied in the continuous low dose study. The original CW NIRS system has the ability to measure light signals from eight different locations, but due to the finite tumor size, we used only four detectors to monitor tumor vascular oxygenation dynamics during respiratory challenges. In common with our previous work<sup>12,20</sup>, we assume that oxyhemoglobin and deoxyhemoglobin are the only significant absorbing materials in the blood-perfused tumor tissue in the NIR range. The absorption coefficients comprise the extinction coefficients for deoxyhemoglobin and oxyhemoglobin multiplied by their respective concentrations (Eqs. 1 and 2) at 730 nm and 850 nm, that have been employed in our multi-channel NIRS system.

$$\mu_a^{730} = \epsilon_{\text{Hb}}^{730}[\text{Hb}] + \epsilon_{\text{HbO}_2}^{730}[\text{HbO}_2], \quad (1)$$

$$\mu_a^{850} = \epsilon_{\text{Hb}}^{850}[\text{Hb}] + \epsilon_{\text{HbO}_2}^{850}[\text{HbO}_2]. \quad (2)$$

Based on modified Beer-Lambert's law, the data presented in this paper were analyzed using amplitude values to find the changes in absorption (Eq. 3). By manipulating Equations 1-3, changes in oxygenated hemoglobin, deoxygenated hemoglobin and total hemoglobin concentrations were calculated from the transmitted amplitude of the light through the tumor (Eqs. 4, 5 and 6).

$$\mu_{aB} - \mu_{aT} = \log (A_B/A_T) / L, \quad (3)$$

$$\Delta[\text{HbO}_2] = [-0.674 * \log (A_B/A_T)^{730} + 1.117 * \log (A_B/A_T)^{850}] / L, \quad (4)$$

$$\Delta[\text{Hb}] = [0.994 * \log (A_B/A_T)^{730} - 0.376 * \log (A_B/A_T)^{850}] / L, \quad (5)$$

$$\Delta[\text{Hb}_{\text{total}}] = \Delta[\text{Hb}] + \Delta[\text{HbO}_2] = [0.32 * \log (A_B/A_T)^{730} + 0.741 * \log (A_B/A_T)^{850}] / L, \quad (6)$$

where  $A_B$  = baseline amplitude;  $A_T$  = transition amplitude;  $L$  = optical pathlength between source/detector. The constants contained in these equations were computed with the extinction coefficients for oxy and deoxyhemoglobin at the two wavelengths used.<sup>21</sup> Notice that these coefficients have accounted for four hemes per hemoglobin molecule. In principle,  $L$  should be equal to the source-detector separation,  $d$ , multiplied by a differential pathlength factor (DPF), i.e.,  $L = d * \text{DPF}$ . Little is known about DPF for tumors, although a DPF value of 2.5 has been used by others.<sup>10</sup> Since our focus is on dynamic changes and relative values of tumor  $[\text{HbO}_2]$  in response to oxygen intervention, we have taken the approach of including the DPF in the unit, and eq. (4) becomes as follows:

$$\Delta[\text{HbO}_2] = [-0.674 * \log (A_B/A_T)^{730} + 1.117 * \log (A_B/A_T)^{850}] / d, \quad (7)$$

where  $d$  is the direct source-detector separation in cm, and the unit of  $\Delta[\text{HbO}_2]$  in Eq. (7) is mM/DPF.

Since the wavelengths of light sources from the ISS, frequency-domain system were 750 nm and 830 nm, the corresponding equations for  $\Delta[\text{HbO}_2]$ ,  $\Delta[\text{Hb}]$ , and  $\Delta[\text{Hb}_{\text{total}}]$  are modified as follows.

$$\Delta[\text{HbO}_2] = [-0.709 * \log (A_B/A_T)^{750} + 1.404 * \log (A_B/A_T)^{830}] / d, \quad (8)$$

$$\Delta[\text{Hb}] = [0.9546 * \log (A_B/A_T)^{750} - 0.4992 * \log (A_B/A_T)^{830}] / d, \quad (9)$$

$$\Delta[\text{Hb}_{\text{total}}] = \Delta[\text{Hb}] + \Delta[\text{HbO}_2] = [0.2456 * \log (A_B/A_T)^{750} + 0.9048 * \log (A_B/A_T)^{830}] / d. \quad (10)$$

### 2.3 Bi-exponential Model of Tumor Vascular Oxygenation

In our previous report,<sup>12</sup> we followed an approach used to measure regional cerebral blood flow (rCBF) with diffusible radiotracers, as originally developed by Kety<sup>22</sup> in the 1950's. By applying Fick's principle and defining  $\gamma$  as the ratio of  $\text{HbO}_2$  concentration changes in the vascular bed to that in veins, we arrived at Eq. (11):

$$\Delta\text{HbO}_2^{\text{vasculature}}(t) = \gamma H_o [1 - \exp(-ft/\gamma)] = A_1 [1 - \exp(-t/\tau)] \quad (11)$$

where  $\gamma$  is the vasculature coefficient of the tumor,  $H_o$  is the arterial oxygenation input and  $f$  is the blood perfusion rate.

If a tumor has two distinct perfusion regions, and the measured signal results from both of the regions (Figure 2), then it is reasonable to include two different blood perfusion rates,  $f_1$  and  $f_2$ , and two different vasculature coefficients,  $\gamma_1$  and  $\gamma_2$ , in the model. Therefore, Eq. (11) can be modified to count for the double exponential feature observed in the experiments:

$$\begin{aligned} \Delta\text{HbO}_2^{\text{vasculature}}(t) &= \gamma_1 H_o [1 - \exp(-f_1 t / \gamma_1)] + \gamma_2 H_o [1 - \exp(-f_2 t / \gamma_2)] \\ &= A_1 [1 - \exp(-t/\tau_1)] + A_2 [1 - \exp(-t/\tau_2)] \end{aligned} \quad (12)$$

where  $f_1$  and  $\gamma_1$  are the blood perfusion rate and vasculature coefficient in region 1 for the well perfused region, respectively;  $f_2$  and  $\gamma_2$  have the same respective meanings in region 2 for the poorly perfused region, and  $A_1 = \gamma_1 H_o$ ,  $A_2 =$

$\gamma_2 H_0$ ,  $\tau_1 = \gamma_1 / f_1$ ,  $\tau_2 = \gamma_2 / f_2$ . Then, if  $A_1$ ,  $A_2$ ,  $\tau_1$ , and  $\tau_2$  are determined by fitting the measurements with the model, we can obtain the ratios of two vasculature coefficients and the two blood perfusion rates:

$$\frac{\gamma_1}{\gamma_2} = \frac{A_1}{A_2}, \quad \frac{f_1}{f_2} = \frac{A_1/A_2}{\tau_1/\tau_2}. \quad (13)$$

With these two ratios, we are able to understand more about tumor physiology, such as tumor vasculature and blood perfusion.

### 3. RESULTS

#### 3.1 Body weight and tumor volume changes during chemotherapy

Body weight and tumor volume were monitored before and after the CTX treatments to see the tumor responses and side effects from chemotherapy. In the single high dose treatment group, body weight decreased until 6 days after the treatment, but later increased for the rest of days of observation. Two rats among five in this group failed to survive at day 6 due to the toxicity from the high dose CTX treatment. Therefore, the data shown at day 8 and 10 represent the smaller group of rats which survived during the high dose treatment. Tumor volume did not further decreased after day 4. (Fig. 2(b)) In comparison, rats in the continuous low dose group initially lost weight after a low dose of CTX administration, but gradually gained the weight during the treatment, presenting low toxicity from the treatment. This group also showed a significant reduction in tumor volume during the treatment. For a control group, saline was injected into the rats instead of CTX, and a gradual decrease of body weight was observed, while their tumor volumes increased exponentially. Changes in rat body weight and tumor volume were normalized to day 0 (before CTX or saline administration). (Figures 2(a) and (b)) Solid circles represent the data from a control group, and open squares and open diamonds represent the continuous low dose group and single high dose group, respectively.

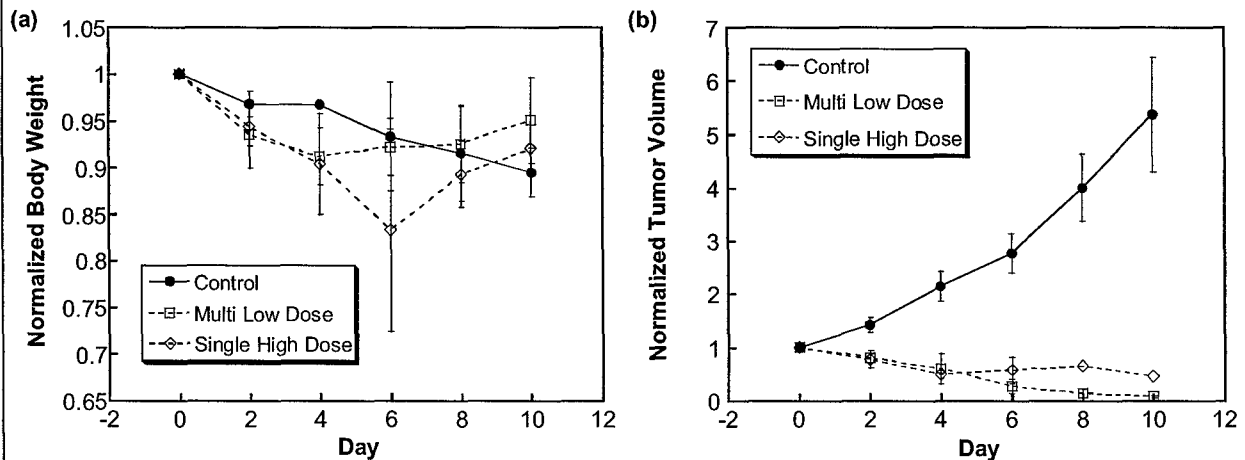
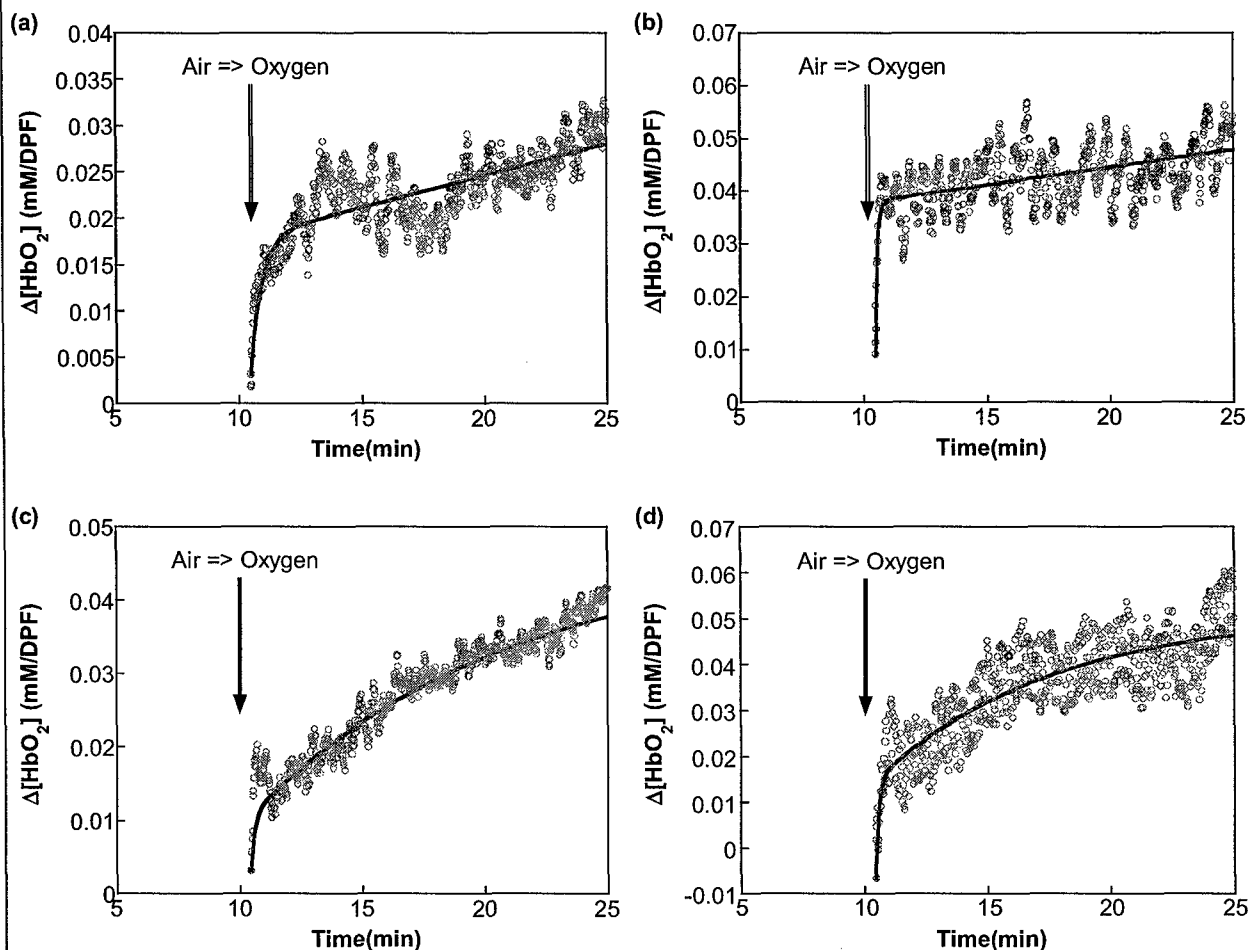


Fig. 2. Normalized changes in rat body weight (a) and tumor volume (b) during the saline and CTX treatments.

#### 3.2 Intratumoral heterogeneity of vascular oxygenation observed by the multi-channel NIRS

In our experiment, we have utilized either one light source and four detectors and from the CW system (NIM, Inc) or four light sources and one detector from the FD system (ISS, Inc.) for the rat breast tumor measurements, and the setups (Fig. 1). After 10 minutes of baseline measurement with air breathing, gas was switched to pure oxygen, causing a rapid increase in tumor  $[HbO_2]$ . These changes were measured simultaneously from four locations of the tumor. Figure 3 shows a representative set of data before the CTX treatment, with the DC NIRS system. Open circles show the raw data

measured by multi-channel NIRS, and the solid black lines represent the fitted curves using our bi-exponential model for hemodynamics during oxygen intervention.<sup>12</sup> It is apparent that the data from each location differs though there are similar trends of  $\Delta[\text{HbO}_2]$ .



**Fig. 3.** Dynamic changes of tumor  $[\text{HbO}_2]$  from four locations in a rat breast tumor. The rising parts of  $\Delta[\text{HbO}_2]$  from the four locations were fitted using a double-exponential expression. Figures 3(a)-3(d) were taken from locations #1-#4, respectively. In this case, the tumor was not treated yet.

**Table 1.** Summary of vascular oxygen dynamics determined at the four detectors from tumor shown in the Fig. 3.

Location	$A_1$	$A_2$	$\tau_1$	$\tau_2$	$A_1/A_2 (= \gamma_1/\gamma_2)$	$\tau_1/\tau_2$	$f_1/f_2$
1 (Fig. 3a)	0.013	0.027	0.48	24.3	0.48	0.02	24
2 (Fig. 3b)	0.029	0.026	0.09	29.8	1.12	0.003	373
3 (Fig. 3c)	0.008	0.036	0.15	10.6	0.22	0.014	16
4 (Fig. 3d)	0.021	0.037	0.12	7.25	0.57	0.017	34

To compare the data taken from four locations of the tumor more clearly, the time constants and amplitudes from the four fitted curves are summarized in Table 1. The ratios of  $\gamma_1/\gamma_2$  and  $f_1/f_2$  characterize tumor vascular structure and blood

perfusion within the volume of tumor interrogated by light.<sup>12</sup> In principle, when  $\gamma_1/\gamma_2$  is close to 1, it implies that the measured optical signal results equally from both regions 1 (*i.e.*, well perfused region) and 2 (*i.e.*, poorly perfused region); if  $\gamma_1/\gamma_2 < 1$ , the measured signal results more from region 2 than region 1 [Figures 3(a), 3(c) and 3(d)]. As Table 1 demonstrates, only location #2 has a ratio of  $\gamma_1/\gamma_2$  slightly higher than 1, and the readings from locations #1, #3 and #4 have the ratios of  $\gamma_1/\gamma_2$  less than 1. This may suggest that the tumor volume that was optically interrogated from location #2 was dominated by well perfused regions, while most of other tumor volumes detected from locations #1, #3 and #4 are composed of more poorly perfused regions. Furthermore, all the ratios of  $f_1/f_2$  from four locations of the tumor shown in Fig. 3 are much greater than 1, indicating that the blood perfusion rate in well perfused region is much greater than that in poorly perfused region. Especially,  $f_1/f_2$  from location #2 is 10 to 20 times higher than those from locations #1, #3, and #4, showing a high level of intratumoral heterogeneity in dynamic vascular structure.

### 3.3 Monitoring vascular hemodynamics of breast tumors before and after chemotherapy

The tumor hemodynamics during oxygen intervention were measured before and after administration of CTX and saline. The representative data from the control group and continuous low dose group are shown in Figs. 4(a) and 4(b), respectively. Similar to Figure 3, open symbols are the raw data from measurements, and solid lines are the fitted curves using our double exponential model. As mentioned before, there were 4 light sources placed on the surface of tumor. Figure 4 shows the acute and then gradual changes of  $[\text{HbO}_2]$  after switching the breathing gas from air to oxygen, and the data were observed at the same (or nearly the same) location of tumor from day 0 to day 6. From Figure 4(a), we can see different tumor hemodynamics at different days, but having similar trends and maximum  $\Delta[\text{HbO}_2]$  for the control group. However, the data taken from the continuous low dose group show quite different hemodynamics throughout the treatment days (Fig. 4(b)). Especially, we notice that the fast increase part became much smaller at Days 2 and 6 compared to Day 0, implying a significant decrease in signal from the well perfused region.

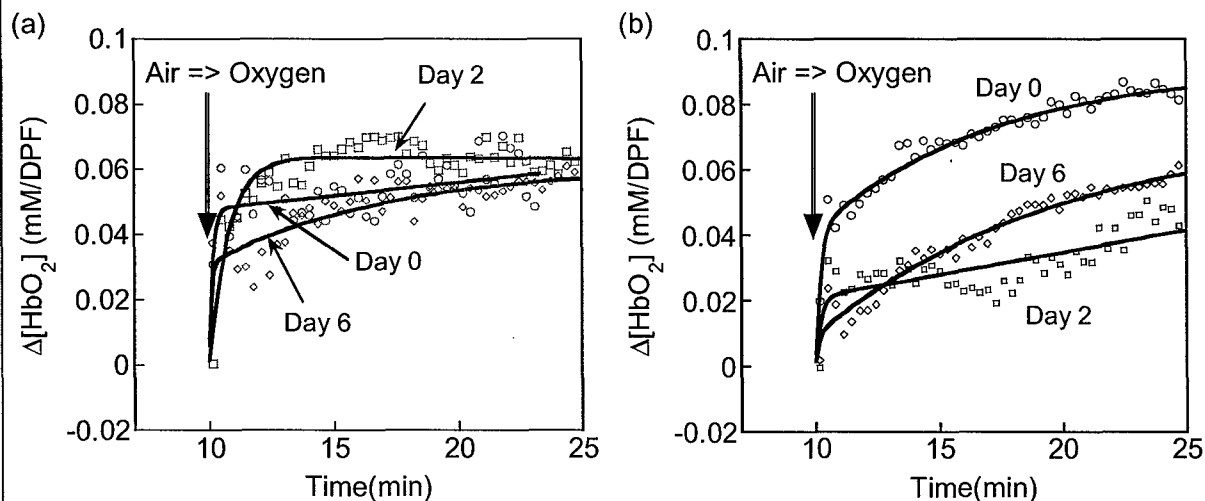


**Fig. 4.** Dynamic changes of  $\Delta[\text{HbO}_2]$  taken at location #1 from a rat breast tumor before and after administration of (a) saline and (b) continuous low dose of CTX (20 mg/kg for 10 days). The rising part of  $\Delta[\text{HbO}_2]$  from location #1 was fitted using the double-exponential expression.

Figure 5 also shows the changes of tumor hemodynamics during oxygen intervention, before and after a single high dose of CTX treatment, measured by the CW NIRS. This figure clearly demonstrates that we can observe significant changes in tumor hemodynamics after chemotherapy by using respiratory challenge as a mediator. The fitted parameters from our mathematical model are summarized in Table 2 to compare the changes in hemodynamic parameters before and after administration of CTX. The rising part of  $\Delta[\text{HbO}_2]$  from location #1 was fitted using either a single- or double-exponential expression.

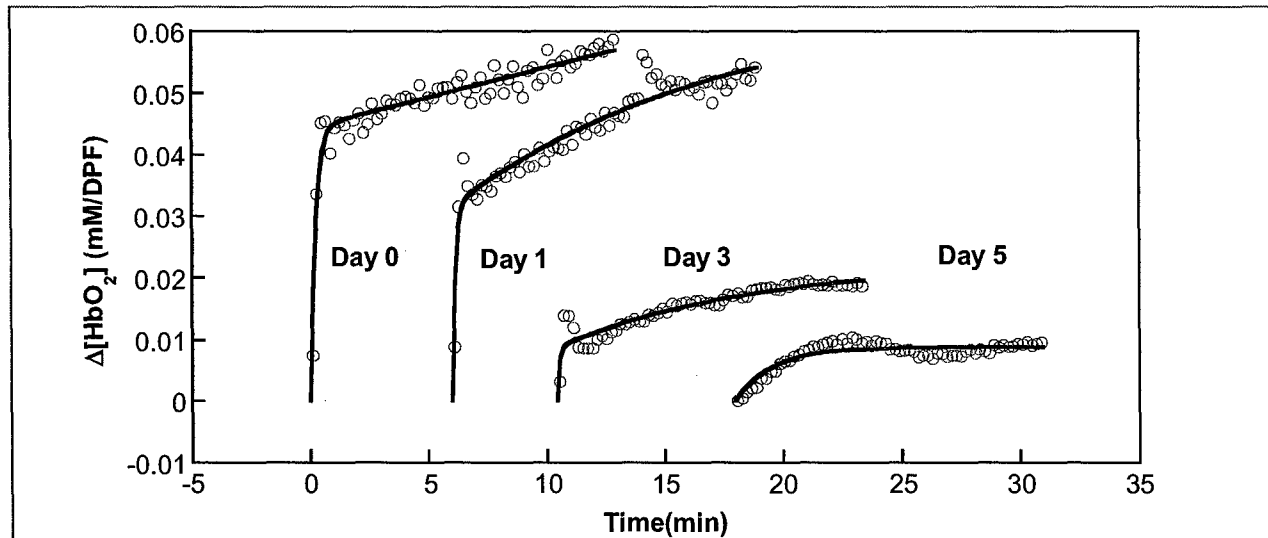


**Fig. 5.** Dynamic changes of  $[HbO_2]$  taken at location #1 from a rat breast tumor before and after a single high dose of CTX treatments (200mg/kg). The rising part of  $\Delta[HbO_2]$  from location #1 was fitted using either a single- or double-exponential expression.

**Table 2.** Summary of vascular oxygen dynamics determined at location #1 from the tumor shown in Fig. 5 before and after CTX treatment.

Day	$A_1$	$A_2$	$\tau_1$	$\tau_2$	$A_1/A_2 (= \gamma_1/\gamma_2)$	$\tau_1/\tau_2$	$f_1/f_2$
0	0.044	0.031	0.23	25.21	1.42	0.0091	156
1	0.032	0.033	0.13	11.36	0.97	0.0114	85
3	0.0087	0.014	0.089	8.36	0.62	0.0106	58
5	0.0087		1.27				

#### 4. DISCUSSION

Changes of rat body weight and tumor volume clearly show that CTX treatment is effective for the tumor type that we have used in this study. For the control group, the average rat body weight gradually decreased during the entire course of treatment, which implies the sickness of rats possibly due to the tumor growth (cachexia). (At Day 10, the tumor volume was ~5 times larger than that at Day 0.) It is clear that there is a different effectiveness of CTX treatment between the single high dose group (200mg/kg) and continuous low dose group (20mg/kg for 10 days). Both of the CTX treatments delayed the tumor growth and even further reduced the tumor volume. However, a single high dose of CTX treatment caused the death of two rats, and the tumor volume was not decreased further 4 days after the treatment, while the continuous low dose CTX treatment continued to provide tumor regression without causing severe sickness. From this observation, it is obvious that continuous low dose of CTX treatment is working much better than a single high dose of CTX treatment for a rat mammary adenocarcinomas 13762NF tumor.

NIRS is a portable, low cost, and real time measurement system that can monitor changes of vascular oxygen levels by using two wavelengths. We have previously used a single-channel NIRS system with one light source and one detector for global measurements of  $\Delta[HbO_2]$  and  $\Delta[Hb_{total}]$  in tumors during respiratory challenges.<sup>12,20</sup> Through those experiments, we have found that most tumors have a bi-phasic behavior in  $\Delta[HbO_2]$  increase (i.e., a rapid increase followed by a slow and gradual increase) after switching the gas from air to carbogen/oxygen. To explain this bi-phasic behavior, we developed a mathematical model and formed a hypothesis that the bi-phasic behavior of  $\Delta[HbO_2]$  during carbogen/oxygen inhalation results from two different vascular regions in tumor with two blood perfusion rates and vascular structures.<sup>12</sup>

By giving an oxygen intervention, tumor blood vessels are acutely subject to an increase of  $[\text{HbO}_2]$  due to higher supply of oxygenated blood from artery compared to that from air breathing. However, due to the irregular vascular structure in tumor, the well perfused regions in tumor may have an increase in  $[\text{HbO}_2]$  much faster than other parts of tumor that are poorly perfused. Therefore, two time constants obtained from tumor hemodynamic measurements during oxygen intervention are able to reveal two blood flow/perfusion rates in tumor, more precisely, two speeds of blood flow within the tumor blood vessels. More recently, we have shown that the bi-phasic increase in optical density changes occurs when there exist two different flow rates in tumor vascular phantom.<sup>23</sup> The bi-phasic model is a basis of our current study where we wish to detect any changes in vascular structures, hemodynamic features, or perfusion rate within a tumor after CTX treatment.

The amplitude and time constants obtained from  $\Delta[\text{HbO}_2]$  increase (Fig. 5) are summarized in Table 2. At day 0, we can see that  $\gamma_1/\gamma_2$  is higher than 1, indicating that the measured signal results more from the well perfused region than poorly perfused region. However, this ratio becomes less than 1 after injection of cyclophosphamide (Day 1 and 3). This may be explained by destruction of vascular structure in tumor after chemotherapy. We expect that after a single high dose administration of CTX, the drug circulates in the blood vessels and is delivered to the tumor cells more in the well perfused region than in the poorly perfused region. This will lead to death of tumor cells in the well perfused region more effectively than that in the poorly perfused region, eventually resulting in decreases in tumor volume in the well perfused region more than in the poorly perfused region. Then, the tumor volume containing the well perfused regions will consequently decrease, so will the contribution of detected NIR signals from the well perfused region. In other words, a decrease in  $\gamma_1/\gamma_2$  may indicate decreases in well perfused regions in tumor volume, after the administration of CTX.

As shown in Table 2, moreover, the perfusion rate ratio,  $f_1/f_2$ , was also decreased after a single high dose of CTX administration. At Day 0,  $f_1/f_2$  was very high, meaning that there was a big difference of perfusion rate between the well perfused and poorly perfused region in tumor. However, this ratio significantly decreased at Day 1 and 3 after CTX treatment, representing that the perfusion rate gap between the well perfused region and poorly perfused region became much smaller than that at day 0. At Day 5, changes in  $[\text{HbO}_2]$  during oxygen intervention do not show any bi-phasic behavior anymore, and it was fitted by a single-exponential model. This may indicate that most of tumor cells and/or tumor vasculature in the well perfused region are possibly destroyed by the effect of CTX, resulting in quite different hemodynamic behavior.

## 5. CONCLUSION

In conclusion, we have conducted this study to show the possibility of using NIRS to monitor tumor hemodynamics in response to chemotherapy by comparing the changes in tumor vascular oxygenation before and after CTX treatment. The heterogeneity of tumor vasculature was easily observed by quantifying the blood perfusion rate and vascular coefficients at four different locations of the tumor. Tumor hemodynamics has been significantly changed before and after CTX treatment compared to the saline-treated control group, showing high possibility of the NIRS system to be used as a monitoring tool for cancer treatments. Our future studies will include the development of NIR imaging systems to obtain a map of tumor hemodynamic changes from whole tumor, allowing us to predict the efficacy of tumor treatment.

## ACKNOWLEDGEMENTS

This work was supported in part by the Department of Defense Breast Cancer Research grants DAMD 170310353(JGK), DAMD 170310363 (DZ), and DAMD 170010459 (HL) and by NIH/NCI P20 CA086354 (RPM). We are grateful to Ammar Adam for technical assistance and to Dr. Britton Chance at the University of Pennsylvania, Philadelphia for the support of the multi-channel NIRS system.

## REFERENCES

1. S. Li, J. P. Wehrle, S. S. Rajan, R. G. Steen, J. D. Glickson, and J. Hilton, "Response of radiation-induced fibrosarcoma-1 in mice to cyclophosphamide monitored by in vivo  $^{31}\text{P}$  nuclear magnetic resonance spectroscopy," *Cancer Research*, **48**, 4736-4742, 1988.
2. H. Poptani, N. Bansal, W. T. Jenkins, D. Blessington, A. Mancuso, D. S. Nelson, M. Feldman, E. J. Delikatny, B. Chance, and J. D. Glickson, "Cyclophosphamide treatment modifies tumor oxygenation and glycolytic rates of RIF-1 tumors:  $^{13}\text{C}$  magnetic resonance spectroscopy, Eppendorf electrode, and Redox scanning," *Cancer Research*, **63**, 8813-8820, 2003.
3. D. Zhao, A. Constantinescu, E. W. Hahn, and R. P. Mason, "In vivo evaluation of metronomic chemotherapy on prostate tumors by MRI," CaPCure, New York, NY, November 2003.
4. B. Chance, S. Nioka, J. Kent, K. McCully, M. Fountain, R. Greenfield, and G. Holtom, "Time resolved spectroscopy of hemoglobin and myoglobin in resting and ischemic muscle", *Anal. Biochem.*, **174**,698-707, 1988.
5. S. Homma, T. Fukunaga, and A. Kagaya, "Influence of adipose tissue thickness on near infrared spectroscopic signals in the measurement of human muscle", *J. Biomed. Opt.*, **1**(4), 418-424, 1996.
6. M. Ferrari, Q. Wei, L. Carraresi, R. A. De Blasi, and G. Zaccanti, "Time-resolved spectroscopy of the human forearm", *J. Photochem. Photobiol. B: Biol.*, **16**,141-153, 1992.
7. B. Chance, E. Anday, S. Nioka, S. Zhou, L. Hong, K. Worden, C. Li, T. Murray, Y. Ovetsky, D. Pidikiti, and R. Thomas, "A novel method for fast imaging of brain function non-invasively with light", *Optics Express*, **2**(10), 411-423 1998.
8. R. Wenzel, H. Obrig, J. Ruben, K. Villringer, A. Thiel, J. Bernarding, U. Dirnagl, and A. Villringer, "Cerebral blood oxygenation changes induced by visual stimulation in humans", *J. Biomed. Opt.*, **1**(4),399-404, 1996.
9. M. Cope, and D. T. Delpy, "A system for long term measurement of cerebral blood and tissue oxygenation in newborn infants by near infrared transillumination", *Med. Biol. Eng. Comp.*, **26**, 289-294, 1988.
10. R. G. Steen, K. Kitagishi, and K. Morgan, "In vivo measurement of tumor blood oxygenation by near-infrared spectroscopy: immediate effects of pentobarbital overdose or carmustine treatment", *J. Neuro-Oncol.*, **22**, 209-220, 1994.
11. H. D. Sostman, S. Rockwell, A. L. Sylvia, D. Madwed, G. Cofer, H. C. Charles, R. Negro-Vilar, and D. Moore, "Evaluation of BA1112 rhabdomyosarcoma oxygenation with microelectrodes, optical spectrophotometry, radiosensitivity, and magnetic resonance spectroscopy", *Magn. Reson. Med.*, **20**, 253-267, 1991.
12. H. Liu, Y. Song, K. L. Worden, X. Jiang, A. Constantinescu, and R. P. Mason, "Noninvasive Investigation of Blood Oxygenation Dynamics of Tumors by Near-Infrared Spectroscopy", *Applied Optics*, **39**(28), 5231-5243, 2000.
13. H. Liu, Y. Gu, J.G. Kim, and R. P. Mason, "Near infrared spectroscopy and imaging of tumor vascular oxygenation", *Methods Enzymol.*, **386**, 349-378, 2004
14. S. Nioka, M. Miwa, S. Orel, M. Shnall, M. Haida, S. Zhao, B. Chance, "Optical imaging of human breast cancer," *Adv. Exp. Med. Biol.*, **361**, 171-179, 1994.
15. J. B. Fishkin, O. Coquoz, E. R. Anderson, M. Brenner, B. J. Tromberg, "Frequency-domain photon migration measurements of normal and malignant tissue optical properties in a human subject," *Applied Optics*, **36**(1), 10-20, 1997.
16. B. Pogue, S. Jiang, S. Srinivasan, X. Song, H. Dehghani, K. Paulsen, T. Tosteson, C. Kogel, S. Soho, S. P. Poplack, "Near-infrared scattering spectrum differences between benign and malignant breast tumors measured in vivo with diffuse tomography," in Biomedical Topical Meetings on CD-ROM (The Optical Society of America, Washington, DC) 2004. ThB1.
17. D. B. S., Hoon, "Circlulating immune complexes in rats bearing 6-thioguanine-resistant variants of the 13762 mammary adenocarcinoma," *Cancer Res.*, **44**, 2406-2409 (1984).
18. A.R. Ahmed, S.M. Hombal, "Cyclophosphamide (Cytoxan). A review on relevant pharmacology and clinical uses," *J. Am. Acad. Dermatol.*, **11**(6), 1115-1126, 1984.

19. P. Calabresi, B. A. Chabner, "Antineoplastic agents", In: A.F. Gilman, T. W. Rall, A.S. Niss, and P. Taylor (Editors), *The Pharmacological Basis of Therapeutics*, 8<sup>th</sup> ed. MacGraw-Hill, Singapore. 1992.
20. J. G. Kim, D. Zhao, Y. Song, A. Constantinescu, R. P. Mason, and H. Liu, "Interplay of tumor vascular oxygenation and tumor pO<sub>2</sub> observed using near-infrared spectroscopy, an oxygen needle electrode, and <sup>19</sup>F MR pO<sub>2</sub> mapping", *J. Biomed. Opt.*, **8**(1), 53-62, 2003.
21. M. Cope, "The application of near infrared spectroscopy to non invasive monitoring of cerebral oxygenation in the newborn infant", PhD dissertation, Appendix A, University College London, 1991.
22. S. S. Kety, "The theory and applications of the exchange of inert gas at the lungs and tissue," *Pharmacol. Rev.*, **3**, 1-41, 1951.
23. J. G. Kim, and H. Liu, "Investigation of breast tumor hemodynamics using tumor vascular phantoms and FEM simulations", in *Biomedical Topical Meetings on CD-ROM* (The Optical Society of America, Washington, DC, 2004), WF16.